A STUDY OF THE $f_1(1285)\pi^-$ SYSTEM PRODUCED IN THE REACTION $\pi^- p \to \eta\pi^+\pi^-\pi^- p$ AT 18 GeV/c

A Dissertation

Submitted to the Graduate School

of the University of Notre Dame

in Partial Fulfillment of the Requirements

for the Degree of

Doctor of Philosophy

by

Todd Adams, B.S., M.S.

William D. Shephard, Director

Department of Physics

Notre Dame, Indiana

April, 1997

A STUDY OF THE $f_1(1285)\pi^-$ SYSTEM PRODUCED IN THE REACTION $\pi^- p \to \eta\pi^+\pi^-\pi^- p$ AT 18 GeV/c

Abstract

by

Todd Adams

The $f_1(1285)\pi$ system has been proposed as a strong candidate for a hybrid meson search. The flux tube model predicts $f_1(1285)\pi$ as a preferential decay mode of hybrid mesons. Several previous experiments have reported evidence for exotic J^{PC}=1^{-+} $f_1(1285)\pi^-$ states, although none have been confirmed. Brookhaven Experiment 852 is a meson spectroscopy experiment designed to search for exotic mesons in the light meson sector (< 3.0 GeV/c^2). The $f_1(1285)\pi$ system is available to E852 in many different channels. A study of the $f_1(1285)\pi^-$ system decaying to $\eta\pi^+\pi^-\pi^-$ is presented.

E852 studied π^-p interactions at 18 GeV/c during the 1994 AGS run. Approximately 900,000 $\eta\pi^+\pi^-\pi^- p$ events were reconstructed. The final selection criteria found about 12,000 events for the $f_1(1285)\pi^-$ analysis. The $f_1(1285)$ was seen to decay predominately through $a_0(980)\pi$. Other states contributing to the data sample included $\rho^0(770)a_0^-(980)$, $a_2^-(1320)\eta$, and $a_1^-(1260)\eta$. These states are not studied here.

A complete partial-wave analysis was performed on the final 12,000 events. This analysis showed the $\eta\pi^+\pi^-\pi^- p$ events were produced predominately via natural par-

ity exchange. The results showed significant contributions from $1^{++}0^{+}P\ f_1(1285)\pi^-$, $1^{-+}1^{+}S\ f_1(1285)\pi^-$ and $2^{-+}0^{+}D\ f_1(1285)\pi^-$ waves. The $1^{-+}1^{+}S\ f_1(1285)\pi^-$ wave is needed at the 99.99% confidence level. These three states were studied with a mass dependent analysis. The final results are interpreted and compared with previous experiments and theoretical calculations.

To my parents,

Dianne M. Adams
and
the late Ron Adams

TABLE OF CONTENTS

LIST OF FIGURES

LIST OF TABLES

ACKNOWLEDGEMENTS

First, I would like to acknowledge the great assistance I have received from Dr. William Shephard. Without his meticulous reading and editing this work would not be anywhere near the quality it has become. I would also like to acknowledge the help of Dr. Shephard, Dr. Neal Cason and Dr. John LoSecco in carrying out this analysis. Their experience in the field of high energy physics made the problems and solutions of this work much clearer. They always seemed to know the right questions to ask and the right way to interpret the answers. I have learned a great deal from them and hope to be able to pass that knowledge on to others.

The senior members of the E852 collaboration have all assisted in producing this work. The construction, running and analysis of this experiment has required their wide range of talents and experience. The MPS crew was indispensable in the running of this experiment.

I would like to thank my fellow Notre Dame graduate students Sydney Taegar, Joe Manak, Doran Stienike and Dave Thompson. It has been an educational time, especially due to the many hours of discussion of physics and other topics we have shared. The work of the other graduate students on E852, especially Rob Lindenbush and Jeff Gunter, has been especially helpful.

I truly appreciate the support of my friends here at Notre Dame during my graduate career. I would especially like to thank Jeremy and Valerie Kropf for their friendship. Thanks to all my friends from Hope College who helped me make it to graduate school. Also, thanks to James Vosler and Amy Wallace, two of my oldest friends, for always being there.

There are a number of people who have taught me throughout my life. I would like to thank all those who helped inspire my scientific curiosity. I would also like to acknowledge Coach Ed Rarey for all the wonderful things he taught me and so many others.

My whole family has been so supportive throughout the years. I would especially like to thank everyone for all the cards and prayers while I was recovering. Thank you to my sister and brother-in-law, Tracy and Chad Herr, for everything.

I would like to thank my late father, Ron, for teaching me so much in so little time and helping to start my interest in science. Most importantly, I would like to thank Mom, your love and support has been crucial to everything I have done in life. The greatest gift you have ever given me was the freedom to choose what I wanted to do and pursue this dream. Mom and Dad, I hope I've made you proud.

CHAPTER 1

INTRODUCTION

Elementary particle physicists have been searching for decades for an understanding of the basic building blocks of the universe and their interactions. In the 1930's and 1940's the picture was simple with a few particles (protons, neutrons, electrons, pions, etc.) and a few forces (gravity, electromagnetism, the strong force and the weak force). Einstein felt a single theory explaining all particles and interactions was within his grasp [1]. Yet the next few decades saw an explosion of new particles. Development of the quark model by Gell-Mann and others [2] simplified and deepened our understanding. The last 20 years have seen many theories successfully developed and tested. These wide ranging theories have been combined into what is commonly referred to as the Standard Model. Much of the current work of high energy physics is based upon testing the Standard Model.

The Standard Model includes Quantum Chromodynamics (QCD), Quantum Electrodynamics (QED), relativity, the quark model and others. It is actually a collection of theories and models rather than a single comprehensive theory. For this reason checks of the Standard Model generally test the individual parts. These tests may involve new particle searches such as the top quark discovery or precision measurement of predictable quantities such as M_Z/M_W.

Quantum Chromodynamics (QCD) is a major component of the Standard Model.

QCD describes the interaction of particles and fields via the strong force. The strong force is mediated by gluon exchange. These gluons carry color charge which allows interactions between gluons. This is in contrast to Quantum Electrodynamics where the photon carries no electric charge.

The interactions between gluons create additional bound states beyond the traditional mesons ($q\bar{q}$ states) and baryons (qqq states) [3]. Two or three gluons (gg or ggg) can be bound by the exchange of virtual gluons. These states are called glueballs. Other bound states include a gluon, quark and anti-quark ($gq\bar{q}$). These are referred to as hybrid mesons or simply hybrids. A third type of state is composed of two quarks and two anti-quarks ($qq\bar{q}\bar{q}$). These are known as diquarkonium. All three types of states are collectively labeled exotic mesons.

The Standard Model requires the existence of these exotic mesons. However they may be difficult to identify experimentally [4, 5]. They are exotic *mesons* because they have a baryon number of zero. Their other quantum numbers may be exactly the same as the quantum numbers of a traditional meson. One experimental technique used to confirm the existence of exotic mesons is to fill the meson octets with all known meson states. Any octet with more than one particle filling a given position confirms the existence of exotics. It does not identify which of the particles is the traditional meson and which are exotic. Several states of interest (such as $a_0(980)$, $f_0(970)$, E/ι) have been identified this way as possible exotic mesons and are under further investigation.

The quantum numbers of exotic mesons are actually less restricted than those of traditional mesons. There are several J^{PC} combinations which cannot be created from a quark - anti-quark pair. These include 0^{--}, 0^{+-}, 1^{-+}, 2^{+-} and 3^{-+} [6]. Any hadron with baryon number zero and any of these J^{PC} values must be an exotic meson. Searches for such states have led to numerous candidates ($\hat{\rho}(1405), X(1910), etc.$), particularly with $J^{PC} = 1^{-+}$.

The third search technique is the study of the decay modes of states. A glueball should decay with no flavor preference while a $q\bar{q}$ state will have a bias. For example, the η' has a strange quark content. The branching ratios of a given state to $\pi\pi$, $\eta\pi$, $\eta'\pi$, $\eta\eta$, $\eta'\eta$, and $\eta'\eta'$ can be compared.

The experimental search for exotic mesons has been going on for decades. It is currently a major focus of meson spectroscopy. In 1988, an experiment was proposed as a further search for exotic mesons in the light meson sector [7]. The experiment was to run at Brookhaven National Lab (BNL). It involved upgrading the existing charged tracking facilities available at the Multi-Particle Spectrometer (MPS) with neutral particle measurement and kaon identification. The experiment was approved as BNL Experiment 852, A Search for Exotic Mesons.

As proposed E852 had the capability of exploring states which involved multiple charged pions, multiple charged kaons, multiple neutral particles and various combinations of these. It was also designed as a high statistics experiment. These abilities allow E852 to study many different states in the light meson spectrum. Exotic meson candidates are accessible in several decay channels (such as $\eta\pi^0$, $\eta\pi^-$, $\rho\pi$, and $f_1(1285)\pi^-$). It also allows studies of states which are not completely understood such as $f_0(970)$, $a_0(980)$, E/ι region and others. There are many additional decay channels available which have not been studied in detail including $b_1(1235)\pi$, and $\omega(782)\rho^0(770)$. Many of these states can be explored in different charge states (such as $f_1(1285)\pi^-$and $f_1(1285)\pi^0$).

1.1 Reaction

The focus of this work is the study of the $f_1(1285)\pi^-$ system in the E852 data. The theoretical and experimental justification for this topic will be discussed below. The E852 experiment has 18 GeV/c negatively charged pions incident upon a hydrogen target. The final state may be a combination of multiple charged and neutral particles. The following reaction was selected for this study:

$$
\begin{array}{l}
\pi^-\, p \longrightarrow X^-\, p \longrightarrow \underbrace{f_1(1285)/\eta(1295)}\ \pi^-\, p \\
\qquad\qquad\qquad\qquad\qquad \hookrightarrow \underbrace{a_0(980)}\ \pi \\
\qquad\qquad\qquad\qquad\qquad\qquad\quad \hookrightarrow \underbrace{\eta}\ \pi \\
\qquad\qquad\qquad\qquad\qquad\qquad\qquad\quad \hookrightarrow \gamma\,\gamma
\end{array}
\tag{1.1}
$$

The $\eta \rightarrow \gamma\gamma$ is reconstructed at the beginning of the analysis. Therefore, the final state of interest is $\eta\pi^+\pi^-\pi^- p$. This event sample is readily available in the E852 data.

There are many reasons for the choice of this reaction. The selection of events with only two photons eliminates the problems of photon combinatorics. The restriction to three charged pions greatly aids charged particle reconstruction and limits combinatorics. The experiment acceptance is adequate. Another consideration is the branching ratios for the decays. Each decay chosen is one of the dominant decay modes. This helps increase the number of events in the data sample. Despite these important points there remain difficulties with this data sample which will be discussed later. The E852 data contain other decay chains and final states which can be used to study the $f_1(1285)\pi^-$ system. The $f_1(1285)\pi^0$ system is also available for study. These are not considered here.

1.2 Theoretical Background

Quantum Chromodynamics is an incredibly complex and encompassing theory. This makes it a very powerful tool for describing the interactions of quarks and gluons. Yet its complexity also makes it difficult to calculate observable quantities directly with our current abilities and computer resources. Therefore, several models have been developed which attempt to simplify the calculations and accurately predict observables. One of these is the MIT bag model [8, 9, 10]. Another is the flux tube model [11, 12].

The flux tube model envisions a traditional meson as a quark and an anti-quark connected by a tube of virtual gluons. A hybrid meson has this tube vibrationally excited. This allows for calculations similar to harmonic oscillator calculations. The hybrid decay is accomplished by breaking of the flux tube. Because of the vibrational excitation a hybrid is predicted to prefer decays to one $L = 1$ and one $L = 0$ $q\bar{q}$ pair. Examples of such decay modes include $b_1(1235)\pi$ and $f_1(1285)\pi$. It is also predicted that the production mechanism in a πp reaction should be exchange of a vector meson with unnatural parity such as $b_1(1235)$ or $f_1(1285)$. This is also called unnatural parity exchange. Therefore, the flux tube model predicts hybrid mesons to couple strongly to $b_1(1235)\pi$ and $f_1(1285)\pi$ states.

Experimental results have led to an extension of the flux tube model by Close and Page [13]. This allows for coupling of hybrid mesons to two L=0 $q\bar{q}$ pairs. A hybrid can then decay through such channels as $\rho(770)\pi$, $\eta\pi$, $\eta'\pi$. It also means that natural parity exchange is allowed in a πp reaction. The coupling to two L=0 $q\bar{q}$ pairs is much smaller than to one L=1 and one L=0 $q\bar{q}$ pair. The extended flux tube model allows for production in a πp reaction via both natural and unnatural parity exchange. It also predicts that J^{PC}=1^{-+} hybrid mesons will decay with the following branching ratios:

$$\pi f_1(1285){:}\ \pi b_1(1235) : \pi\rho : \eta\pi : \eta'\pi = \ 60 : 170 : 5\text{-}20 : 0\text{-}10 : 0\text{-}10$$

The E852 experiment has the ability to investigate all of these channels. This provides for checking the flux tube model and verification of any hybrid candidates.

1.3 Experimental Background

The search for exotic mesons has been a priority of experimental meson spectroscopy for some time. Recently there have been several experiments involved directly in this search. The GAMS experiment [14] studied all-neutral final states. The VES experiment [15] studied mixed neutral and charged states created in $\pi^- N$ collisions. BNL E818 [16] studied the $f_1(1285)/\eta(1295)\pi^-$ state decaying to $K^+\bar{K}^0\pi^-\pi^-$. The KEK E179 experiment [17] studied the reaction $\pi^- p \rightarrow \eta\pi^- p$ at 6.3 GeV/c. There have been several other experiments which, while not primarily searching for exotic mesons, have investigated relevant channels.

There have been a number of exotic meson candidates which have been proposed. The $\hat{\rho}(1405)$ seen by GAMS [14] was quite promising. Several candidates have been proposed for a scalar glueball ($f_0(1500), f_0(1590), f_J(1700)$) [4, 18]. The $a_0(980)$ has been suggested as a $K\bar{K}$ molecule. However, no single candidate has been discovered which has been undeniably demonstrated to be an exotic meson.

The $f_1(1285)\pi$ system has been investigated in several experiments including Brookhaven E818, the VErtex Spectrometer (VES), and Fermilab E687. Each of these experiments sees evidence for an exotic J^{PC}=1^{-+} state which decays to $f_1(1285)\pi$. However, no single claim has been confirmed. The results of these experiments are presented below. Brookhaven Experiment 852 has the possibility of studying the state in several different decay channels.

1.3.1 BNL 818

Brookhaven Experiment 818 (BNL 818) has reported the strongest evidence for a 1^{-+} state in $f_1(1285)\pi$ [16, 19]. The experiment studied the reaction $\pi^- p \to K^+ \bar{K}^0 \pi^- \pi^- p$ at 18 GeV/c. The data were taken with the Multi-Particle Spectrometer (MPS) at the Alternating Gradient Synchrotron (AGS). A total of 747 $f_1(1285)\pi^-$ events were selected and analyzed with the BNL partial-wave analysis program. Several states were claimed. These include a 1^{++} state at 1.7 GeV/c^2 and a broad 1^{-+} state in the 1.6-2.2 GeV/c^2 region. The reaction was found to be almost entirely mediated by natural parity exchange, probably $f_2(1270)$ or $\rho^0(770)$ exchange. This is opposite from the original predictions of the flux tube model. However, the extension of the flux tube model by Close and Page [13] allows for the possibility of ρ exchange. The conclusions of BNL 818 were based on limited statistics.

1.3.2 VES

The VErtex Spectrometer (VES) experiment at Serpukhov has studied several reactions for hybrid states [15]. Of particular interest is the reaction $\pi^- N \to \eta\pi^+\pi^-\pi^- N$ (N = nucleus) at 37 GeV/c. There were 102,000 events of this type in the sample. A partial-wave analysis of the system showed a dominant $J^{PC}=1^{++}$ $f_1(1285)\pi^-$ wave and a small $J^{PC}=1^{-+}$ $f_1(1285)\pi^-$ wave in the region from 1.4-2.2 GeV/c^2. No claim about the properties of this $J^{PC}=1^{-+}$ wave is made except for its existence.

1.3.3 FNAL 687

Fermilab Experiment 687 was a high statistics charm photoproduction experiment. The $f_1(1285)\pi$ system was studied in the reactions $\gamma N \to K_S K^+ \pi^- \pi^\pm N'$ and $\gamma N \to$

$K_S K^- \pi^+ \pi^\pm N'$ [20]. A peak in the $f_1(1285)\pi$ mass distribution is seen at 1.750 GeV/c^2. An angular analysis of this peak indicates a J^{PC}=1^{-+}. This conclusion is also based on limited statistics.

1.4 Organization

This work has the following organization. Background material (theoretical and experimental) has been presented in this chapter (Chapter 1). Chapter 2 describes the setup of the E852 experiment. Chapter 3 details the data taking, data reconstruction, data characteristics and data selection criteria. Chapter 4 describes the partial-wave analysis of the data. Chapter 5 describes the final results and interpretation. Chapter 6 summarizes the conclusions of the analysis. Appendix A gives background information on the partial-wave analysis technique.

CHAPTER 2

EXPERIMENTAL SETUP

Brookhaven Experiment 852 was run at the Multi-Particle Spectrometer (MPS) facility at the AGS. The MPS facility has several major components, some of which were specifically added for E852. The incoming beam is the High Energy Unseparated Beamline (HEUB). The MPS magnet provides a 1 Tesla field for charged-particle momentum measurement. The target region was upgraded to include soft-photon vetoing and recoil-proton detection. Drift chambers and proportional wire counters were installed in the magnet. A large lead glass detector (LGD) was added downstream of the magnet for forward-photon measurement. This combination of detectors allows the study of a wide range of states and topologies which can include multiple charged pions and multiple neutral particles.

2.1 Beamline

The HEUB is located in the A beamline of the AGS. Protons from the main ring are incident upon the A target at 28 GeV/c. Collisions between these protons and the nucleons of the copper target produce a wide range of particle types and energies. The most forward of these particles are refocused into a new mixed beam and continue down the A beamline. These particles are focused and momentum selected by a series of dipole and quadrupole magnets. The resulting beam of 18.3 GeV/c negatively charged particles is delivered to the MPS. It is composed primarily of pions, but contains some other particles such as kaons and anti-protons.

The direction of the individual beam particles and their incident momentum is measured by a series of beam proportional wire chambers (PWCs) and beam scintillator hodoscopes [21]. There are 6 pairs of one PWC and one hodoscope. The first two pairs are located upstream of the momentum measuring dipoles (D3, D4) and two are located downstream of these dipoles. They determine the beam particle momentum [22]. The direction of the particle before entering the MPS is measured by two pairs located just in front of the magnet and the target support structure.

There are detectors placed along the beamline for particle identification and triggering. The three beam Čerenkov counters (C1, C2, C3) [23] were not used during the 1994 run. Scintillator counters were used for triggering. There were two primary sets of scintillators in the beamline. Each pair consisted of a paddle counter (S2 or S3) and a halo veto counter (S1 or S4). The first pair (S1 and S2) was located near the last set of quadrupole magnets. The second pair (S3 and S4) was located just before the beam enters the MPS. An additional beam definition counter (S0.5), placed further upstream, reduced the number of false accidental beam triggers. There were also various other scintillators (SA, SB) in the beamline used for beam focusing and special triggers.

2.2 The Spectrometer

The Multi-Particle Spectrometer facility has been active at BNL for several decades. The current magnet (MPS-II) provides a nearly uniform 1 Tesla field (full field) over a volume 450 cm long, 180 cm wide and 120 cm high [24]. Its coordinate system is defined with the vertex at the magnet pivot point ($x = 0$, $z = 0$) near the front of the magnet and y centered within the pole faces. The positive z direction points downstream along the magnet centerline. Positive y is up. This gives a right handed coordinate system with negatively charged particles bending in the negative x direction. A side view of the E852 experimental layout from the spectrometer to the lead glass detector is given in figure 2.1.

2.3 Target Region

The target used for E852 was a 30.48 cm (12 in) long, 6.35 cm (2.5 in) diameter aluminum and mylar tube filled with liquid hydrogen. The density of liquid hydrogen is .070 g/cm^3 which provides a 3% interaction rate. The target was centered 177.8 cm downstream of the magnet pivot point. This positioning (well within the MPS field) has the advantage of a larger opening angle for photons passing through the magnet aperture. The disadvantage of this placement is a shorter spread in drift chambers for charged particle momentum measurement and greater difficulty delivering the beam to the target center. The target was displaced 1.4 cm horizontally in the negative x direction to account for beam curvature within the MPS. The $\pi^- p$ center of mass axis does not generally lie along the z axis. An expanded drawing of the E852 target region is provided in figure 2.2.

A cylindrical drift chamber (TCYL) surrounds the target and its support structure [25]. It consists of 4 concentric cylinders. The innermost cylinder's radius is 6.8 cm, while the outermost radius is 9.5 cm. The purpose of TCYL is detection of recoil protons and wide-angle charged tracks. It is used both in the trigger and in event identification at the reconstruction level. The z position of a charged track is determined by the method of charge division while the azimuthal angle is given by the wire position. Momentum measurement is not available. TCYL is very similar to a cylindrical drift chamber used at the MPS in BNL Experiment 818 [26].

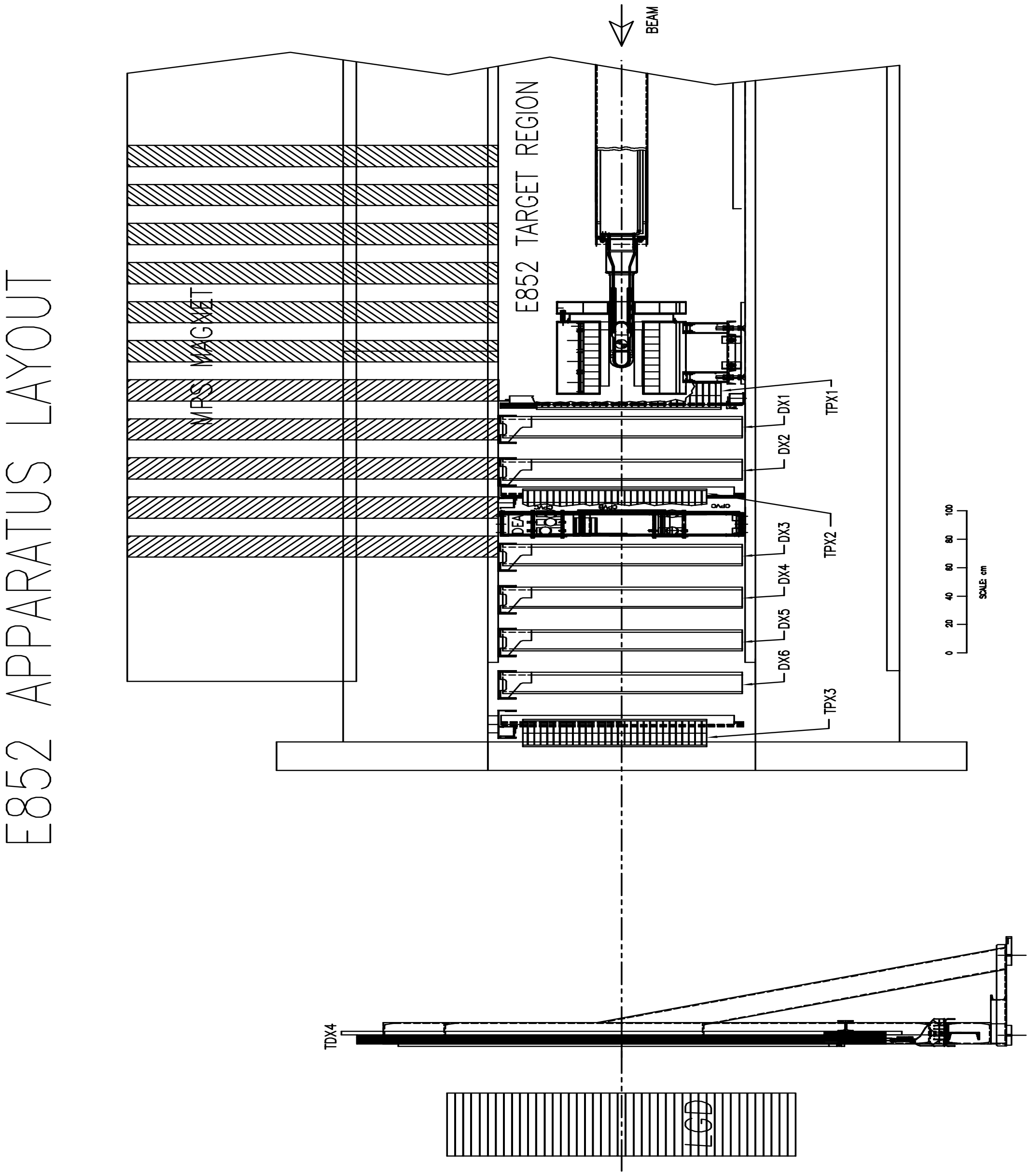

Figure 2.1: Experimental layout for E852.

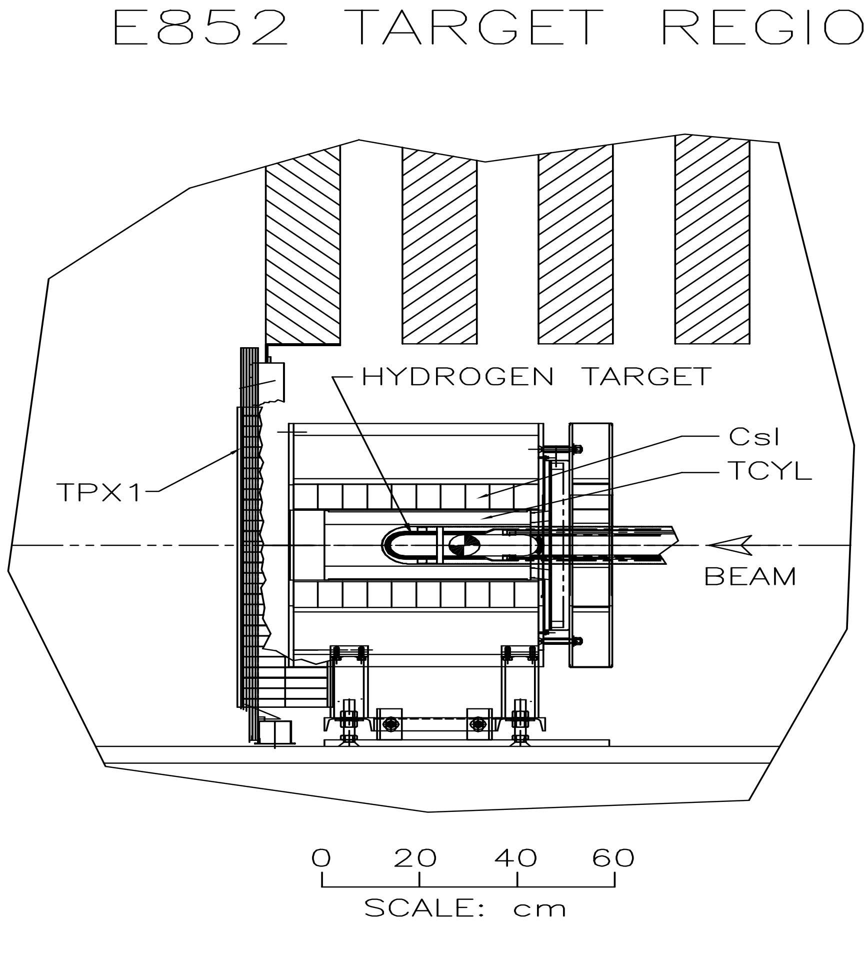

Figure 2.2: Target region for E852.

TCYL is surrounded by a CsI soft-photon detector. The CsI detector is a barrel of crystals which can detect photons coming from the reaction with a large angle to the beam [27]. Its primary purpose is to veto events with a recoil Δ particle which decays to a nucleon and a π^0. It also helps to give 4π steradian coverage for photon detection. It is 4 radiation lengths deep which does not fully contain many showers. It is used as a veto detector rather than as a calorimeter. The CsI detector is discussed in more detail later.

2.4 MPS Region

The main system of charged particle detection lies downstream of the target region. These detectors lie completely within the MPS magnet ensuring a uniform magnetic field and good momentum resolution. There are several parts to this system. It includes 3 proportional wire chambers (TPX1-3) and 6 drift chambers (DX1-6). The arrangement of chambers is given in figure 2.1.

The main purpose of the 3 downstream proportional wire chambers (PWC) is for the trigger, but they are also used in track reconstruction. The PWC wire planes measure only x position. The PWC planes contain 10 wires per inch. The first PWC (TPX1) is fully instrumented, but has a limited active region for triggering. This region consists of 238 wires covering the center area of the MPS region from $x = -26.7$ cm to $x = 34.0$ cm. The second PWC (TPX2) is fully used for readout and triggering. The final PWC (TPX3) is read out, but not used in the trigger.

The main detectors used for charged particle measurement are the 6 drift chambers (DC) [28, 29]. These are an integral part of the MPS facility and have been used in numerous experiments since their initial construction in 1982. Each chamber contains 7 planes. The three X planes measure the x position of the track while the two Y planes measure the y position. The U and V planes are oriented $\pm 30°$ from the Y plane. They are, in order from upstream to downstream, X′,X,X,Y,U,V,Y′. The X′ and Y′ planes are displaced .32 cm from the X and Y planes. The displaced planes (X′,Y′) help resolve left-right ambiguities while the tilted planes (U,V) help to match hits between the X and Y planes. The cell size for the drift chambers is .64 cm.

The final component of the MPS region is the DEA/CPV detectors. DEA stands for Downstream Endcap Array. It is a veto system for photons which miss both the lead glass and the CsI detectors. It consists of 4 sections of a layered lead/scintillator sandwich. The top and bottom pieces are fixed in position and each has two phototubes, one on each end. The side pieces can be moved horizontally and each has one phototube. The hole in the center is designed to shadow the lead glass detector. The DEA was uncalibrated and not used as a calorimeter. The front face of each section of the DEA is covered by a sheet of scintillator with its own phototube. These sections are called CPVC and identify charged particles which hit the DEA. The center hole of the DEA was filled with a single sheet of scintillator (CPVB) with two phototubes on it. The combination of CPVB and CPVC served as a portion of the neutral trigger.

2.5 LGD Region

The area downstream of the MPS contains several new detectors designed to measure photons. The main component is the lead glass detector. In front of it is located a large drift chamber. The original proposal for E852 included a Čerenkov detector (C9) in this region. However, that detector was not constructed for the 1994 or 1995 runs. It should be in place for the 1997 run. The LGD region also contains two scintillation counters, EV/BV, which veto non-interacting beam particles and elastic scattering events.

The major upgrade of the MPS facility for E852 was the addition of a large 3045 element lead glass detector (LGD) [30, 31]. Each lead glass block was 4 cm by 4 cm by 45 cm. They were stacked in an array 71 blocks wide by 43 blocks high. The light from each block was read out by a phototube on the back. The entire array was mounted on a transport system which allowed it to be moved in or out of the experiment and to change positions for magnetic field on or off. Four blocks at the center of the array were replaced by blocks of low-Z material to avoid interactions of straight-through beam tracks with the lead glass.

A new large-volume drift chamber (TDX4) was built to sit in front of the LGD. This was to facilitate reconstruction of charged tracks just before they reach the LGD. The reconstructed tracks were then used to tag clusters in the lead glass as hadrons rather than photons. TDX4 contained two X planes which were displaced from each other by .8 cm. The cell size for TDX4 is 1.6 cm.

2.6 Trigger

The physics trigger for E852 was a very complex system designed to maximize the interesting physics recorded while limiting the bias it imposed. It consisted of several parts including the pre-trigger, the level 1 trigger and the level 2 trigger. There were additional trigger possibilities not described here which included such events as straight-through beam, interacting beam, monitoring triggers, and random triggering.

The pretrigger was composed of fast scintillators whose signals were brought to a central location on top of the magnet as directly as possible. The initial requirement was that the beam counters S0.5, S2, S3 fired while the beam halo counters S1,S4 did not. There was also the requirement that the beam veto and elastic veto counters, EV/BV, didn't fire. The logic is given by:

$$Pretrig = S0.5 \cdot \overline{S1} \cdot S2 \cdot S3 \cdot \overline{S4} \cdot \overline{BV} \cdot \overline{EV} \tag{2.1}$$

The capability of including the beam Čerenkov counters was available, but not used. The pretrigger started the higher level triggers in motion and began event readout.

The level 1 trigger primarily determined event multiplicity. There were several components to this. TCYL was checked for the possibility of either zero or one track in it. The main requirement was zero or one hits in the outer cylinder. The single track requirement also needed at least one hit in 3 or more cylinders. The single track was nominally a recoil proton while the zero track was a recoil neutron.

The downstream charged particle requirement was determined by the TPX multiplicity trigger. This required a certain number of hits in the central region of TPX1 and a certain number of hits in TPX2. For the 1994 run of E852 the number of hits in each chamber was required to be the same. For a single track in TCYL, the TPX multiplicity was allowed to be either 1 or 3. For no track in TCYL it was allowed to be 0, 2, or 4. The level 1 trigger had the additional requirement for all-neutral events that there be no hits in CPVB, CPVC, or DEA. Failure at the level 1 trigger created resets for the readout and enabled the pretrigger again.

The level 2 trigger was an LGD requirement. The LGD had a digital trigger which had multiple capabilities [31]. It was able to do a fast calculation of the energy deposited, the effective mass and the cluster multiplicity among other things. For all-neutral events it required that the energy deposited in the lead glass be above a minimum level. In other triggers, it usually required the effective mass in the lead glass be greater than that of the π^0. The suppression of single π^0's greatly enriched the sample of η, $\pi^0\pi^0$ and other high-gamma-multiplicity events. Because of hadronic clusters, single π^0's still passed the level 2 trigger some of the time.

TABLE 2.1
TRIGGER MULTIPLICITIES FOR 1994 RUN

0-0-0-E	$n(N\gamma)$	$(N > 0)$
1-1-1-η	$p\pi^-(N\gamma)$	$(N > 1)$
0-2-2-η	$n\pi^+\pi^-(N\gamma)$	$(N > 1)$
1-3-3	$p\pi^+\pi^-\pi^-(N\gamma)$	$(N \geq 0)$
1-3-3-η	$p\pi^+\pi^-\pi^-(N\gamma)$	$(N > 1)$
0-4-4	$n\pi^+\pi^+\pi^-\pi^-(N\gamma)$	$(N \geq 0)$

E852 uses a general format for labeling trigger types by their multiplicity. The format is A-B-C-D. Here A is the number of tracks in TCYL, which is zero or one. B is the number of hits in the central region of TPX1 (B=0-4). C is the number of hits in TPX2 (C=0-4). D is the 2nd level LGD requirement which was described previously. Table 2.1 shows the allowed trigger types for most of the 1994 run. This work will concentrate on the 1-3-3-η trigger type.

2.7 *CsI Detector*

The CsI detector was the responsibility of the Notre Dame Group. It is a soft-photon veto detector which surrounds the target region. The CsI(Tl) crystals are arranged in rings of 18. The upstream ring (CIA or CIR) is composed of larger crystals which give coverage for backward photons. The remaining crystals form a 10 ring barrel (CIB). The CsI detector serves two purposes. The first is to veto events with wide-angle photons which would miss both the LGD and the DEA. The second is to veto events in which the recoil particle is not a nucleon. An example is a recoil Δ^+ which decays to $p\pi^0$.

The partial-wave analysis assumes that the reaction includes only a recoil nucleon. The CsI detector had several features to help ensure this. The main feature was sensitivity to low-energy photons. The CsI crystals were thallium doped to increase the light output of deposited energy. The CsI light spectrum adequately matches the sensitivity of the photodiodes used in readout. Preamps were designed and mounted directly with the photodiodes to increase the signal. The gain and gate of the signal electronics were set to maximize the low-energy sensitivity while keeping noise to a minimum. The crystal size was chosen based on cost, size and space constraints. The detector is not a calorimeter so containment of high-energy particles was not necessary. Additional details of some steps taken to reach design goals are described below.

2.7.1 *Photodiodes*

Within the MPS magnetic field, the use of phototubes for light readout is difficult. For this reason, photodiodes were chosen for the CsI detector. These photodiodes were matched as well as possible to the light spectrum of the CsI(Tl) crystals. They were also specified to have low dark current. PIN-type Hamamatsu 3590-01 photodiodes were selected. These photodiodes were tested at Notre Dame to ensure quality and usability. A special test station was designed. Each photodiode was used to measure the spectrum of ^{241}Am directly. The ^{241}Am source emits several good low-energy photons as shown in figure 2.3. The position, width and strength of the 60 keV peak was checked. All but one photodiode gave essentially the same results. That one photodiode gave no recognizable signal and was not used. There were no photodiode failures during the 1993, 1994 or 1995 runs.

2.7.2 *Calibration*

A small fraction of the beam pions decay during their trip down the HEUB by the process $\pi^- \to \mu^- \nu_\mu$. This creates a number of highly energetic μ^- particles

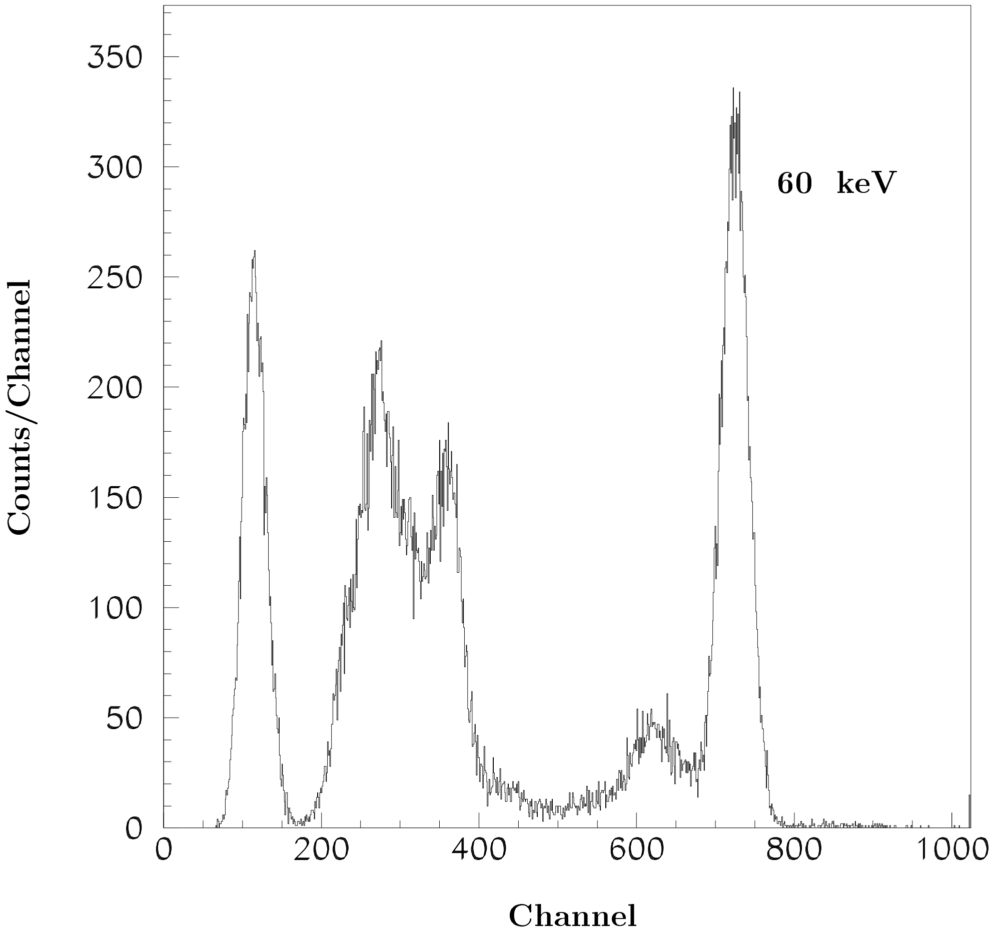

Figure 2.3: ^{241}Am photon spectrum observed in a typical photodiode test.

travelling nearly parallel to the beam. These muons are commonly known as the halo around long pion beamlines. Some muons are far enough away from the beam center to travel through the CsI barrel. Muons interact only electromagnetically and weakly. Therefore, they are most often simple minimum-ionizing particles [32, 33]. It was determined that these halo muons would be a good tool for calibrating the CsI detector.

The halo muons transverse the CsI detector generally parallel to its long axis. A straight-through muon should pass through all 11 crystals of a given row. The variation of pathlength through a crystal is small. This means the minimum-ionizing particle should deposit a fairly consistent amount of energy. Monte Carlo simulations of 18 GeV straight-through muons show an energy distribution with a well defined peak centered at 31 MeV for crystals in CIB (figure 2.4) and 43 MeV for crystals in CIA. This is a perfect calibration point for the low-energy sensitivity desired for the CsI.

A halo muon trigger was developed to collect events of the desired type. Scintillator paddles were built which covered the upstream and downstream faces of the CsI barrel. Each end was subdivided into three segments covering 120 degrees arc (6 crystal rows). The downstream end was rotated 60 degrees with respect to the upstream end. Any combination of one upstream and one downstream overlapping paddles covered 3 crystal rows. Each segment of scintillator was read out by one Hamamatsu type R2490-01 high-magnetic field phototube. The scintillator and phototube were connected by a series of specially built light guides. This allowed the phototubes to be oriented at 40 degrees from the magnetic field for best results. A 4508 Memory Lookup Unit (MLU) was programmed to trigger on two overlapping paddles firing and no signal in the remaining 4 paddles. A short running time (less than 2 hours) gave sufficient signal in all channels to calibrate.

Strict selection criteria were applied to the halo trigger data. The events were

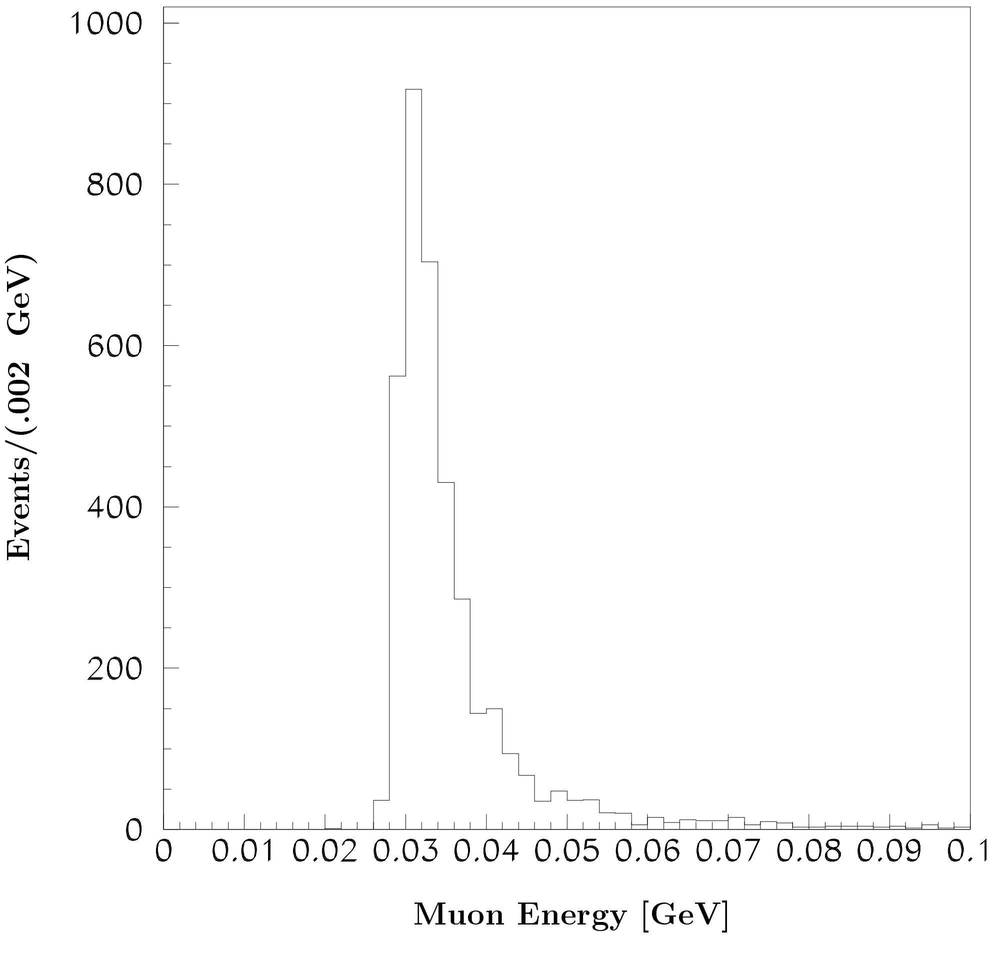

Figure 2.4: Distribution of energies deposited by Monte Carlo clean halo muons.

required to have 9-13 hits in the complete CsI barrel with at least 9 crystals in a row hit. Figure 2.5 shows a typical clean spectrum. The peak position was fit with a Gaussian-resolution smeared Landau distribution [34] and set to the appropriate energy for a minimum-ionizing particle. The pedestal was taken as zero energy deposited. A straight linear calibration was done. The calibration procedure was done at the beginning and end of each run (1993, 1994, 1995). Variations of a few percent were seen over several months time (figure 2.6).

2.7.3 Monitoring

During data taking, the CsI detector was monitored to ensure the quality of the recorded CsI data. This was done with several different systems, one of which is described here. The online data acquisition system was set up such that programs could connect to it and receive a small subset of the current data. One such program was designed to monitor the CsI detector. It histogrammed the CsI hits for each crystal. These histograms were available in real time through a shared memory segment. Other programs connected to this shared memory which allowed the user to view the histograms. Careful checking of each of the 198 crystals easily identified failed channels. The most common cause for failures was loose cables. There were no catastrophic failures of CsI crystals, photodiodes or associated electronics during the 1993, 1994 or 1995 runs.

These measures, combined with other work, produced a detector which met and surpassed its design specifications. Many studies of the effectiveness of the CsI detector have been carried out. Off-line use of the CsI detector as a soft-photon veto is effective in eliminating Δ's as seen by the missing-mass-squared distribution before and after cuts. Details of one such study are provided in Section 3.4.3.

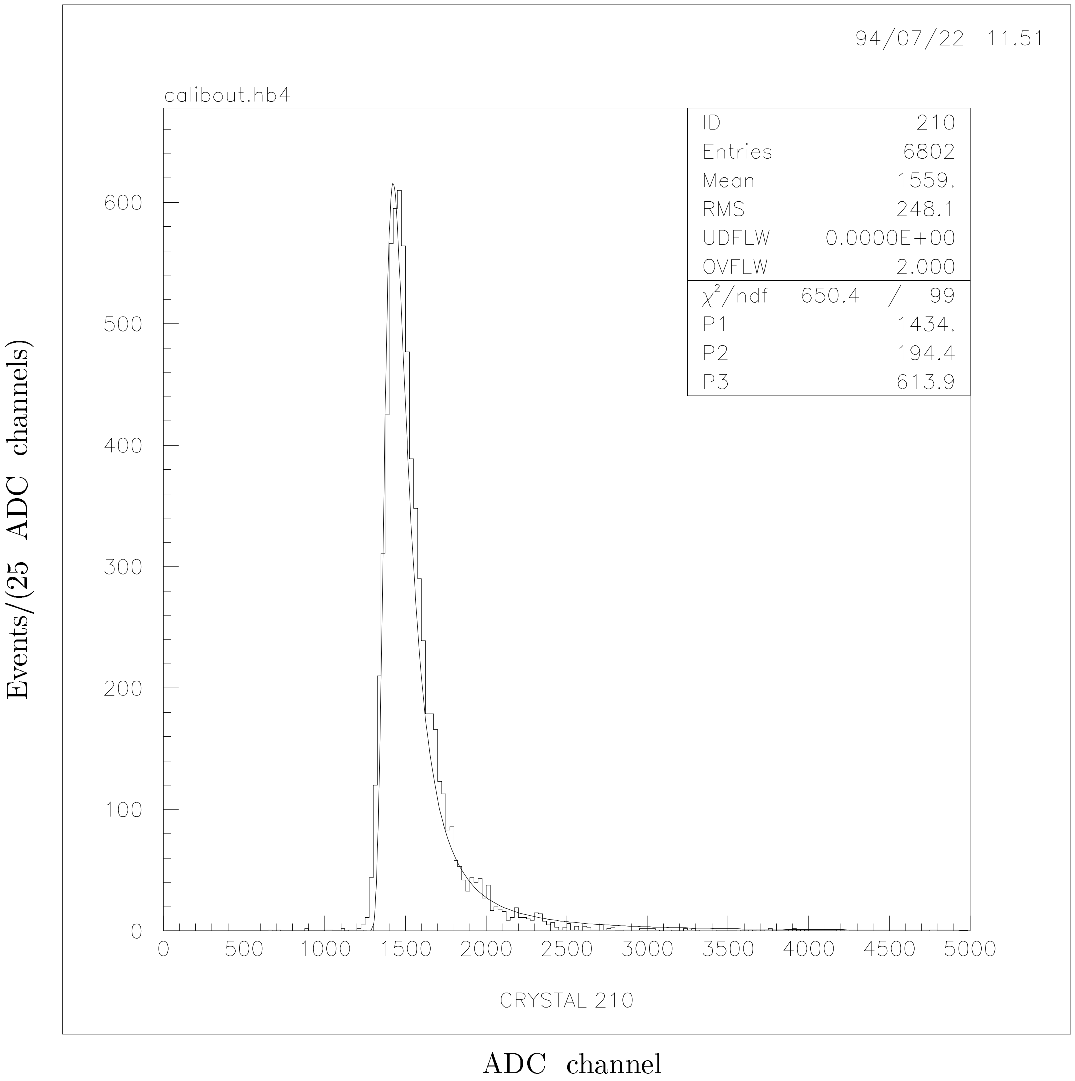

Figure 2.5: CsI ADC spectrum (crystal 210) for clean halo data. Peak position is taken to be 31 MeV.

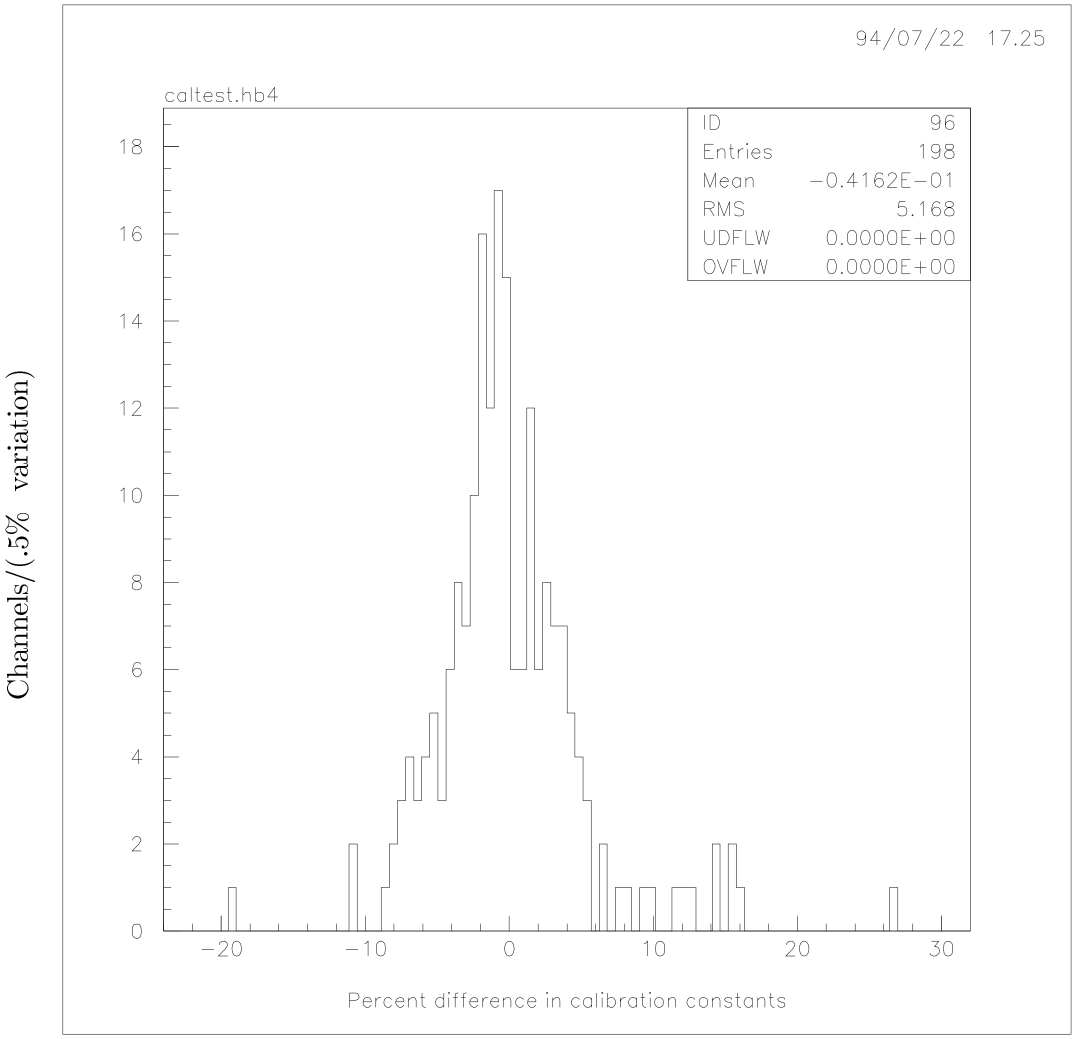

Figure 2.6: Variation of CsI crystal calibration constants between the beginning and end of the 1994 run.

CHAPTER 3

DATA

During the summers of 1991, 1992, and 1993, test runs of E852 demonstrated the capabilities of the components of the spectrometer. While they were very useful in developing the equipment and expertise, these runs did not produce physics data. The 1994 run of the AGS saw all parts of E852 (except the Čerenkov, C9) ready. During this 1000 hour run more than 200 million physics triggers were taken. These data are of high quality and enlightening about possible new physics. The 1995 run was of longer duration with less setup time needed. More than 700 million triggers were taken in winter/spring of 1995. This work includes only data from the 1994 run.

3.1 Data Collection

The 1994 proton run of the AGS was from April to the end of July. The first part of the run was dedicated to detector commissioning and trigger development. The LGD trigger processor was installed and operational by the end of June. Prior to that, 50 million physics triggers had been taken without an LGD requirement. The bulk of the neutral and (charged + neutral) data was collected during July. A summary of the recorded physics triggers is given in Table 3.1.

TABLE 3.1
NUMBER OF TRIGGERS TAKEN IN 1994 AND 1995 (M=10^6)

Trigger	1994 run	1995 run
0-0-0-E	14M	94M
1-1-1-η	47M	147M
0-2-2-η	48M	108M
1-3-3	42M	—
1-3-3-η	46M	265M
0-4-4	4M	96M
Total	197M	711M

The AGS runs with a spill cycle of about 3.2 seconds with the extracted beam coming during the first second. For each trigger taken, the appropriate analog-to-digital converters (ADCs) and time-to-digital converters (TDCs) are recorded by 6 SLAC Scanner Processors (SSPs) located in the MPS Fast Trailer and the LGD Electronics Hut. At the end of extracted beam, the master SSP (SSP0) collects the data from the other SSPs and sends it to the data acquisition computer (MPSDAQ) (figure 3.1). A program running on MPSDAQ sorts the SSP data and rebuilds individual events by combining the various ADC/TDC outputs from a specific trigger. All the events from a given spill are then recorded on 8mm magnetic tape. By this method, E852 recorded the triggers listed above on 300 tapes for the 1994 run and 1000 tapes for the 1995 run.

3.2 Data Processing

The raw data contain all the electronic information which was recorded for an event. These data must then be processed and the event reconstructed into a format under-

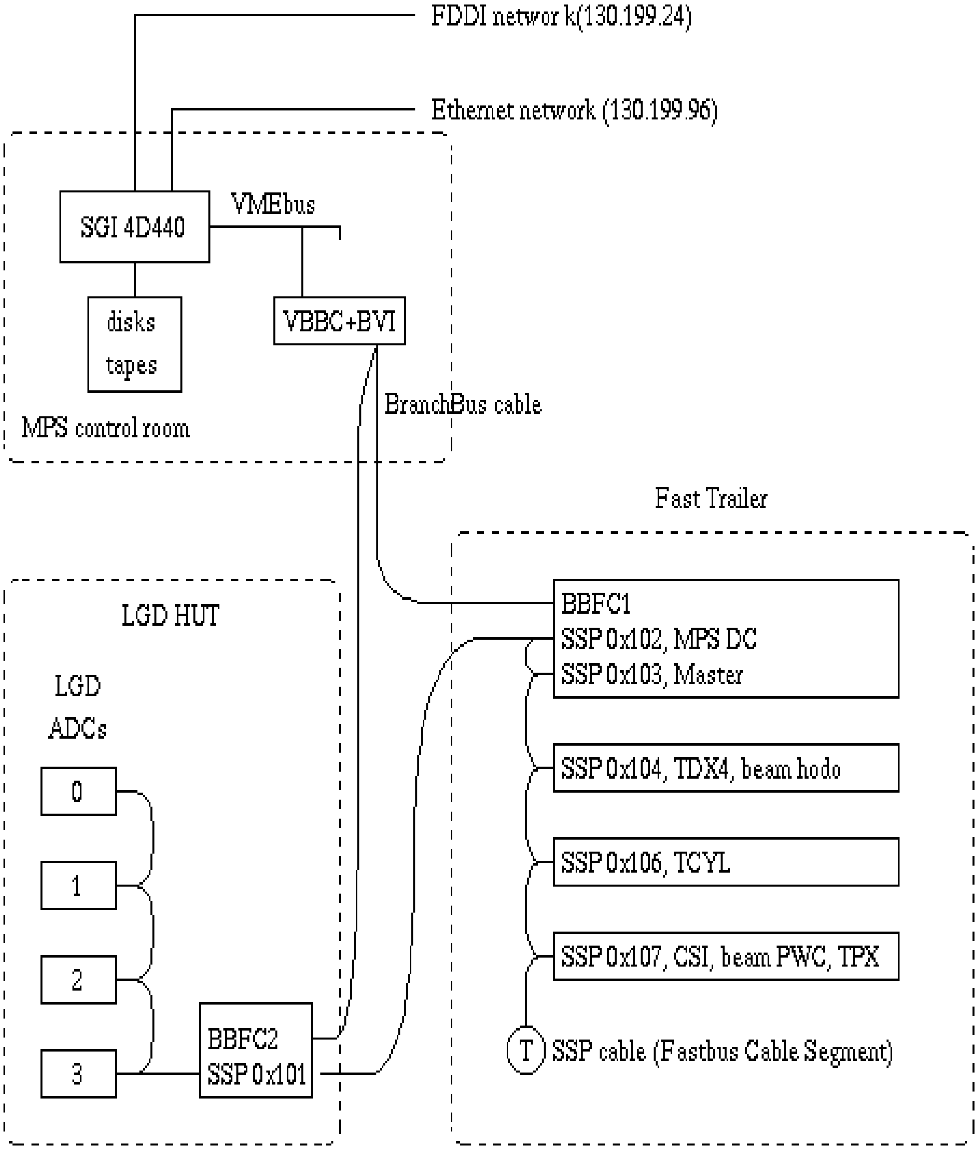

Figure 3.1: Configuration of the data acquisition system for E852.

standable to the experimenters. This was done with a program called a1pro. The data must also be reduced to a more selective subset. This involves several stages including bad-event rejection and topology selection.

3.2.1 Data Reconstruction

There were several important tasks for a1pro. These include data conversion and particle reconstruction. The electronic readout of ADC channels was converted from a channel number to a piece of a detector, for example a wire number or an LGD block number. For many detectors the ADC value was also converted to an energy.

Higher level reconstruction such as charged track reconstruction was done at this stage. The existing MPS pattern reconstruction and track fitting routines were upgraded and used for this. The pattern recognition routines [35, 36, 37] attempt to match drift chamber and PWC hits to a straight line in y and a circle in x. This gives a maximum number of tracks which may be reconstructed for the event. The track fitting routines attempt to find a vertex where the tracks meet and perform a momentum determination for the track. Tracks in TCYL are also reconstructed. These can be used in the vertex determination, but no momentum measurement is possible. Tracks which would not fit onto a vertex may be discarded.

Photon reconstruction for the lead glass detector can also be done here. However, due to later work on calibrations and clusterizing, this was redone. The photon reconstruction includes several stages [31]. A multiple-pass clusterizer first uses the lead glass hits to find clusters. A modified logarithmic weighting of energy in the blocks was used for the position finding. The reconstructed charged particles are then tracked to the LGD front face and all clusters within 20 cm transverse distance from a charged track are tagged as hadronic. All untagged clusters are then converted to photons by determining the vector from the event vertex to the cluster position with a lead glass depth correction.

Some minimum-bias cuts have been applied in a1pro. There is a requirement that the number of tracks found by the pattern recognition be at least the number of tracks determined by the trigger. Therefore, a 1-3-3-η trigger requires at least 3 downstream charged tracks for the event to continue through the reconstruction. A beam track must also be reconstructed before continuing.

The reconstruction of the 1994 data was performed primarily at Notre Dame with BNL concentrating on the 1-3-3-(no LGD) data from early in the run and Indiana University doing the LGD calibration. An elaborate system was designed at BNL with customization at Notre Dame to process the data with utilization of as many computers as possible. This was based on the Dispatcher system.

The Dispatcher is a program with several clients connected to it. One process generally connects to feed raw data to it. These data are then distributed to multiple processors running a1pro. Each event goes to only one processor. After reconstruction is completed, the event is returned to the Dispatcher as "cooked" data. One or more processes are connected to the Dispatcher to write out the data.

The production analysis system at Notre Dame consisted of several parts (figure 3.2). There was one input tape stacker which read 10 raw tapes in sequence and fed the data to the Dispatcher. The analyzer, a1pro, was run on 6 IBM RS6000 machines (one 380, three 370s, one 320 and one 220) and two Silicon Graphics Indigos. These eight processors were able to process about 18 events/second. The output was split by trigger type. Three output tape stackers recorded the 1-1-1, 0-2-2, and 1-3-3 triggers independently. The all-neutral events were written to disk and later saved on magnetic tape. This system ran with a duty cycle of better than 80% (including all day Christmas day) for 4 months to complete the majority of the 1994 production analysis processing.

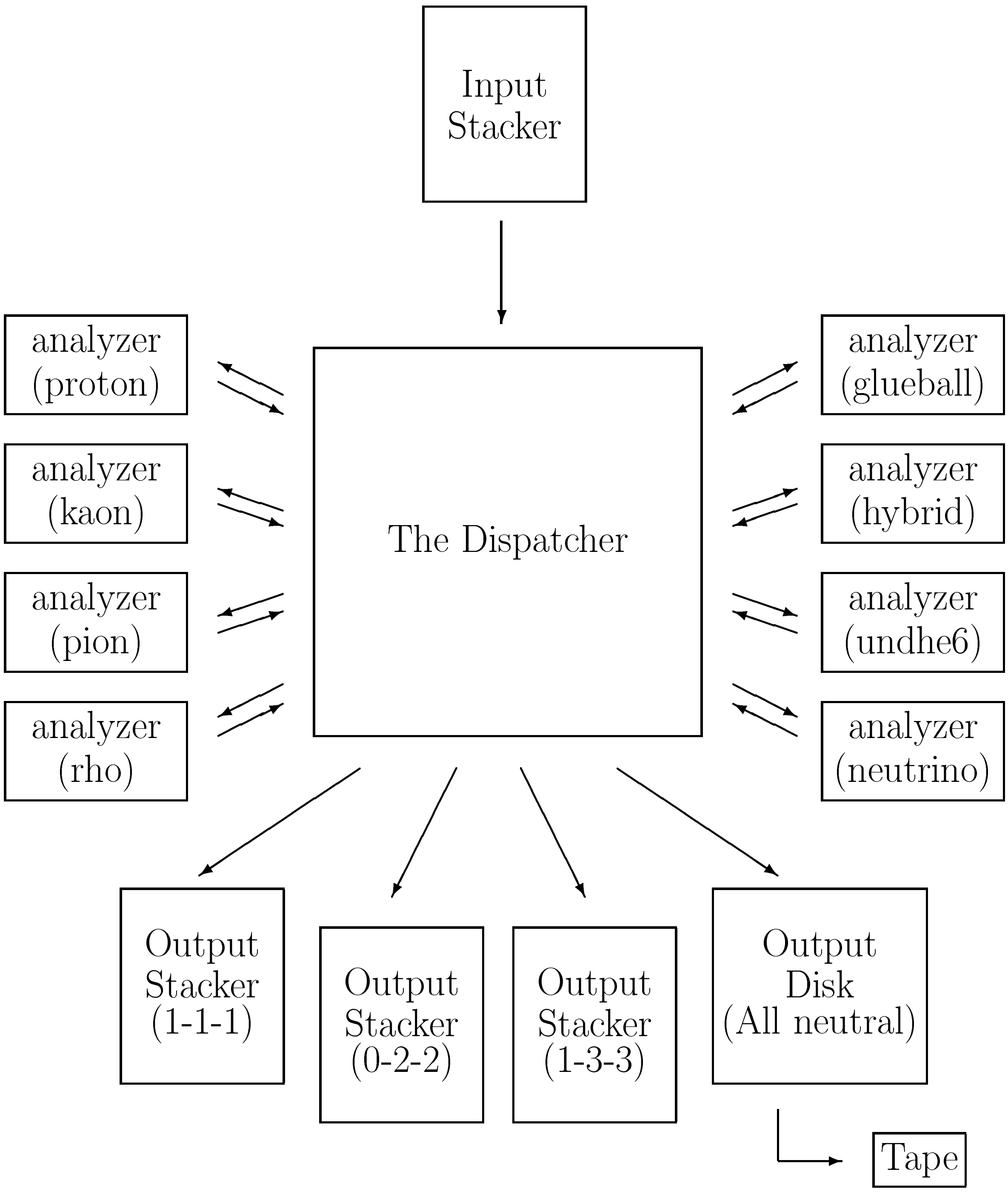

Figure 3.2: Schematic of the system used to process the 1994 data through the reconstruction code at Notre Dame

TABLE 3.2
NUMBER OF EVENTS AFTER EACH STAGE OF PROCESSING

1-3-3 Triggers	Production Analysis	Skim	Topology Selection	Kinematic Fitting
88M	38M	21M	890K	237K

3.2.2 Data Reduction

After the 1994 data were reconstructed by a1pro, they were processed through the program skimmer. This program applied several cuts to reduce the data. Events with an even number of downstream tracks were required to have a net charge of zero (neutron recoil) and those having an odd number of downstream tracks were required to have a net charge of -1 (proton recoil). This is referred to as a charge balance cut. All events with a hit in the DEA which did not have a hit in the corresponding section of CPVC were removed. This cut discarded events with photons which missed both the LGD and the CsI. Events with a neutral recoil were also discarded if the CsI had more than 160 MeV deposited in it. This was a very conservative cut which reduced the output size. No cut on the CsI was applied to proton recoil events at this stage. The number of 1-3-3-η events which were left after each stage of the processing is given in Table 3.2.

The 1-3-3 events which passed through the skim were required to have three downstream charged tracks which form a vertex and two untagged clusters in the LGD with a combined effective mass greater than 0.3 GeV/c^2. This topology cut nominally selected $\eta\pi^+\pi^-\pi^-p$ events. These events were then passed through a kinematic fitter, a modified version of the Berkeley bubble chamber fitter SQUAW [38]. A two constraint (2C) fit was performed with the gammas fit to π^0, η, or η' hypotheses and the total event missing mass fit to a recoil proton. Events were selected if a SQUAW fit to the hypothesis $\eta\pi^+\pi^-\pi^-p$ yielded a confidence level of greater than

10^{-4}.

3.3 Data Characteristics

Several questions need to be answered about the data set under study. Do we have the topology ($\eta\pi^+\pi^-\pi^-$) which is desired? Is the state under study ($f_1(1285)\pi^-$) present in the topology? Does the state decay ($f_1(1285) \rightarrow a_0\pi$) as previously seen? What other states exist in the data sample? These questions have been addressed in various studies.

3.3.1 Raw Data Analysis

Early studies were done to determine the existence of the $\eta\pi^+\pi^-\pi^- p$ topology in the E852 data. The $\gamma\gamma$ spectrum was plotted for events with 3 reconstructed tracks (1-3-3) and two untagged LGD clusters. The region for 0.3<M($\gamma\gamma$)<0.8 GeV/c^2 is shown in figure 3.3. A requirement was made that the missing-mass-squared (MM^2) for the events be in the range 0<MM^2<3.5 GeV^2/c^4. The η is clearly seen. This establishes the existence of $\eta\pi^+\pi^-\pi^-$ events in the data set. When additional cuts are applied to simulate the final data set, a signal to background ratio for the η is found to be 1.2 to 1.

The goal of this work is the study of the $f_1(1285)\pi^-$ system in this topology. The $\gamma\gamma\pi^+\pi^-$ mass spectrum for reconstructed data is plotted in figure 3.4. There are two entries per event. The same missing-mass-squared requirement is used. The $\gamma\gamma$ mass is restricted to the range .5<M($\gamma\gamma$)<.6 GeV/c^2. An additional requirement is applied; the azimuthal angles (ϕ) of the missing momentum and of the TCYL track must be less than 20° apart. This cut is detailed further in section 3.4.2. The $\eta'(958)$ is seen just below 1.0 GeV/c^2. A clear signal in the 1.28 GeV/c^2 region is also seen. This is strong evidence for $f_1(1285)$ and/or $\eta(1295)$ in the sample.

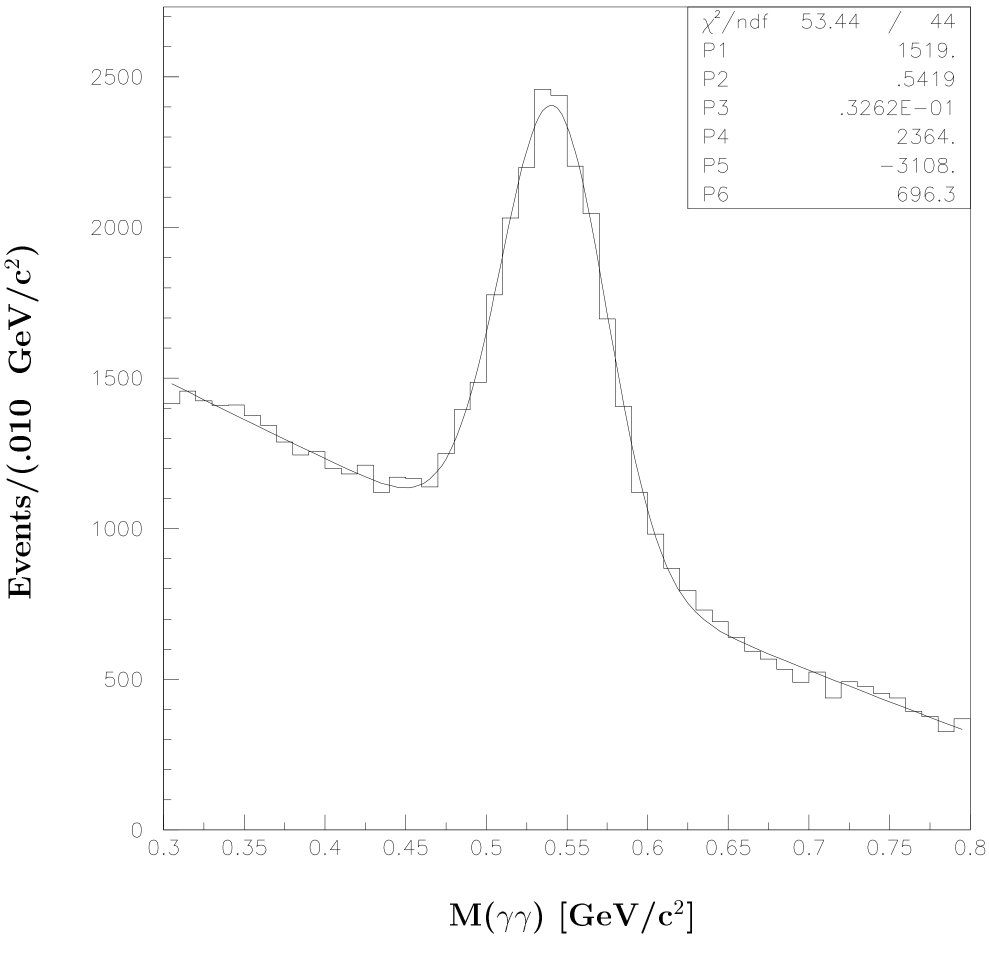

Figure 3.3: $\gamma\gamma$ mass spectrum in η region for 1-3-3 events

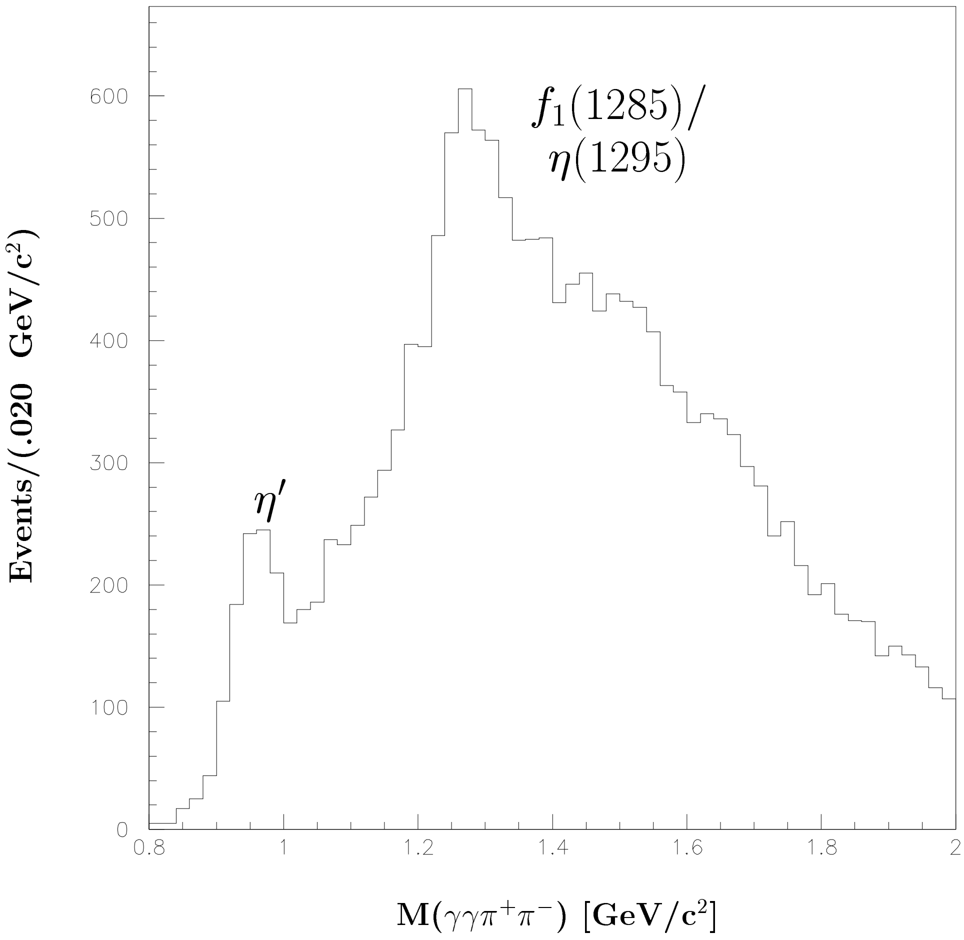

Figure 3.4: $\gamma\gamma\pi^+\pi^-$ mass spectrum for a sample of 1-3-3-η events (2 entries per event)

3.3.2 Fit Data Analysis

Once the existence of $f_1(1285)\pi^-$ events was established, the data were reexamined after kinematic fitting. There were 237,000 events which fit the hypothesis of $p\eta\pi^+\pi^-\pi^-$ with a confidence level greater than 10^{-4}. The $\gamma\gamma$ are fit to an η. The η and $\pi^{\pm}$ four-vectors are used for a total event fit with a missing proton. There are no other intermediate mass constraints. The resulting $\eta\pi^+\pi^-$ spectrum shows much narrower η' and $f_1(1285)/\eta(1295)$ peaks (figure 3.5). The measured width (Γ_{BW} = .056 GeV/c^2) of the peak at 1.28 GeV/c^2 is consistent with Monte Carlo events generated with a Breit-Wigner width of .024 GeV/c^2 and processed through the experimental simulation, reconstruction and kinematic fitting (Γ_{BW} = .048 GeV/c^2). The measured peak position ($mass$ = 1.278) is consistent with the the Particle Data Group value of $1.282 \pm .0007$ GeV/c^2 [18].

The natural width of the $\eta'(958)$ is very small ($\Gamma = .000201 \pm .000016$ GeV/c^2) and can be used as a kinematic constraint. However, the $f_1(1285)$ is significantly wider ($\Gamma = .024 \pm .0013$ GeV/c^2) [18] and the mass is not used as a constraint. Another author has done a concurrent analysis of the $\eta'(958)\pi^-$ data [39] with the η' intermediate mass used as an additional constraint. All events with either $\eta\pi^+\pi^-$ mass less than 1.02 GeV/c^2 were removed from the data set for the $f_1(1285)\pi^-$ analysis. This removes essentially all of the $\eta'\pi^-$ events.

The Particle Data Group (PDG) lists $\eta\pi^+\pi^-$ as the largest decay mode of the $f_1(1285)$ [18]. Most of these decays are listed as going through the intermediate decay $a_0(980)\pi$. This is supported by many previous experiments [40, 41, 42, 43]. The $\eta(1295)$ has similar decay modes. The $f_1(1285)$ and $\eta(1295)$ have also been seen in studies of the reaction

$$\pi^- p \to \eta\pi^+\pi^- n \tag{3.1}$$

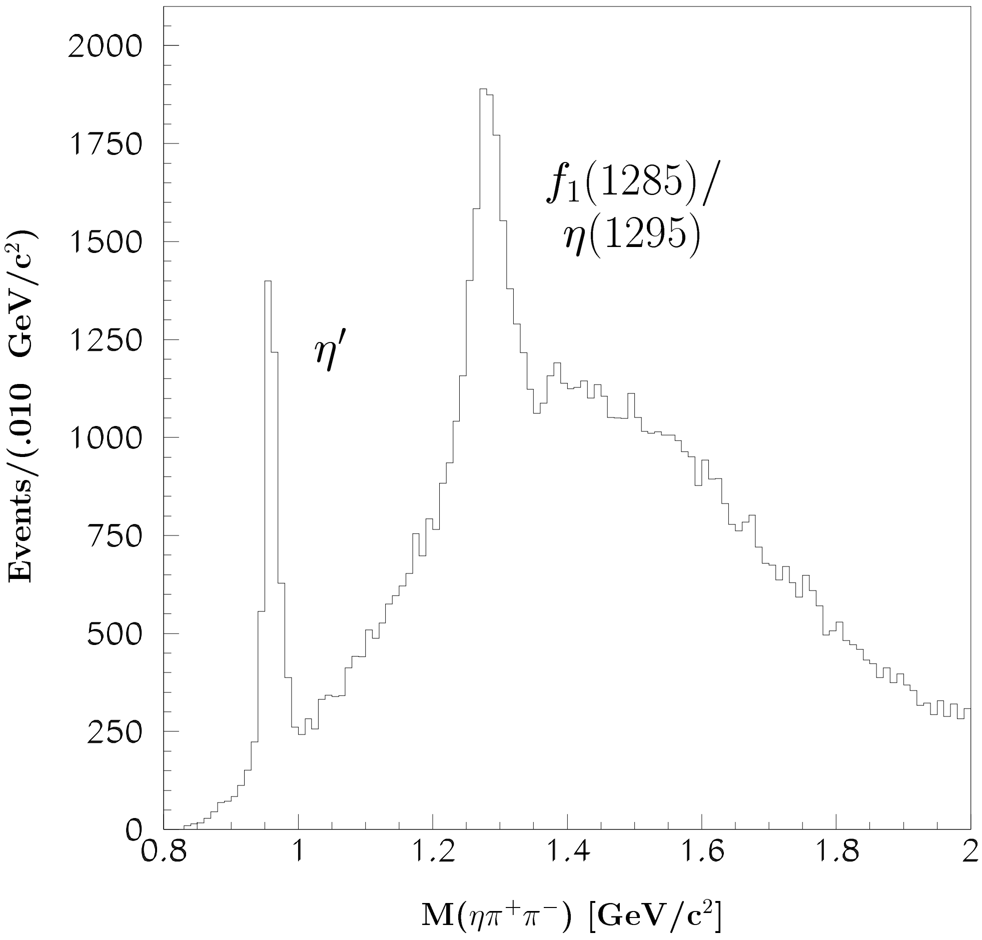

Figure 3.5: $\eta\pi^+\pi^-$ mass spectrum after SQUAW kinematic fitting (2 entries per event)

in the E852 data [44, 45]. The $\eta\pi$ spectrum for the $\eta\pi^+\pi^-\pi^-$ data set is shown in figure 3.6. There are three entries per event with no selection on the π. The $a_0(980)$ is seen as expected.

There is a strong correlation between the $a_0(980)$ peak in the $\eta\pi$ mass spectrum and the $f_1(1285)/\eta(1295)$ peak in the $\eta\pi^+\pi^-$ spectrum. A selection is made on $\eta\pi$ mass within the range .93<M($\eta\pi$)<1.03 GeV/c^2. For each $\eta\pi^-$ selected the $\eta\pi^+\pi^-$ mass is plotted. For each $\eta\pi^+$ selected both $\eta\pi^+\pi^-$ masses are plotted. A given $\eta\pi^+\pi^-$ mass is included only once. The resulting spectrum is shown in figure 3.7. The $f_1(1285)/\eta(1295)$ peak remains strong and the background is greatly suppressed. Figure 3.8 shows a plot of $M^2(\eta\pi^+)$ versus $M^2(\eta\pi^-)$ for $\eta\pi^+\pi^-$ combinations with 1.23<M($\eta\pi^+\pi^-$)<1.33 GeV/c^2. An event may be included twice if both $\eta\pi^+\pi^-$ combinations fall within the criteria. Bands corresponding to the $a_0^+(980)$ and $a_0^-(980)$ can be clearly seen. It has been demonstrated that the reaction of Eq. 1.1 is available for study in the E852 data.

The final question about the data sample to be explored is the existence of additional states in the set. The particles of the $\eta\pi^+\pi^-\pi^-$ sample can be combined in many ways as a result of different reactions. The primary possibilities for resonant subsystems are $\eta\pi^+\pi^-$, $\pi^+\pi^-\pi^-$, $\eta\pi$, and $\pi^+\pi^-$. The combinations $\eta\pi^-\pi^-$ and $\pi^-\pi^-$ are of negligible interest.

It has already been shown that there is $\eta'(958)$ in the $\eta\pi^+\pi^-$ spectrum. These events have been subsequently removed. The peak in the $f_1(1285)/\eta(1295)$ region is the only other obvious structure in the $\eta\pi^+\pi^-$ spectrum of figure 3.5. The E/ι region above 1.4 GeV/c^2, in particular, shows no definite signs of enhancement. The $a_0(980)$ has been seen in the $\eta\pi$ spectrum. While there is a strong correlation between the $a_0(980)$ and the $f_1(1285)$, the possibility remains of $a_0(980)$ production as part of a different decay chain. There is also evidence for the $a_2^-(1320)$ in the $\eta\pi^-$ spectrum which is essentially eliminated by the final cuts.

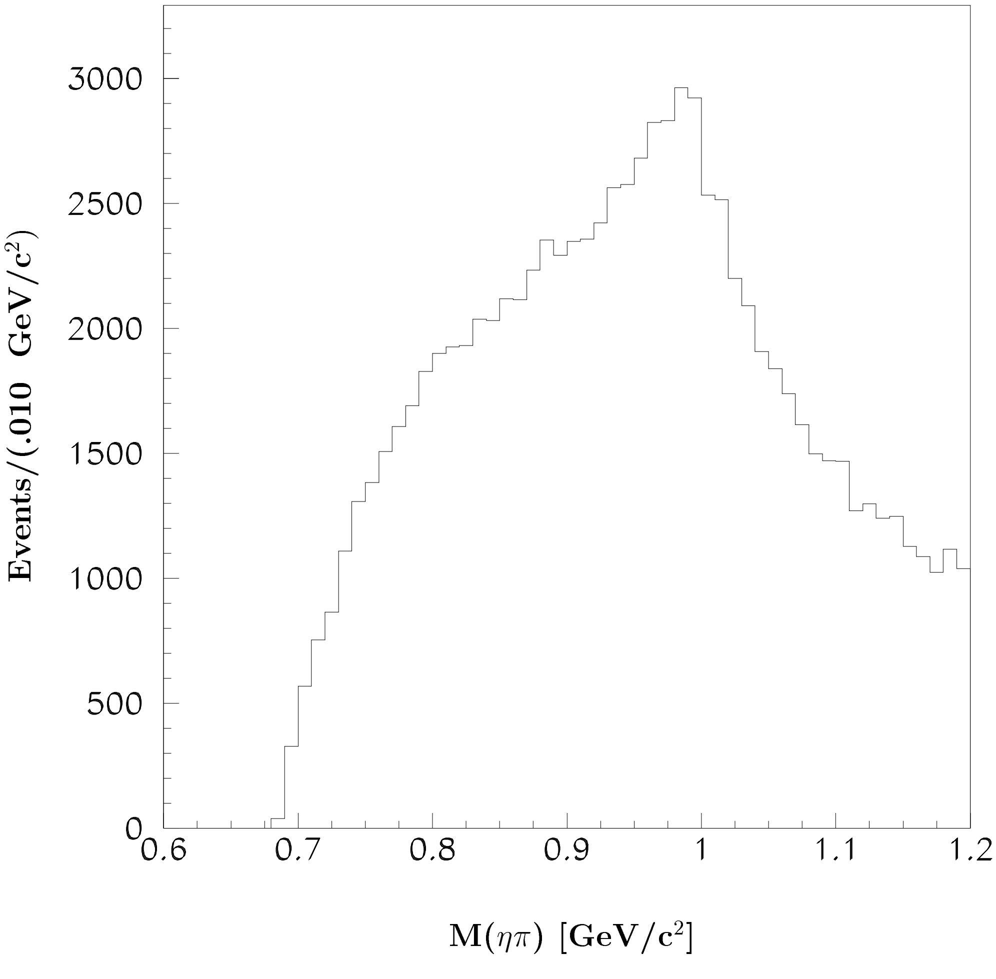

Figure 3.6: $\eta\pi$ mass spectrum after SQUAW kinematic fitting (3 entries per event)

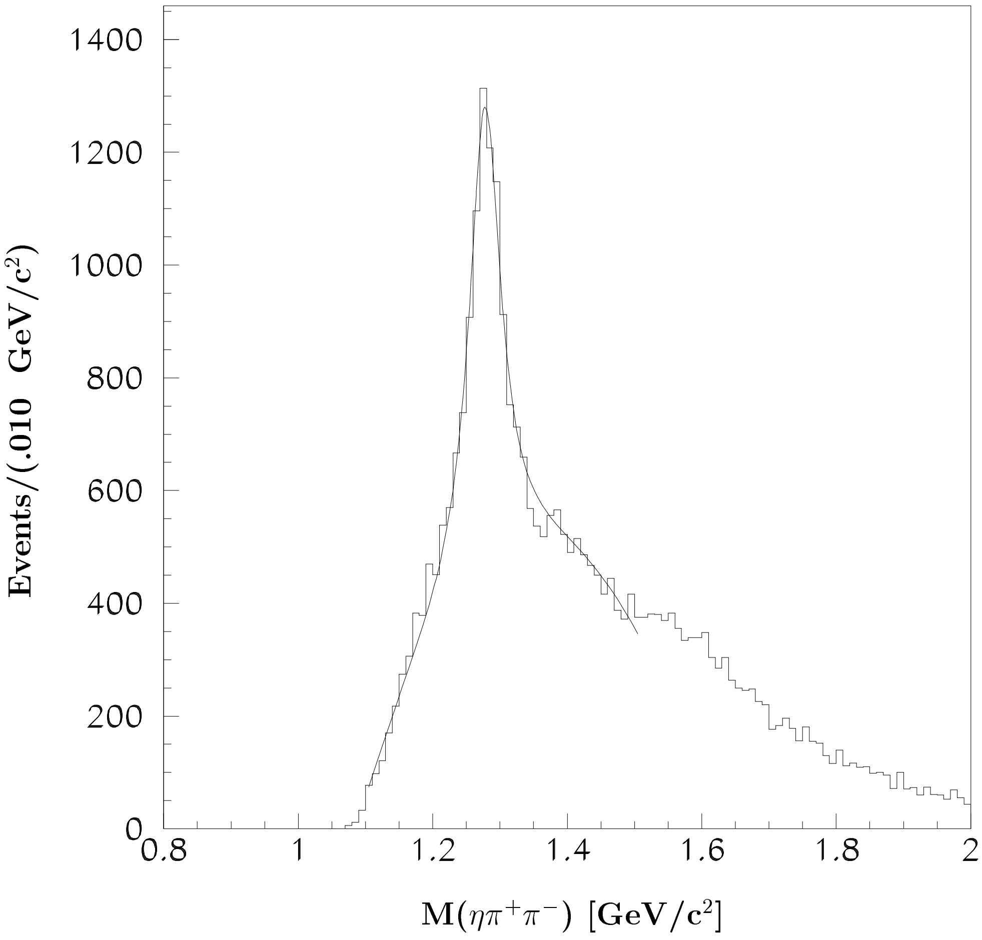

Figure 3.7: $\eta\pi^+\pi^-$ mass spectrum after cut on $\eta\pi$ mass (.93<M($\eta\pi$)<1.03 GeV/c^2) (1 or 2 entries per events) (See text for details.)

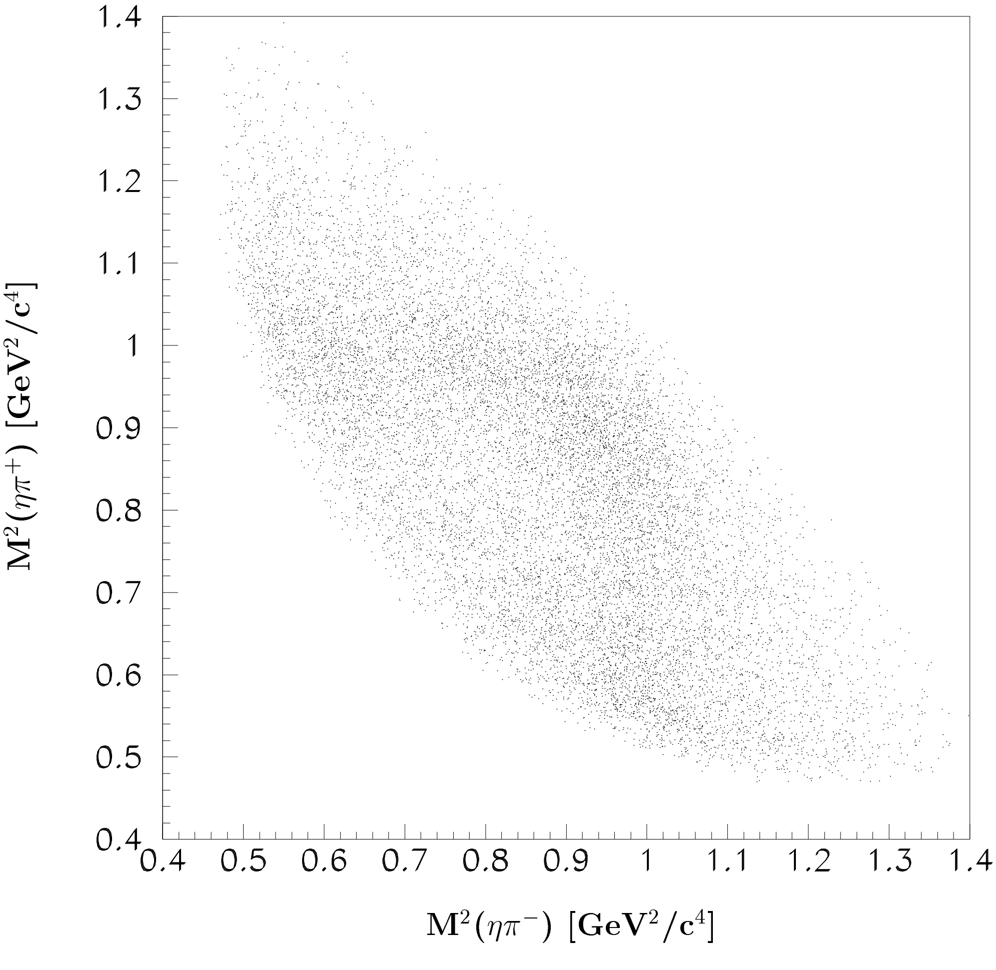

Figure 3.8: Dalitz plot for $1.22 < M(\eta\pi^+\pi^-) < 1.33$ GeV/c^2. Enhancements can be seen at the $a_0(980)$ mass corresponding to $f_1(1285) \rightarrow a_0(980)\pi$

The $\pi^+\pi^-$ and $\pi^+\pi^-\pi^-$ mass spectra are shown in figure 3.9. The $\rho^0(770)$ is visible in the $\pi^+\pi^-$ spectrum. There may be $a_2^-(1320)$ in the $\pi^+\pi^-\pi^-$ spectrum. There is some correlation between these resonances. This has been demonstrated by cutting on the $a_2^-(1320)$ peak ($1.15<\mathrm{M}(\pi^+\pi^-\pi^-)<1.45$ GeV/c^2) in the $\pi^+\pi^-\pi^-$ mass distribution and plotting the $\pi^+\pi^-$ mass distribution (figure 3.10(a)). The $\rho^0(770)$ peak is greatly enhanced. The $a_2^-(1320)$ peak can also be enhanced by cutting on the $\rho^0(770)$ peak (figure 3.10(b)). This is expected since the primary decay of the $a_2(1320)$ is through $\rho\pi$. These plots show the possibilities within the $\eta\pi^+\pi^-\pi^-$ data which need to be accounted for in this analysis.

3.4 Data Selection

The quality of the sample can be improved by applying various selection criteria which minimize the background events and keep as many signal events as possible. Background events can be badly reconstructed events, non-η events, Δ recoil events, and non-$f_1(1285)\pi^-$ events. Several such cuts have already been applied to the sample. There was a requirement that the number of charged downstream tracks reconstructed agree with the trigger (i.e. 3 reconstructed tracks for 1-3-3 triggers). There was a requirement of 2 untagged LGD clusters with an effective mass near the η ($.3<\mathrm{M}(\gamma\gamma)<.8$ GeV/c^2). Events also must be kinematically consistent with the hypothesis $\eta\pi^+\pi^-\pi^-p$.

Other basic requirements must be met. The DEA/CPVC cut described in Section 3.2.2 removes events with a photon which missed the lead glass detector. Portions of the data which were deemed unusable were removed. This included data with the LGD in the wrong position, the LGD uncalibrated and the target not filled with liquid hydrogen. The event vertex was also required to be reconstructed within the hydrogen target. All of these simple cuts have been applied to the data

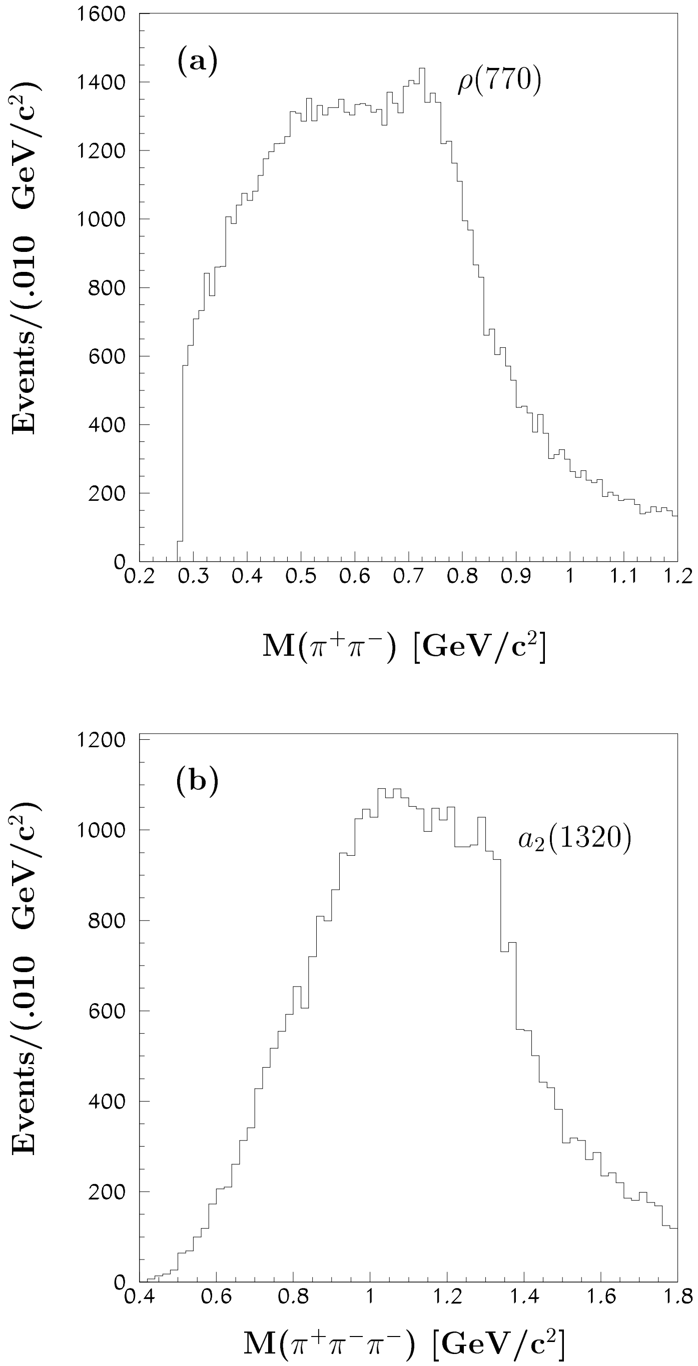

Figure 3.9: (a) $\pi^+\pi^-$ mass spectrum (2 entries per event); and (b) $\pi^+\pi^-\pi^-$ mass spectrum for $\eta\pi^+\pi^-\pi^-p$ events.

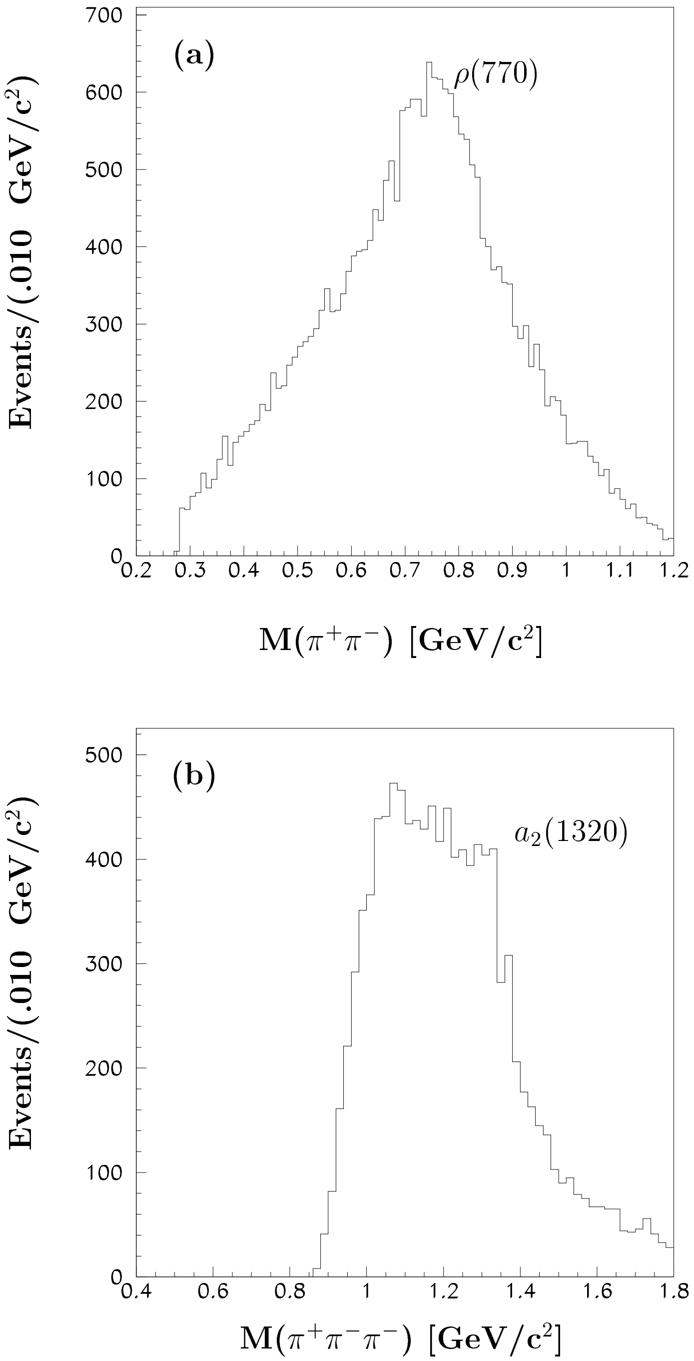

Figure 3.10: (a) $\pi^+\pi^-$ mass spectrum with a_2^- cut (1.15< $M(\pi^+\pi^-\pi^-)$ <1.45 GeV/c^2) (2 entries per event); and (b) $\pi^+\pi^-\pi^-$ mass spectrum with $\rho^0(770)$ cut (.72< $M(\pi^+\pi^-)$ <.82 GeV/c^2) for $\eta\pi^+\pi^-\pi^- p$ events.

presented in Section 3.3.2. They cause no real bias in the data sample and reject significant background. More restrictive cuts and their justification are presented in the following subsections.

3.4.1 *Fit Confidence Level*

The SQUAW kinematic fitter returns a χ^2 and a confidence level (CL) for each hypothesis. The confidence level distribution for the $\eta\pi^+\pi^-\pi^-p$ data sample is shown in figure 3.11. This sample is a mixture of real $\eta\pi^+\pi^-\pi^-p$ events and background. The true $\eta\pi^+\pi^-\pi^-p$ events should have confidence levels uniformly distributed from 0 to 1. The excess of events near the lower end of the distribution is primarily due to the background. A cut on the confidence level of 0.1 (10%) has been applied in selecting the data sample. This cut will eliminate approximately 10% of the real events, but should remove a much higher percentage of background. This cut should greatly improve the signal-to-background ratio for the sample.

The MM^2 distribution for the sample can be a good indicator of the quality of the data. For most of this analysis (other than section 3.3.1) no cut is applied on the MM^2. The MM^2 for properly reconstructed proton recoil events should be centered at the proton mass squared ($M^2(p) = 0.88$ $\mathrm{GeV}^2/\mathrm{c}^4$). The expected width will depend on the experimental resolution. The effect of the confidence level cut on the MM^2 distribution is shown in figure 3.12. The unfitted four-vectors have been used to calculate the MM^2. This cut is related to a MM^2 cut since events farther away from the proton ($\mathrm{MM}^2 = .88$ $\mathrm{GeV}^2/\mathrm{c}^4$) will have a lower confidence level. The fit confidence level requirement of CL>0.1 is used for the final data selection.

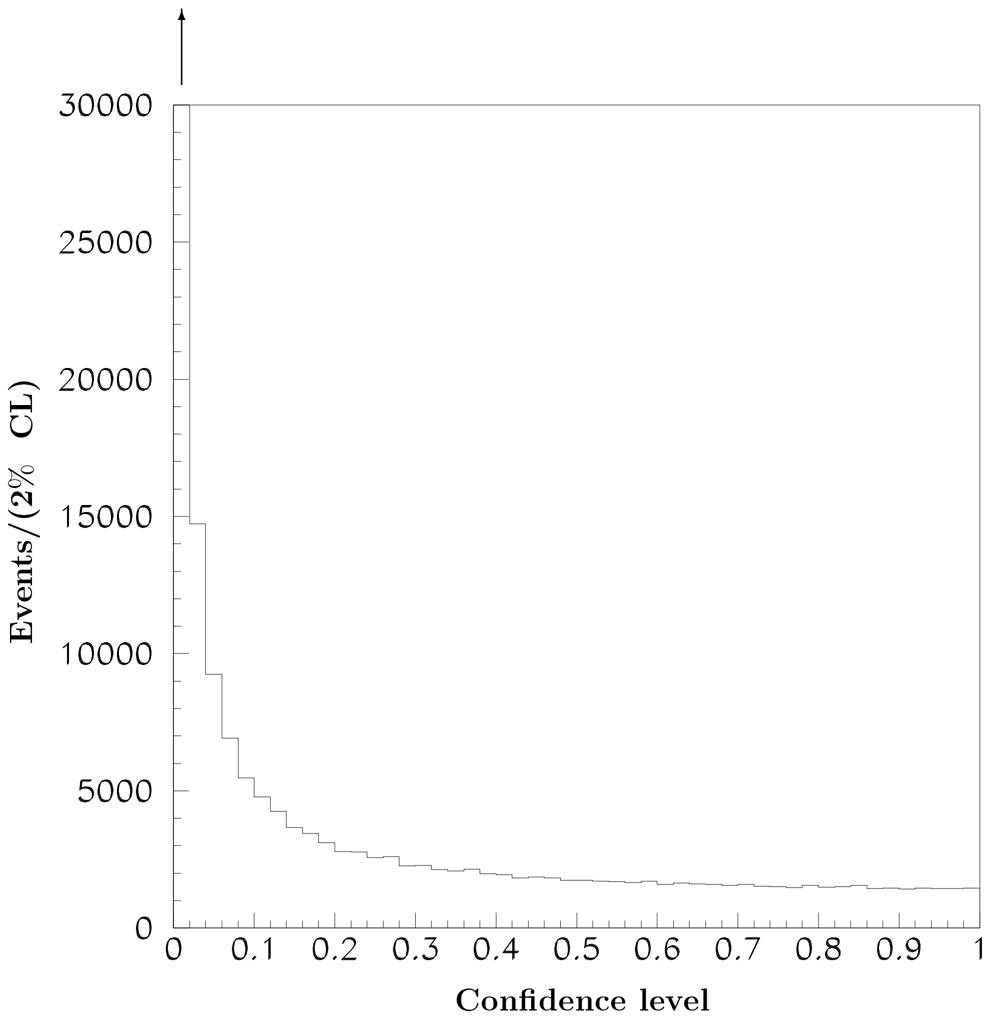

Figure 3.11: Fit confidence level for events fitting the $\eta\pi^+\pi^-\pi^-p$ hypothesis.

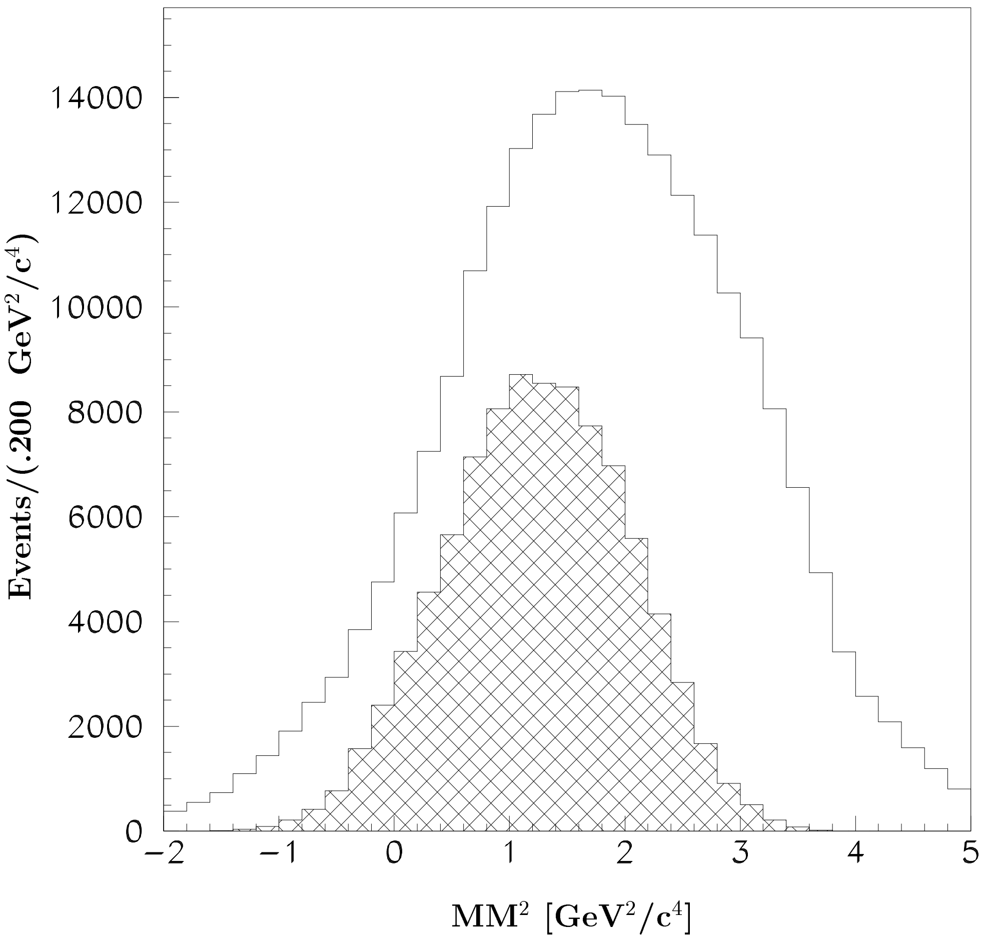

Figure 3.12: Effect of fit confidence level cut upon MM^2. The unhatched histogram is the MM^2 distribution for all $\eta\pi^+\pi^-\pi^- p$ events with fit confidence level $> 10^{-4}$. The hatched histogram is for events with fit confidence level $> .1$.

3.4.2 Azimuthal Angle

The azimuthal angle (ϕ) of a track in the MPS reference frame is defined as the angle from the positive x-axis to the track projection into the x-y plane. This gives ϕ=0° for the positive x axis and ϕ=90° for the positive y axis. The azimuthal angle of the TCYL track is well determined by the wire location. There is a strong correlation between the azimuthal angles of the TCYL track and the missing momentum in the fit (figure 3.13). This is unsurprising since the TCYL track and the fit missing momentum are both expected to represent the recoil proton. The effect of the magnetic field on the proton trajectories is small because the outer radius of TCYL is relatively small (9.5 cm). In particular, the azimuthal angle is not changed by the magnetic field for angles along either the x or y axis (ϕ=0°, 90°, 180°, 270°).

The events which do not have a strong correlation in ϕ most likely involve a Δ recoil or are mis-reconstructed (i.e.. missing a particle or with an extra particle). These events are discriminated against with a requirement that the azimuthal angle between the TCYL track (ϕ_{TCYL}) and the fit missing momentum (ϕ_{MM}) be less than 20° ($|\phi_{TCYL} - \phi_{MM}| < 20°$). The effect of this cut on the MM^2 distribution is seen in figure 3.14. The events with $\Delta\phi < 20°$ have a MM^2 distribution closer to the proton MM^2 than the events with $\Delta\phi > 20°$.

There is no requirement on the match between the polar angles (θ) of the TCYL track and missing momentum. This is due to the fact that there is not a strong correlation between them as was seen in the azimuthal angles in figure 3.13. There are three major reasons for this. The TCYL track polar angle is dependent upon the charge division of TCYL and is not as well determined. The polar angle of the fit missing momentum has a much larger error since it is determined by the small difference between two large numbers. Also, the polar angle can be more affected by the magnetic field than the azimuthal angle.

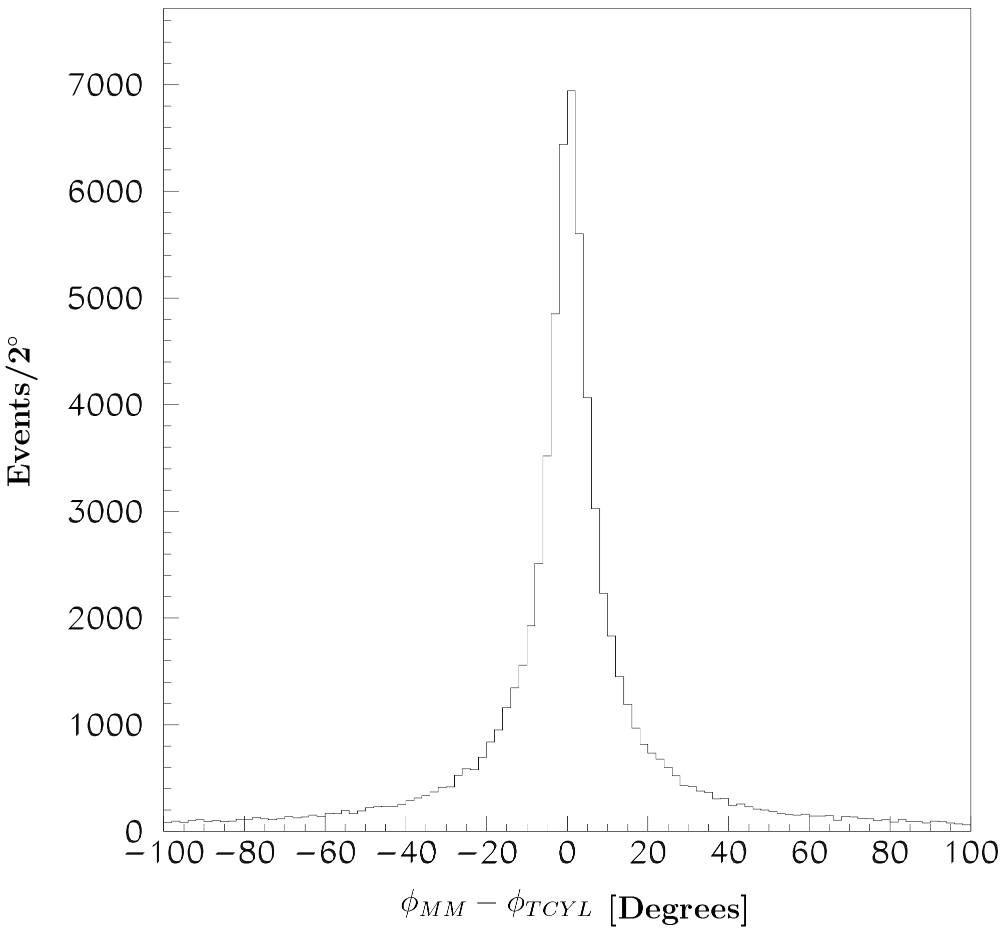

Figure 3.13: Distribution of the difference between the azimuthal angles of the fit missing momentum and the track in TCYL

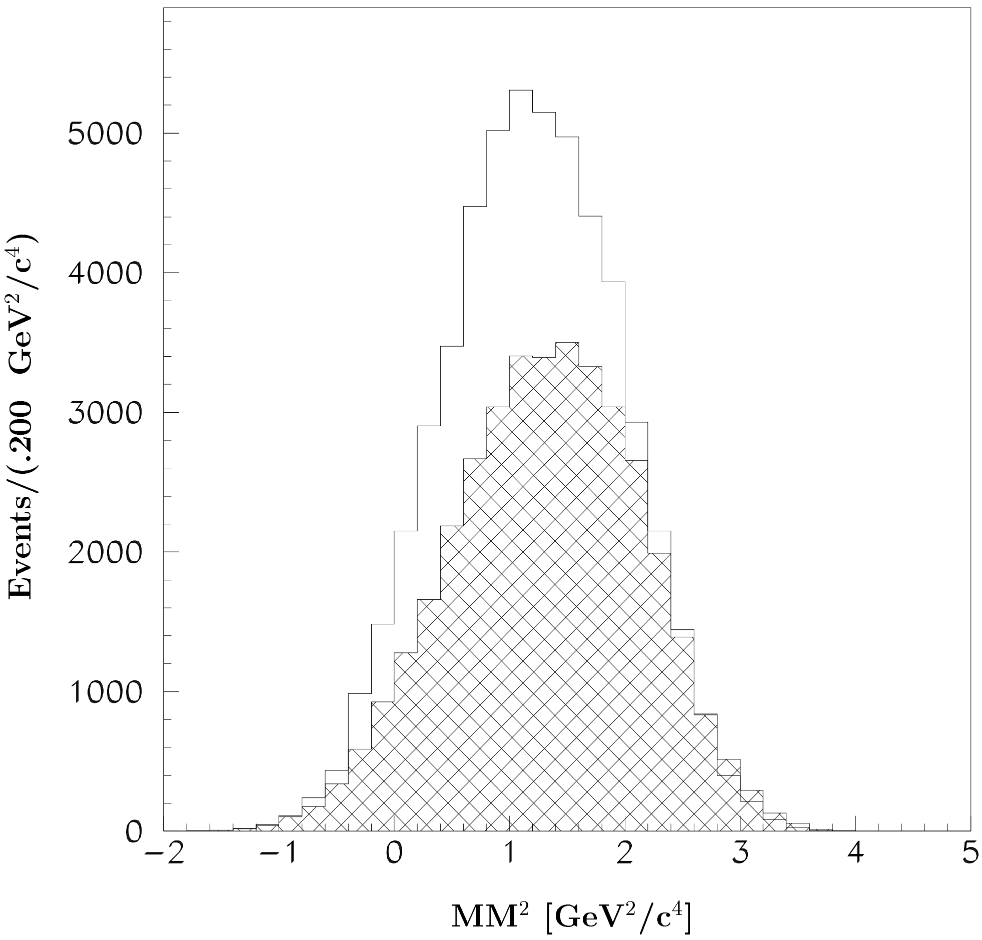

Figure 3.14: Effect of $\Delta\phi$ cut upon MM^2. The unhatched histogram is the MM^2 distribution for all events with $\Delta\phi < 20°$. The hatched histogram is for all events with $\Delta\phi > 20°$.

3.4.3 *Untagged CsI*

The partial-wave analysis of this system assumes the data to consist exclusively of proton-recoil events. Quite a bit of work has been done to remove non-proton-recoil events. Several cuts reduce the Δ recoil events in the sample. Both the fit confidence level and the $\Delta\phi$ requirements should do this. However, they may not be sufficient. The CsI detector was built for the purpose of vetoing such events. The decay $\Delta^+ \to p\pi^0$ should produce a wide angle π^0 which decays to $\gamma\gamma$. These photons will hit the CsI and deposit energy. A cut on the energy deposited in the CsI should remove these events.

The problem for the 1-3-3 events arises from the recoil proton. A recoil proton which passes through TCYL (a trigger requirement) will almost certainly deposit energy in the CsI. Therefore a system has been developed to track all TCYL tracks and all other charged tracks to the CsI volume and tag neighboring blocks. These blocks are then ignored in the CsI energy summation. A requirement of less than 20 MeV of untagged energy in the CsI is made on the data. The effect of this cut on the MM^2 distribution is seen in figure 3.15. This requirement removes some good events, but helps ensure a clean sample for the partial-wave analysis.

3.4.4 $f_1(1285)$ *Cut*

The goal of this work is the analysis of the $f_1(1285)\pi^-$ system. Therefore, an enriched sample of $f_1(1285)\pi^-$ events is desired. A selection criterion that at least one of the two $\eta\pi^+\pi^-$ masses lie within the $f_1(1285)$ peak ($1.23<\mathrm{M}(\eta\pi^+\pi^-)<1.33$ GeV/c^2) is applied. The effect of this cut on the $\eta\pi^+\pi^-$ spectrum is shown in figure 3.16. The $\eta'\pi^-$ cut (Section 3.3.2) causes the removal of some events in the $f_1(1285)$ peak. This cut dramatically reduces the non-$f_1(1285)\pi^-$ events while retaining most of the desired events. However, it does limit the scope of this analysis to the

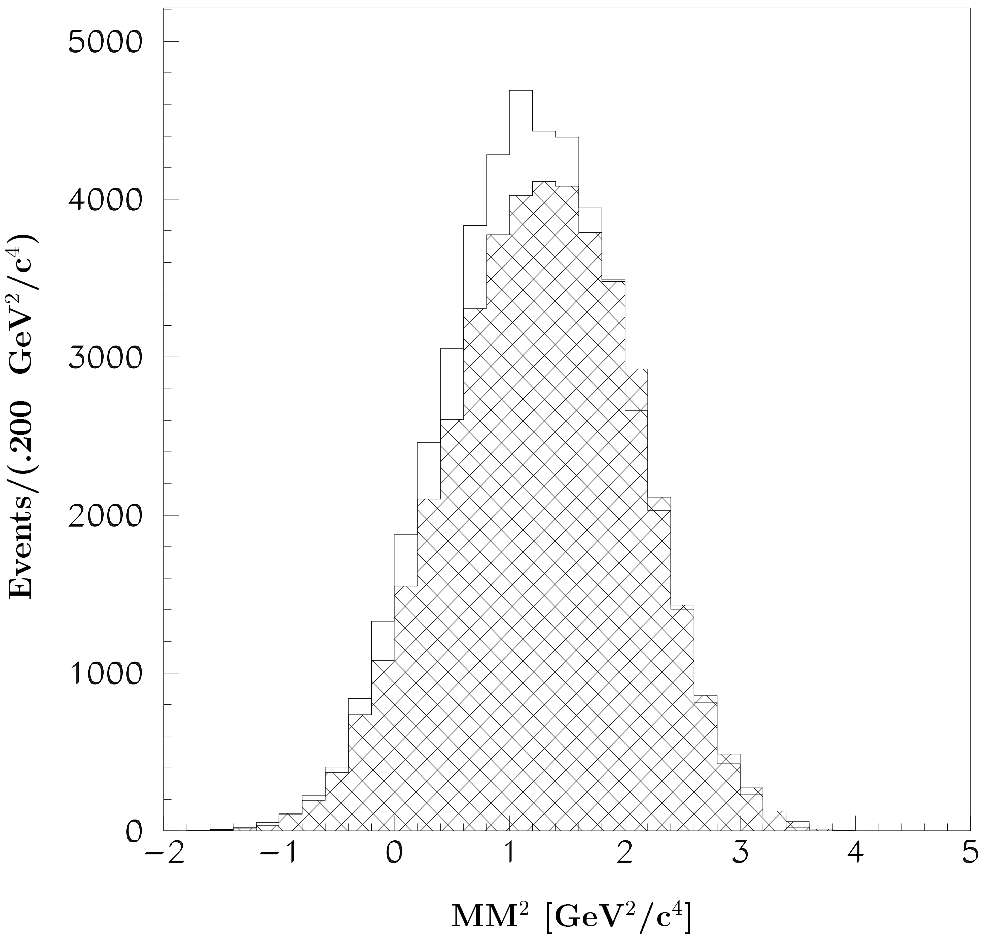

Figure 3.15: Effect of the CsI cut upon MM^2. The unhatched histogram is the MM^2 distribution for all events with untagged CsI energy $<$ 20 MeV. The hatched histogram is for all events with untagged CsI energy $>$ 20 MeV.

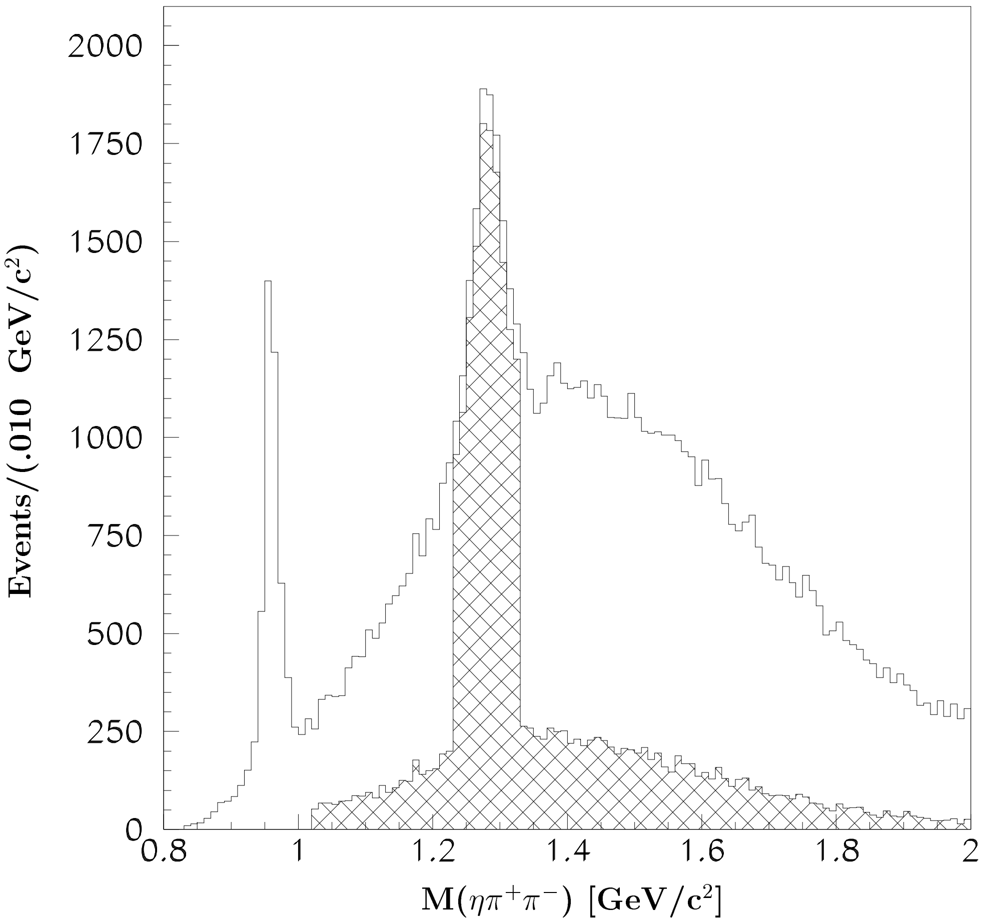

Figure 3.16: The $\eta\pi^+\pi^-$ mass distribution with (hatched) and without (unhatched) the $f_1(1285)$ cut.

$f_1(1285)\pi^-$ system. Any conclusions about other states in the $\eta\pi^+\pi^-\pi^-$ data must be limited.

3.4.5 Final Data Set

Once the selection criteria are determined, the final data set can be examined. There are actually two final data samples to be further analyzed. The two samples are without and with the cut on the energy deposited in the CsI. The cuts for the two samples are listed in Table 3.3. The $\eta\pi^+\pi^-\pi^-$ mass distributions for both final data sets are given in figure 3.17. The distributions are unremarkable enough that no initial conclusions are drawn about the existence of resonances within the data sample. The -$t' = -(t - t_{min})$ distribution for this sample is given in figure 3.18. The trigger requirement gives a very low acceptance below .08 GeV^2. A fit to the region .1<-t'<.8 with the function $e^{bt'}$ gave $b = (4.19 \pm .02)$ GeV^2.

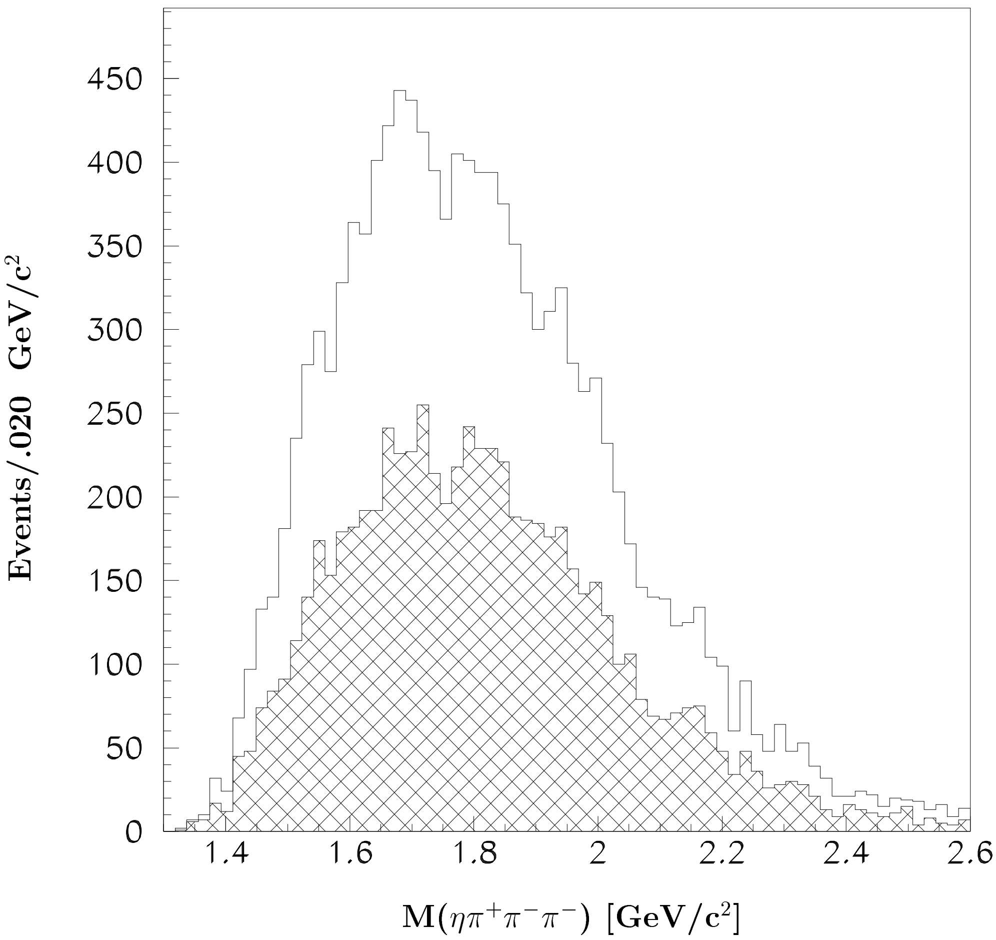

Figure 3.17: $\eta\pi^+\pi^-\pi^-$ mass spectrum for the final data sets. The unhatched distribution is for the primary data sample, while the hatched distribution is for the secondary data sample which includes the cut on energy deposited in the CsI.

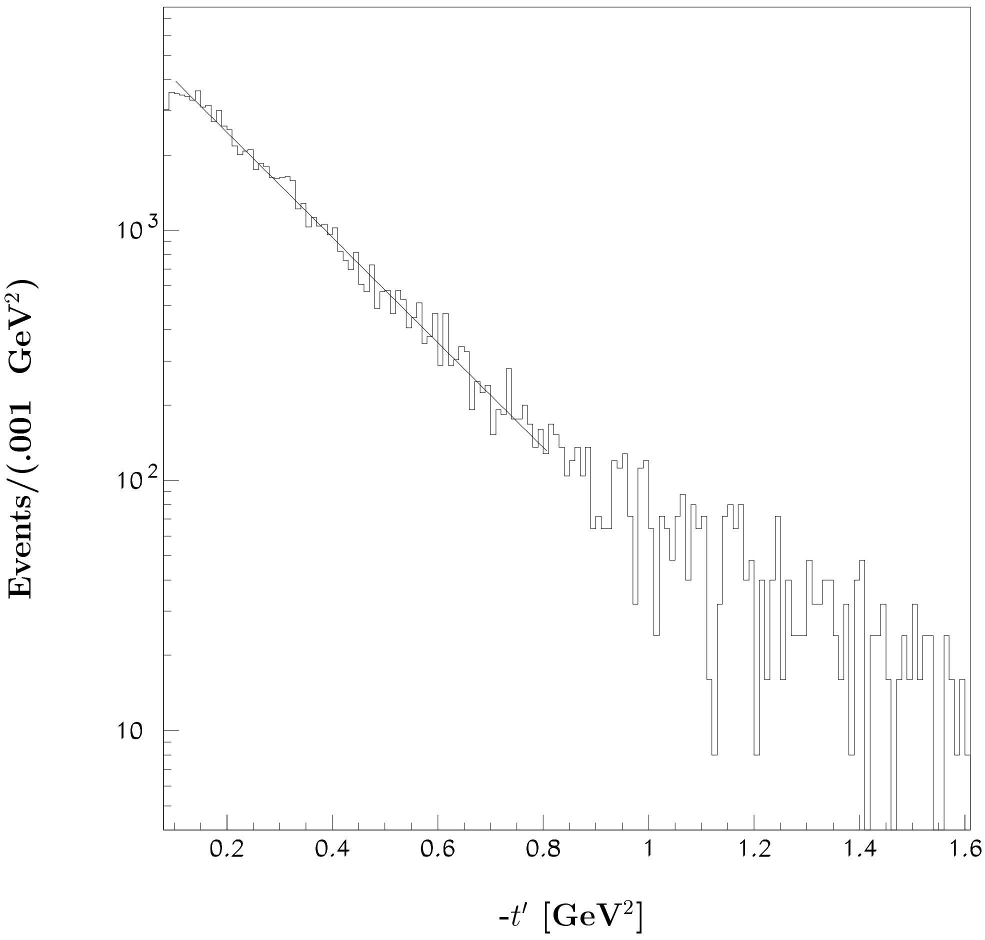

Figure 3.18: Acceptance corrected -t' distribution for the final p$\eta\pi^+\pi^-\pi^-$data sample.

TABLE 3.3
SUMMARY OF CUTS APPLIED TO THE TWO DATA SAMPLES

Selection Criteria	Primary Data Sample	Secondary Data Sample
Hadron rejection	20 cm	20 cm
DEA/CPVC Cut	Yes	Yes
# of charged tracks	3	3
# of untagged clusters	2	2
Vertex Cut	Inside target	Inside target
Beam reconstruction	Required	Required
Charge of tracks	-1	-1
SQUAW hypothesis	$\eta\pi^+\pi^-\pi^-p$	$\eta\pi^+\pi^-\pi^-p$
SQUAW Confidence level	>.1 (10%)	>.1 (10%)
$\lvert\Delta\phi\rvert$	<20°	<20°
$\eta\pi^+\pi^-$ mass ($f_1(1285)$ cut)	$1.23<M(\eta\pi^+\pi^-)<1.33$ (GeV/c^2)	$1.23<M(\eta\pi^+\pi^-)<1.33$ (GeV/c^2)
η' cut	M($\eta\pi^+\pi^-$)>1.02 GeV/c^2	M($\eta\pi^+\pi^-$)>1.02 GeV/c^2
Untagged CsI Energy	No Cut	<.020 GeV
Total Number of Events	12,559	6,478

CHAPTER 4

ANALYSIS

The complete analysis of an inclusive reaction such as $\pi^- p$ can be extremely difficult. A large number of states may be produced. These states may decay several different ways. For the data set under consideration, only the initial state ($\pi^- p$) and the final state ($\eta\pi^+\pi^-\pi^- p$) are known. The intermediate states are unknown and the possibilities are numerous. The determination of what actually occurred is a major undertaking.

4.1 Partial-Wave Analysis

Currently, the most comprehensive technique for this analysis is partial-wave analysis (PWA). It is based upon the superposition principle. The total data sample is determined by the combination of states which are produced and decay into the final state under study. In a PWA, the decay of each possible intermediate state is modelled. Fits are then accomplished to try to match the data. In this way it is possible to determine how much of each state was produced. This is the most simple of descriptions of partial-wave analysis.

The partial-wave analysis used in this work is based upon the Brookhaven PWA which was originally developed for BNL E771 [46, 47]. It was extended to include a four-body analysis by BNL E818 [19]. It has been further modified to include the additional states needed for this analysis. The notation used in describing the PWA follows as closely as possible that of S.U. Chung's *Formulas for Partial Wave Analysis* [48]. Further explanations of partial-wave analysis are available in numerous references [48, 49, 50, 51, 52]. Also, specifics of this particular PWA are given in Appendix A.

4.1.1 Isobar Model

In this analysis, the decay of unstable particles is described by the isobar model [53]. The state can decay to any of three combinations: two bachelor particles, a bachelor particle and an isobar, or two isobars. A bachelor particle is defined as any stable particle or any long-lived particle whose decay is irrelevant in the analysis. An example is $\eta \rightarrow \gamma\gamma$. The η is reconstructed prior to the PWA and constrained by SQUAW. In this analysis, the bachelor particles are the η, the π^+, and the two π^-'s. The isobars include $f_1(1285)$, $\eta(1295)$, $a_0(980)$, $\rho^0(770)$, $a_1(1260)$, and $a_2(1320)$.

There are two types of decay chains involved in this analysis. The primary decay chain is a series of decays to a bachelor particle and an isobar (figure 4.1(a)). Equation 1.1 is an example of this type of decay chain. The other type of decay chain involves an initial decay to two isobars (figure 4.1(b)). Both of these isobars then decay to two bachelor particles. The decay $X^- \rightarrow \rho^0(770) a_0^-(980)$ is an example of this type of decay chain. The double isobar decays are handled differently by the PWA. The descriptions used in this section will generally apply to the primary decay mode, while the handling of the double isobar decays is described in Appendix A.3.

The decay chains which were considered are listed in Tables 4.1 and 4.2. Each of these results in the final state $\eta\pi^+\pi^-\pi^-$. Note: in the tables σ refers to a

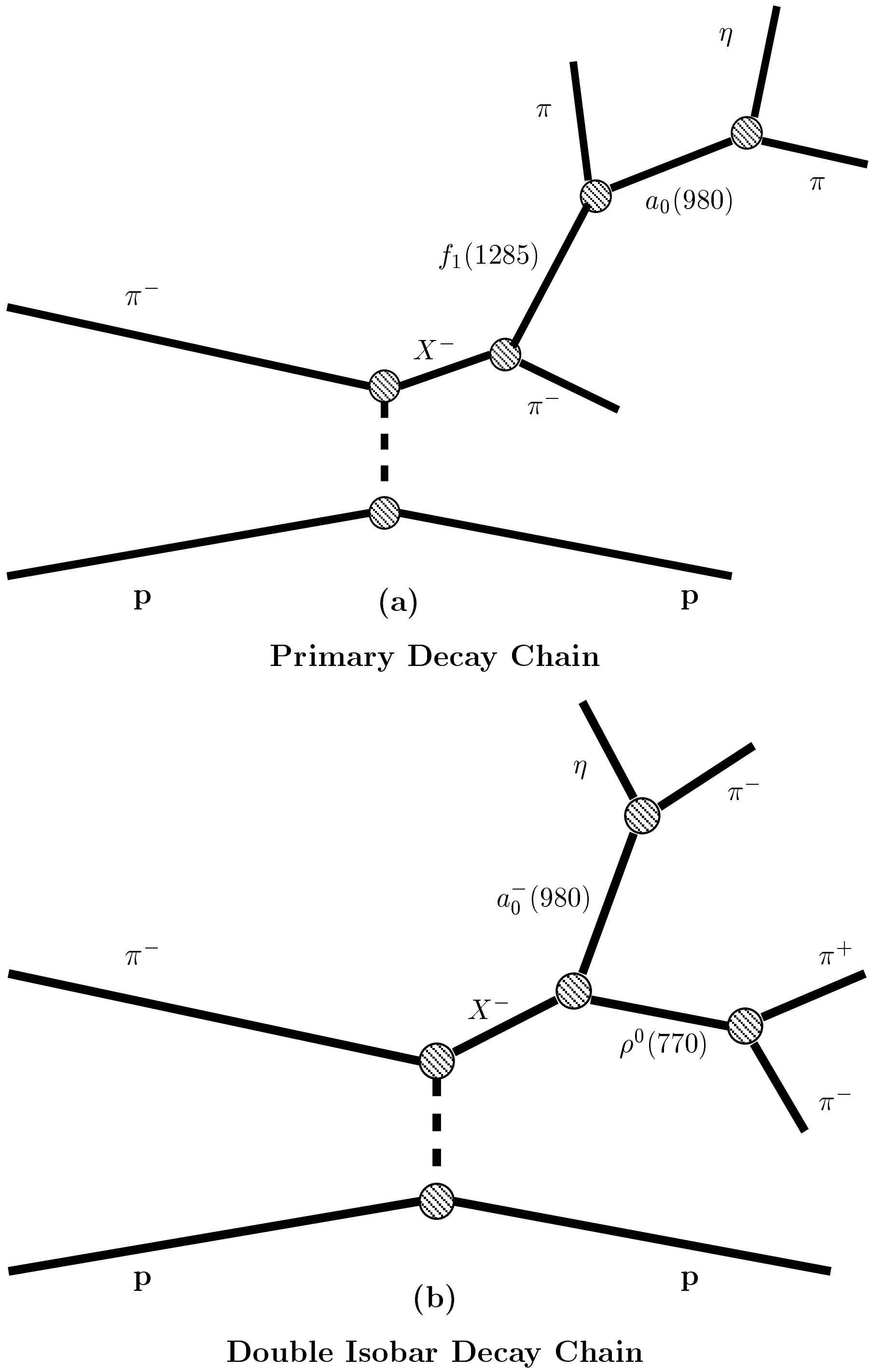

Figure 4.1: Feynman diagrams for examples of the two main types of decay chains in the $\eta\pi^+\pi^-\pi^-p$ analysis; (a) Primary decay chain; (b) Double isobar decay chain

TABLE 4.1
PRIMARY DECAY MODES FOR $\eta\pi^+\pi^-\pi^-$ STATE

Primary Decay	Secondary Decay	Tertiary Decay
$X^- \to f_1(1285)\pi^-$	$f_1(1285) \to a_0(980)\pi$ $f_1(1285) \to \sigma\eta$	$a_0(980) \to \eta\pi$ $\sigma \to \pi^+\pi^-$
$X^- \to \eta(1295)\pi^-$	$\eta(1295) \to a_0(980)\pi$ $\eta(1295) \to \sigma\eta$	$a_0(980) \to \eta\pi$ $\sigma \to \pi^+\pi^-$
$X^- \to a_2^-(1320)\eta$	$a_2^-(1320) \to \rho^0(770)\pi^-$	$\rho^0(770) \to \pi^+\pi^-$
$X^- \to a_1^-(1260)\eta$	$a_1^-(1260) \to \rho^0(770)\pi^-$	$\rho^0(770) \to \pi^+\pi^-$

TABLE 4.2
DOUBLE ISOBAR DECAY MODES FOR $\eta\pi^+\pi^-\pi^-$ STATE

Primary Decay	Secondary Decay A	Secondary Decay B
$X^- \to \rho^0(770)a_0^-(980)$	$\rho^0(770) \to \pi^+\pi^-$	$a_0^-(980) \to \eta\pi^-$
$X^- \to \rho^0(770)a_2^-(1320)$	$\rho^0(770) \to \pi^+\pi^-$	$a_2^-(1320) \to \eta\pi^-$
$X^- \to \sigma a_0^-(980)$	$\sigma \to \pi^+\pi^-$	$a_0^-(980) \to \eta\pi^-$
$X^- \to \sigma a_2^-(1320)$	$\sigma \to \pi^+\pi^-$	$a_2^-(1320) \to \eta\pi^-$

parametrization of the $\pi^+\pi^-$ S-wave state (see Appendix A.4). There are other decay chains which result in this final state. However, they are not used for various reasons. There are two primary reasons: (1) small or unconfirmed decay modes and (2) little evidence in the mass spectra. In general, decay chains will be simply referred to by the particles of the primary decay. Therefore, an $a_2^-(1320)\eta$ state assumes the $a_2^-(1320) \to \rho^0(770)\pi^-$ and $\rho^0(770) \to \pi^+\pi^-$ decays. This is possible because there is no ambiguity for these decays. The term *primary isobar* will refer to the isobar which decays in the secondary decay. The term *secondary isobar* will refer to the isobar which decays in the tertiary decay.

4.1.2 *Description of the $\eta\pi^+\pi^-\pi^-$ States*

The $\eta\pi^+\pi^-\pi^-$ data sample is a superposition of many different states. These states can be described by a limited number of parameters, including quantum numbers and isobars. The parameters for the primary decay mode are:

$$b = \{I^G J^{PC} \ell s \ell' \sigma \ell'' m \ (\omega_0 \omega_0')\} \tag{4.1}$$

where:

I : the isospin of the $\eta\pi^+\pi^-\pi^-$ system, I=1,

G : the G-parity of the $\eta\pi^+\pi^-\pi^-$ system, $G = -1$,

J : the spin of the $\eta\pi^+\pi^-\pi^-$ system,

P : the parity of the $\eta\pi^+\pi^-\pi^-$ system,

C : the charge conjugation of the $\eta\pi^+\pi^-\pi^0$ system, $C = G(-1)^I = +1$,

ℓ : the orbital angular momentum between the products of the primary decay,

s : the spin of the primary isobar,

ℓ' : the orbital angular momentum between the products of the secondary decay,

σ : the spin of the secondary isobar,

ℓ'' : the orbital angular momentum between the products of the tertiary decay, $l'' = \sigma$,

m : the absolute value of the z component of the spin of the $\eta\pi^+\pi^-\pi^-$ system,

ω_0 : the primary isobar mass, and

ω_0' : the secondary isobar mass.

Note: the number of parameters required is reduced by the fact that all bachelor particles in this analysis have spin 0.

One additional parameter is used to describe the state: ϵ, the reflectivity. This is due to a transformation of basis via the reflection operator [19, 48, 54] in the overall CM rest frame. The parity conservation of the strong interaction is thus taken into account. This is also the reason for m being solely positive. For m=1, ϵ=±1. For m=0, ϵ is given by

$$\epsilon = P(-1)^{J+1} \tag{4.2}$$

The reflectivity also defines the naturality of the exchanged particle in the production process. Positive reflectivity, $\epsilon = +1$, is natural parity exchange ($J^P = 0^+, 1^-, 2^+, ...$) with likely exchange particles $\rho^0(770)$, $f_0(980)$ or $f_2(1270)$. Negative reflectivity, $\epsilon = -1$, is unnatural parity exchange ($J^P = 0^-, 1^+, 2^-, ...$) with likely exchange particles η, $f_1(1285)$ or $b_1(1235)$.

4.1.3 Description of the $\eta\pi^+\pi^-\pi^-$ Data

The $\eta\pi^+\pi^-\pi^-$ data require a minimum set of variables to describe each event. Sixteen variables will fix the four-vectors of the four final-state particles. Conservation of momentum for the event applies four constraints. Four additional constraints come from the masses of the final-state particles. Therefore, 16-8 = 8 variables are needed to describe an $\eta\pi^+\pi^-\pi^-$ event. Two of these are chosen to be the intermediate isobar masses, ω and ω', of the secondary and tertiary decays. The remaining six are chosen to be the decay angles: $\Omega = (\Theta,\Phi)$, $\Omega_h = (\theta,\phi)$, and $\Omega_{h'} = (\theta', \phi')$.

These angles are measured in the rest frames of the decays. The first two (Ω) are the polar and azimuthal angles of the first isobar momentum ($\vec{p}$) in the Gottfried-Jackson (G-J) frame ($\eta\pi^+\pi^-\pi^-$ rest frame). The Gottfried-Jackson frame is oriented with $\hat{z}$ along the beam (in the $\eta\pi^+\pi^-\pi^-$rest frame) and $\hat{y}$ normal to the production plane ($\vec{beam} \times \vec{X}^-$ in the CM frame). The second two (Ω_h) are the polar and azimuthal angles of the second isobar momentum ($\vec{q}$) in the helicity frame (secondary decay rest frame). The helicity frame is oriented such that $\hat{z}_h = \hat{p}$ ($\hat{p} = \frac{\vec{p}}{|\vec{p}|}$) and $\hat{y}_h \propto \hat{z} \times \hat{p}$ where $\hat{z}$ is the z-axis in the G-J frame. The last two ($\Omega_{h'}$) are the polar and azimuthal angles of one of the products of the tertiary decay as measured in the second helicity frame (tertiary decay rest frame). The second helicity frame is oriented such that $\hat{z}_{h'} = \hat{q}$ ($\hat{q} = \frac{\vec{q}}{|\vec{q}|}$) and $\hat{y}_{h'} \propto \hat{z}_h \times \hat{q}$.

Two other variables are used in describing an event. These are M, the total $\eta\pi^+\pi^-\pi^-$ mass, and t, the total four-momentum transfer squared. For the PWA, the data are binned in M and t. Therefore, for a given M and t the events are described by the variables:

$$\tau = \{\omega, \omega', \Omega, \Omega_h, \Omega_{h'}\} \tag{4.3}$$

4.1.4 *Intensity Distribution*

The differential cross-section for the reaction,

$$\pi^- \; p \rightarrow \eta \; \pi^+ \; \pi^- \; \pi^- \; p \tag{4.4}$$

determines the intensity distribution, $I(\tau)$, and therefore the number of events in a given M and t bin. This intensity distribution is one of the major variables the PWA attempts to match. For the reaction (4.4), the intensity distribution can be written:

$$I(\tau) = \sum_{\epsilon b b'} {}^{\epsilon}\rho_{b,b'} \; {}^{\epsilon}\psi_b(\tau) \; {}^{\epsilon}\psi^*_{b'}(\tau) \tag{4.5}$$

where b is the set of quantum numbers defining each intermediate state (Eq. 4.1), ϵ is the reflectivity and ${}^{\epsilon}\psi_b(\tau)$ is a symmetrized decay amplitude which is described below. The spin density matrix, ${}^{\epsilon}\rho_{b,b'}$, is given by

$$
{}^{\epsilon}\rho_{b,b'} = \sum_{k=1}^{K} {}^{\epsilon}V_{bk}\, {}^{\epsilon}V^{*}_{b'k} \tag{4.6}
$$

where ${}^{\epsilon}V_{bk}$ are the "production amplitudes" and k allows for independent sets of interfering waves. In this analysis, $K = 2$ with the k=1 waves representing spin non-flip of the proton and the k=2 waves representing spin flip of the proton. The Chung and Trueman [54] parametrization of the spin density matrix is used. By defining another set of variables

$$
\alpha = \{\epsilon k b\} \tag{4.7}
$$

the intensity distribution can be written in a most useful form

$$
I(\tau) = \sum_{\alpha\alpha'} V_{\alpha}\, V^{*}_{\alpha'}\, \psi_{\alpha}(\tau)\, \psi^{*}_{\alpha'}(\tau) \tag{4.8}
$$

The unsymmetrized decay amplitudes, ${}^{\epsilon}A_b(\tau)$, (see Appendix A.2) are a method of parameterizing the likelihood that a given event (τ_i) is described by a given set of quantum numbers (b, ϵ). They are composed of several parts. Two Breit-Wigner functions and three Blatt-Weisskopf functions describe the mass and momentum dependence. The two Breit-Wigner functions give the mass dependence of the two intermediate isobars (i.e. $f_1(1285)$ and $a_0(980)$). The three Blatt-Weisskopf functions describe the momentum dependence of the three separate decays. The angular dependence is described by a set of orthonormal functions spanning the six angles of Eq. 4.3. These functions are based upon the spherical harmonics, $Y^L_M(\theta, \phi)$. The symmetrized decay amplitudes, $\psi_{\alpha}(\tau)$, take into account the interchange of the two π^-'s. The exact form of the decay amplitudes is discussed in detail in Appendix A.2.

The production amplitudes, V_α, are the goal of the partial-wave analysis. They essentially measure the amount of a given state which was produced in reaction 4.4. They are complex numbers which give the magnitude and relative phase of each state. One state for each rank is chosen as a reference wave and is purely real by definition. All phase measurements are therefore relative. If a resonant state with known parameters is available in the data it becomes possible to determine the resonant characteristics of other states by comparison.

4.1.5 *Monte Carlo*

The partial-wave analysis requires two sets of Monte Carlo (MC) events. Both of these sets are used to calculate normalization integrals which are used in the fitting process. The first set is a large number of pure phase-space generated four-body ($\eta\pi^+\pi^-\pi^-$) events. These events are used primarily for the calculation of the predicted (acceptance corrected) number of events. In this analysis, the generated Monte Carlo has the $f_1(1285)$ cut applied. This is done so that the predicted number of events corresponds to the $f_1(1285)$ region. The generated normalization integral is given by

$$\Psi_{\alpha\alpha'} = \frac{1}{M}\sum_{i=1}^{M} \psi_\alpha(\tau_i)\psi^*_{\alpha'}(\tau_i) \tag{4.9}$$

where M is the number of generated Monte Carlo events and $\psi_\alpha(\tau_i)$ is the symmetrized decay amplitude.

The second set is the accepted Monte Carlo. This is obtained by sending the generated Monte Carlo through a GEANT-based [55] simulation of the experiment. These events are then processed by a trigger simulator, the data reconstruction (Section 3.2), and the data selection cuts (Section 3.4). This gives a final set which simulates the observed data if it was produced by phase space. These events are used directly in the fitting process. The accepted normalization integral is given by

$$\Psi^x_{\alpha\alpha'} = \frac{1}{M_x}\sum_{i=1}^{M_x} \psi_\alpha(\tau_i)\psi^*_{\alpha'}(\tau_i) \tag{4.10}$$

where M_x is the number of accepted Monte Carlo events and $\psi_\alpha(\tau_i)$ is the symmetrized decay amplitude. One other quantity of importance is

$$\eta_x = \frac{M_x}{M} \tag{4.11}$$

which gives the Monte Carlo acceptance.

The stability of the normalization integrals is the determining factor in how many Monte Carlo events are needed. Studies were done of the $\Psi_{\alpha\alpha}$ normalization integrals. These were calculated with differing sets of N events (N=500, 1000, 2000, 5000, 10000). There were M_N sets of events for each N. M_N ranged from 25 to 100 with M_N decreasing as N increased. The distribution of $\Psi_{\alpha\alpha}$ for the M_N sets was plotted and measured. The variation in $\Psi_{\alpha\alpha}$ was defined to be $\Delta\Psi_{\alpha\alpha} = RMS/Mean$ for these distributions. As N increased, the variation $\Delta\Psi_{\alpha\alpha}$ decreased (figure 4.2). It was determined that at least 5000 Monte Carlo events per bin are needed for the normalization integral calculation. In practice, most of the bins had more (>10000) accepted Monte Carlo events. The average acceptance was 10%. Therefore, ten times as much generated Monte Carlo was available. In order to save time, the generated normalization integral was calculated with only 1/8 of the sample.

4.1.6 Likelihood Function

The major work of the PWA is done by a fitting program. This program determines the best values for the production amplitudes. The extended maximum likelihood method [56] is used. The extended maximum likelihood method gives a normal-

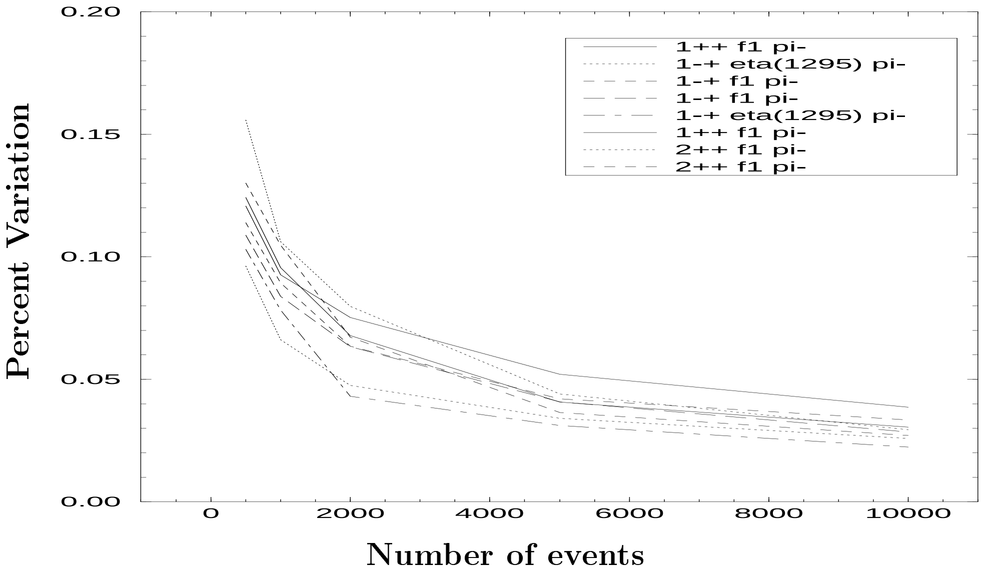

Figure 4.2: Variation in diagonal normalization integrals, $\Psi_{\alpha\alpha}$, as a function of number of Monte Carlo events.

ization for the calculation of predicted numbers of events. The likelihood function which was used can be written

$$\ln \mathcal{L} = \sum_{i=1}^{n} \ln[\sum_{\alpha\alpha'} V_\alpha V_{\alpha'}^* \psi_\alpha(\tau_i)\psi_{\alpha'}^*(\tau_i)] - n[\sum_{\alpha\alpha'} V_\alpha V_{\alpha'}^* \Psi_{\alpha\alpha'}^x] \tag{4.12}$$

where n is the number of data events in a given bin of M and t. The derivation of this function is available in several references [19, 48, 57]. For purposes of implementation the negative log likelihood was minimized using the CERN routine MINUIT [58]. The final result of this fit is a set of production amplitudes, V_α.

The predicted number of events N in a bin can then be calculated. The formula is

$$N = \frac{n}{\eta_x} \sum_{\alpha\alpha'} V_\alpha V_{\alpha'}^* \Psi_{\alpha\alpha'} \tag{4.13}$$

where η_x is the fraction of Monte Carlo events which were accepted in the bin. This is then plotted as the fit result.

4.1.7 Allowed Waves

Each intermediate state is defined by the combination of a decay chain and the set of quantum numbers b, ϵ. These states are also referred to as waves. The decay chains used in this analysis are listed in Tables 4.1 and 4.2. The quantum numbers are restricted by certain constraints. The allowed values for J are defined by the spins of the products of the primary decay and the orbital angular momentum between them, $\vec{J} = \vec{s_1} + \vec{s_2} + \vec{\ell}$. The parity, P, is given by $P = P_1 P_2 (-1)^{\ell}$. The charge conjugation and G-parity for the $\eta\pi^+\pi^-\pi^-$ state are +1 and -1, respectively. ℓ and m can be any non-negative value. ϵ is either +1 or -1. ℓ' and ℓ'' are determined by the isobars and their decay products.

For this analysis, additional restrictions have been placed on the waves. This is primarily to limit the number of waves involved. Extraneous waves may give the fit too many variables to find a proper solution. Certain decay chains (see Appendix A.1) have not been included. Some of the quantum numbers have been limited. While ℓ is unrestricted, J is limited to 3 or less. J>3 waves are not expected until higher mass regions. m is limited to 0 or 1. m>1 waves have not been seen in other analyses. These restrictions still give a large number (>200) of waves which may be included in the fit. The fitting process has difficulties handling more than 60 waves. Therefore, smaller sets of waves are used. The process of fitting and selecting waves is discussed below (Section 4.2). Table 4.3 gives a sample set of waves. The background term refers to an isotropic non-interfering background.

4.2 PWA Fits

The fitting process is the heart of the partial-wave analysis. Beyond understanding the calculation of decay amplitudes and normalization integrals, the fits are the real

TABLE 4.3
A SAMPLE SET OF WAVES USED FOR PWA

J	P	C	m	ϵ	Primary Decay Mode	ℓ	J	P	C	m	ϵ	Primary Decay Mode	ℓ
1	-	+	1	+	$f_1(1285)\pi^-$	S	2	-	+	0	+	$a_2^-(1320)\eta$	S
1	+	+	0	+	$f_1(1285)\pi^-$	P	1	+	+	1	-	$a_2^-(1320)\eta$	P
2	+	+	1	+	$f_1(1285)\pi^-$	P	1	+	+	0	+	$a_2^-(1320)\eta$	P
1	-	+	1	+	$f_1(1285)\pi^-$	D	1	+	+	1	+	$a_2^-(1320)\eta$	P
2	-	+	0	+	$f_1(1285)\pi^-$	D	1	-	+	1	+	$a_1^-(1260)\eta$	S
2	-	+	1	+	$f_1(1285)\pi^-$	D	0	+	+	0	-	$a_1^-(1260)\eta$	P
3	+	+	0	+	$f_1(1285)\pi^-$	F	1	-	+	1	-	$\rho^0(770)a_0^-(980)$	S
0	+	+	0	-	$\eta(1295)\pi^-$	S	0	+	+	0	-	$\rho^0(770)a_0^-(980)$	P
1	-	+	1	+	$\eta(1295)\pi^-$	P	1	+	+	0	+	$\rho^0(770)a_0^-(980)$	P
2	-	+	1	-	$a_2^-(1320)\eta$	S	background						

work. It is the process which determines the states that were produced. It is also the point at which the results must be interpreted and used to direct further work. Fitting is a very complicated process. For this analysis several hundred PWA fits have been done.

Data for the Fit

The data selection process was discussed in Chapter 3. Two primary sets of data have been used for the PWA. The primary data sample has a number of cuts (Section 3.4.5) applied. However, no cut on the energy deposited in the CsI was used. This set includes approximately 12,000 events. The other data set includes a CsI cut and has about 6,000 events. The breakdown of the number of events in each mass bin is given in Table 4.4. The events are binned in a single t bin ($0.1<-t<1.5$ GeV^2). It can be noted that some bins, particularly the high mass bins, have a fairly small number of events. The lack of overwhelming statistics has led to several

TABLE 4.4
THE NUMBER OF DATA EVENTS USED IN THE FIT

Mass bin (GeV)	Primary data sample	Tight Cut data sample	Mass bin (GeV)	Primary data sample	Tight Cut data sample
1.40-1.50	362	202	1.45-1.55	814	428
1.50-1.60	1220	620	1.55-1.65	1573	781
1.60-1.70	1863	931	1.65-1.75	2007	1038
1.70-1.80	1944	1025	1.75-1.85	1809	971
1.80-1.90	1780	958	1.85-1.95	1647	880
1.90-2.00	1373	724	1.95-2.05	1134	603
2.00-2.10	929	487	2.05-2.15	759	371
2.10-2.20	599	296	2.15-2.25	466	224
2.20-2.30	385	179	2.25-2.35	294	139
2.30-2.40	196	92	2.35-2.45	128	59
2.40-2.50	96	50	2.45-2.55	94	51
2.50-2.60	76	36	2.55-2.65	48	20

decisions. The bin size has been chosen to be fairly wide (100 MeV). This will limit the sensitivity to narrow states which may be present. The fits were occasionally done with the mass bins shifted by 50 MeV or with overlapping bins. This helps investigate structure which may be distorted by proximity to a bin edge. Only one t bin is used. This will not allow determination of differences in production processes.

The number of events needed for a proper partial-wave analysis depends upon several things. The number of variables which describe an event (τ) is a major factor. While a two-body analysis needs only 2 variables (θ_{GJ},ϕ_{TY}), the four-body analysis needs 8 ($\omega, \omega', \Theta, \Phi, \theta, \phi, \theta', \phi'$). This means more events are needed to describe the additional variables. Also, the four-body system probably has more intermediate states produced in the reaction. Additional events are needed to differentiate between the states. This, then, is related to the number of waves in the fit, so the larger the number of waves in the fit the greater the number of events required. The

PWA hypothesis plays a role also. If necessary waves are excluded or unnecessary waves included, more events may be needed to make the proper hypothesis more obvious.

Fit Parameters

Attempts were made to keep the number of waves in the fit to a minimum. The number of fit parameters can be easily calculated. Each production amplitude is a complex number (two parameters). However, one of the amplitudes for each reflectivity and rank is a reference wave and is chosen to be purely real. There is also an isotropic background term which is a single real number. Therefore, for a rank 1 fit with only one reflectivity the number of fit parameters is $N \times 2 - 1 + 1$ where N is the number of waves. A rank 2 fit has a different number of parameters. Each wave has two production amplitudes, one for each rank. Another wave is chosen as the rank 2 reference wave. The parameters of the fit result from a linear transformation of the production amplitudes [54]. This transformation guarantees the rank 1 reference wave has no parameters in the second rank. So the number of fit parameters for a rank 2 fit with only one reflectivity is $N \times 4 - 4 + 1$. A fit with only 23 positive reflectivity waves has 46 and 89 parameters for rank 1 and rank 2, respectively. Despite the dramatic increase in fit parameters, this analysis uses rank 2 fits. The reason for this is discussed below.

Fit Waves

The ideal way to do a partial-wave analysis would be to include all possible waves and let the fit determine which waves were important. This is not a practical approach in this analysis. It is, therefore, important that the right set of waves be used. Previous experimental and theoretical work was used as a starting point. The results of BNL 818 and VES were a guide. The waves of greatest interest (i.e.. J^{PC}=1^{-+}) were strongly considered. Intuition also played a role. An initial set of about 25 waves was selected.

From this initial set, trials were performed to determine the best set of waves. Single waves were added or subtracted from the fit. Each wave was evaluated for its significance. If the wave was important it was included in future fits. Most waves were reevaluated several times with various base sets of waves. The method of determining the significance of waves is discussed below.

An improved base set of about 30 waves was found by early tests. Large groups of waves (20-30) were then added to the fit. In this way, all waves (within the conditions discussed in Section 4.1.7) were tried at least once. Most of the waves were found to be consistent with zero and discarded. There were several which were later tried again as individual additions. A few were eventually added to the base set (e.g.. a 3^{++} $f_1(1285)\pi^-$ wave).

A special shorthand notation has been developed to identify a given wave. The notation is $J^{PC}m^{\epsilon}\ell$ *Primary decay*. This information uniquely identifies waves. An example is $1^{++}1^{+}$P $f_1(1285)\pi^-$. This is a J^{PC}=1^{++} $f_1(1285)\pi^-$ state decaying in a relative P wave. Also, m=1 and it is positive reflectivity. This notation will be used in the remainder of this work.

Fit Distributions

There are many distributions available to view the results of a given fit. The most important ones are the intensity distributions. These give the predicted number of events for a given wave or combination of waves. This information can be used to indicate the significance and relative magnitudes of the waves. These distributions can also be used to determine a cross-section; however that is not attempted here. Some sample distributions of predicted numbers of events are given in figure 4.3.

Another type of distribution available is the relative phase between two waves. The production amplitudes are complex numbers and therefore have a phase. This phase is relative to the reference wave and is not an absolute phase. Consequently, the phase difference between two waves is plotted. If a given state is resonant, its

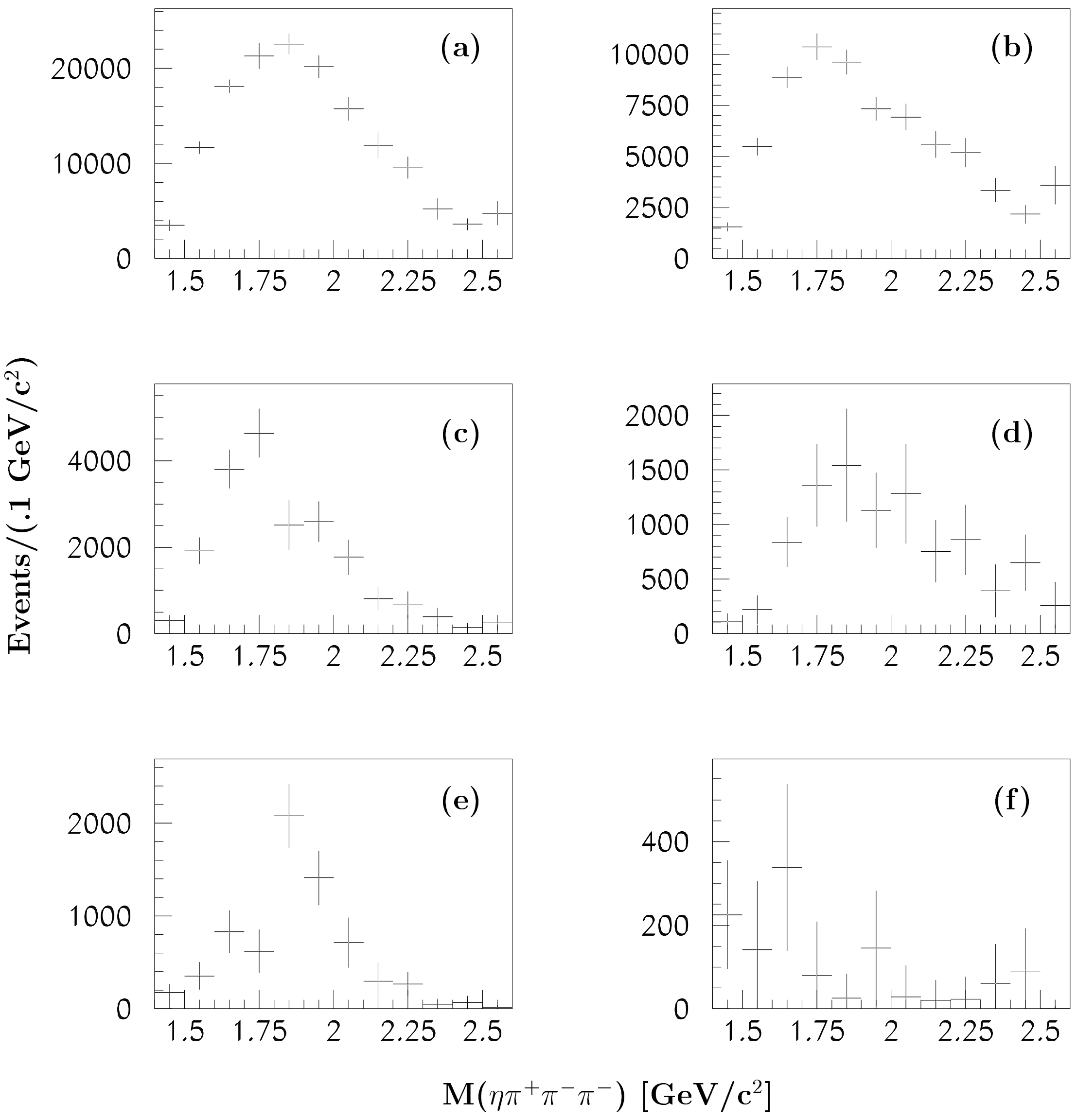

Figure 4.3: Sample distributions of predicted numbers of events (intensity) for an example fit. The plotted distributions are: (a) All waves + background; (b) $f_1(1285)\pi^-$waves; (c) $1^{++}0^+$P $f_1(1285)\pi^-$; (d) $2^{-+}0^+$D $f_1(1285)\pi^-$; (e) $1^{++}0^+$P $a_2^-(1320)\eta$; (f) $1^{++}1^-$P $\rho^0(770)a_0^-(980)$.

phase should undergo a change of π (180°) over the full width of the resonance. When plotted against a state with a constant or slowly varying phase, the phase difference will also undergo a change of π. If there is a known resonant state in the data sample it should be possible to determine the resonance properties of the other states by studying phase differences. However, there are no confirmed resonant $f_1(1285)\pi$ states. An important point to keep in mind is that for the relative phase difference $\pi = -\pi$ so the top and bottom of the plots wrap around.

Significance of Waves

Determining the significance of each wave is one of the most vital tasks of the analysis. Several criteria were used. One is the predicted number of events in that wave. Many waves had their predicted number of events within one standard deviation of 0. These waves were regarded as insignificant. The other important criterion was the change in the likelihood function. The significance of a given change in likelihood is dependent upon the change in number of parameters [59]. Adding or subtracting one wave from a rank 2 fit is a change of four parameters. For a change of four parameters, the wave is needed at the 95% confidence level if the log likelihood changes by about 5. Therefore, a change of five points or more is used as a guideline in determining the significance of a wave.

Many difficulties arise in the selection of waves. There is a constant struggle between trying to keep the number of fit parameters (i.e. waves) to a minimum and ensuring that necessary waves are included. A high level of significance (95%) is used because of the low statistics. If a given state exists within the data sample at the few percent level it will be difficult to discover it. This decision making process is complicated by the fact that for each mass bin the significance can vary. Generally the bins are considered together. However, if a wave is highly significant in only a few bins it is usually kept in all bins.

PWA Predictions

Several things were examined to determine the "goodness" of the fit. The goodness of fit is a measure of how well the fit matches the data. The accepted Monte Carlo events are assigned weights based upon their decay amplitudes and the production amplitudes from a fit. Weighted distributions of various event variables can be plotted. These distributions are then compared to corresponding distributions from the data.

An attempt was made to do a moments analysis similar to that used in the two-body analyses [39, 60, 61, 62]. Three angles were chosen. These were the two angles which describe the normal of the $\pi^+\pi^-\pi^-$ decay plane in its rest frame and the angle between the π^+ and the node (intersection of the decay plane and the x-y plane). These three angles were used the calculate various moments, $H(LMM')$. The moments for the data were compared to the predicted moments. The error bars on the moments for the data were large. The predicted moments were easily consistent with the data moments. However, it was not usually possible to conclude that one fit was better than another unless one of the fits was very bad. Bad fits were usually obviously wrong in other ways. For these reasons, the moments analysis was abandoned as a measure of goodness of fit.

Other distributions have been tried. The intermediate mass distributions ($\eta\pi$, $\pi^+\pi^-$, $\pi^+\pi^-\pi^-$) were compared (figure 4.4). The decay angle distributions were also compared (figure 4.5). These corresponded to the angles used in the calculation of decay amplitudes (Θ, Φ, θ, ϕ, θ', ϕ'). These distributions were an improved measure of the correctness of the fit. Some of the fits failed to match these distributions well. However, the sensitivity was still not good enough to differentiate between two fits which are similar.

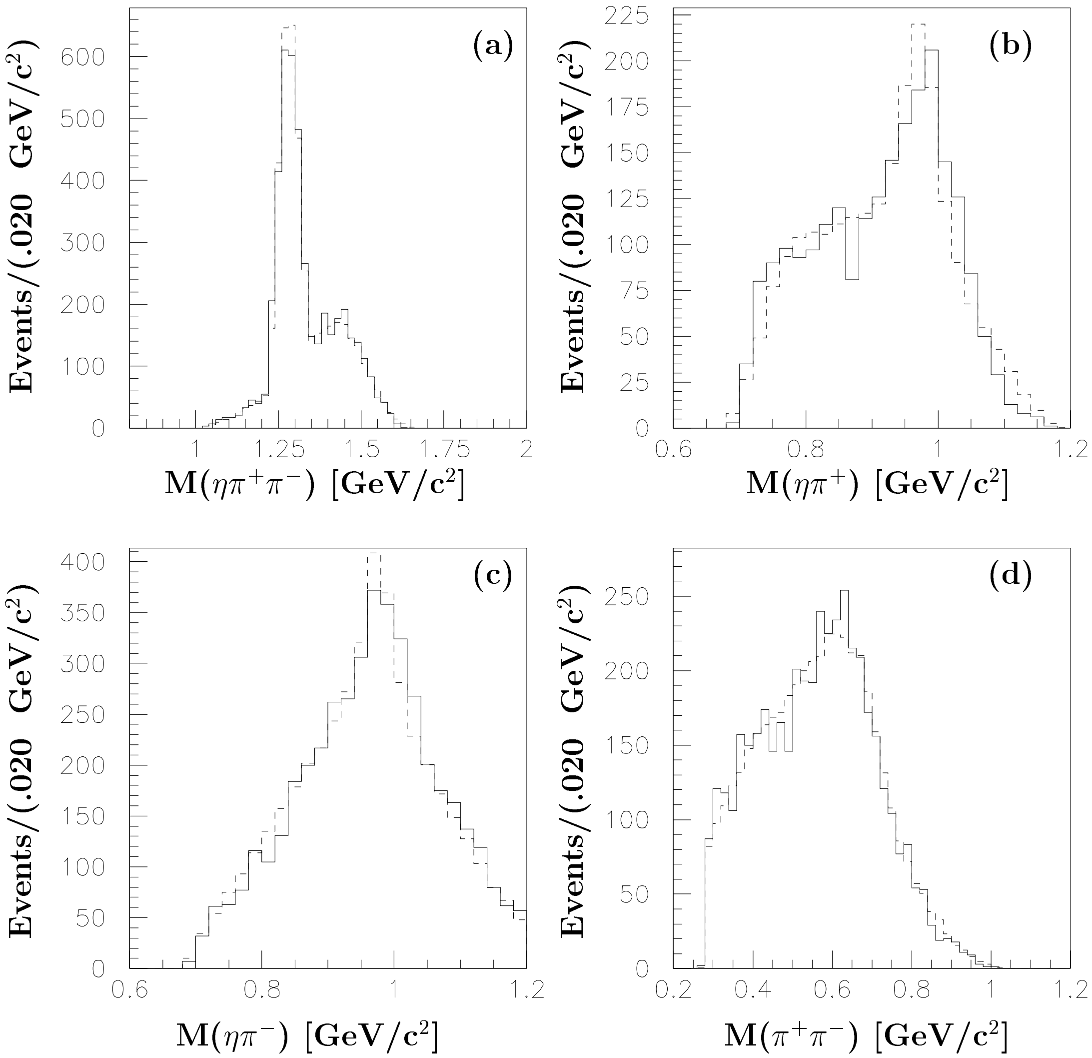

Figure 4.4: The intermediate mass distributions for the data (solid) and sample PWA predicted distributions (dashed). These distributions are for $1.70 < M(\eta\pi^+\pi^-\pi^-) < 1.80$ GeV/c^2. The figures show the (a) $\eta\pi^+\pi^-$, (b) $\eta\pi^+$, (c) $\eta\pi^-$and (d) $\pi^+\pi^-$ mass distributions.

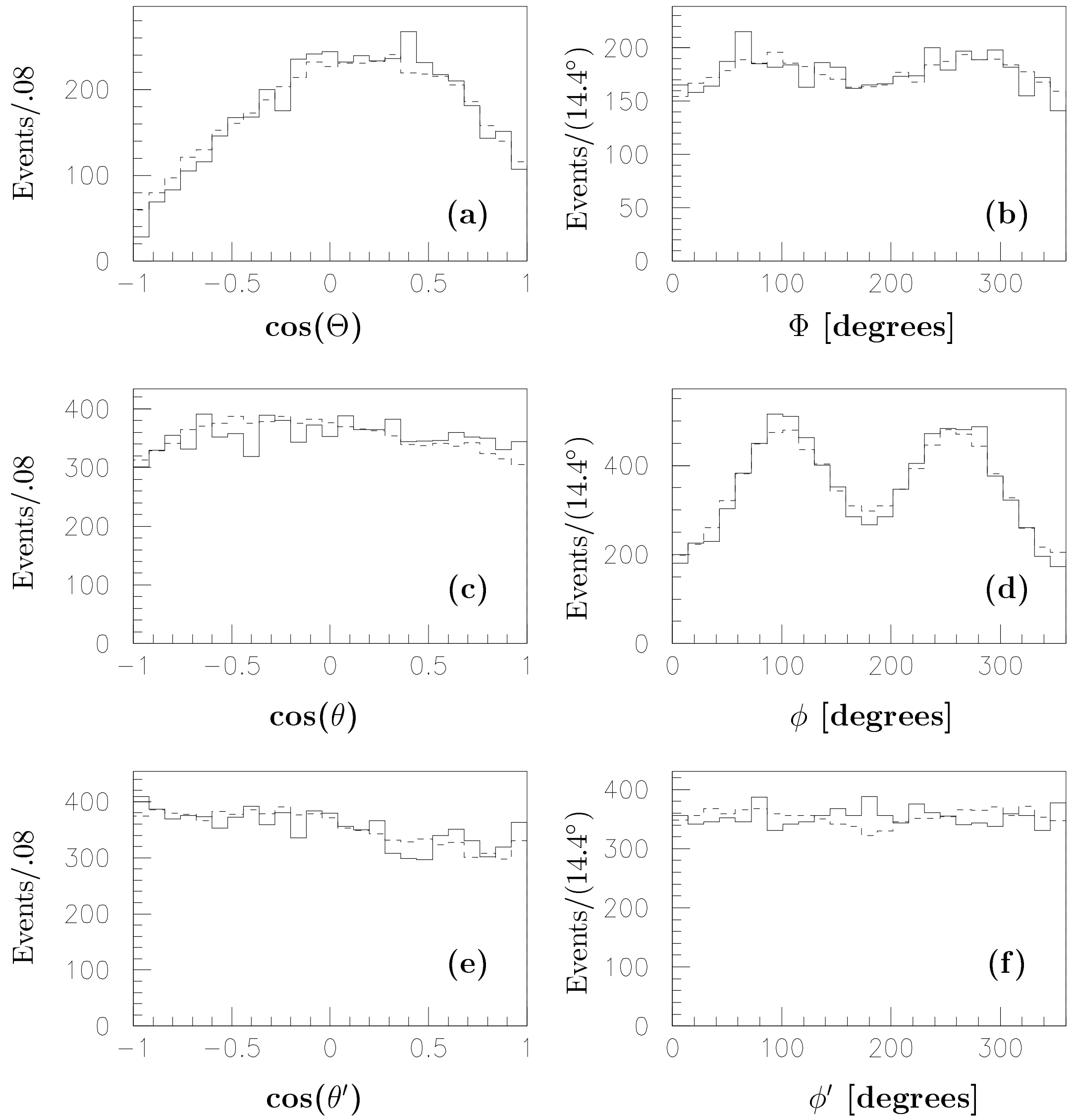

Figure 4.5: The angle distributions for the data (solid) and sample PWA predicted distributions (dashed). The plotted angles are (a) $\cos(\Theta)$, (b) Φ, (c) $\cos(\theta)$, (d) ϕ, (e) $\cos(\theta')$, and (f) ϕ'.

4.3 PWA Tests

Every analysis needs to be tested in various ways. It is necessary to check the validity of the result. There are assumptions on which the analysis is based. These assumptions must be investigated to determine whether they are reasonable. The result of a given analysis can be strengthened by probing its weaknesses.

There are a number of assumptions which are important in this partial-wave analysis. Some of them have been discussed earlier. The number of Monte Carlo events required was considered in Section 4.1.5. For the chosen bin size (100 MeV) there are more than enough generated and accepted Monte Carlo events. The restrictions on the allowed quantum numbers were described in Section 4.1.7. The choice to restrict $J \leq 3$ may become a problem for future analyses with more data in the higher mass regions. Many tests were performed to check the assumptions and interpretations of this analysis. Some of them are described below.

Stability of the Fits

The factors influencing the required amount of data were discussed in Section 4.2. It is clear that the high mass bins are statistics limited. However, it is difficult to put an exact value to the required number of events. There are some checks which may be run. The stability of the fit can be tested by running the fit multiple times with various starting points. In a fit without enough statistics, the fitting space may not be well defined and multiple solutions can exist as a result. Each bin was fit many times (>50) with random starting values for each fit parameter. Multiple solutions were found for every bin in the fit. For some of the bins, "bad" solutions were found in which the likelihood function was 10-60 points higher than for the nominal fit. These solutions were found infrequently and were obvious. They were therefore not important as long as the final fit was performed multiple times to identify any improper solutions.

All of the bins had several "good" solutions. Here, the variation in likelihood function was generally only a few points. In the lower mass bins (<1.9 GeV/c^2), these solutions gave the same result (within one standard deviation) for all waves. In two bins, two results were found in which some phase differences had similar magnitudes but opposite signs. A few other bins in the high mass region had solutions with greater variation. Some of the phase differences were so widely spread as to cover all possible values. There was no known way to determine the proper solution. These bins had low statistics. While multiple solutions were found for each bin, the results were generally consistent; interpretations will be limited in the regions where inconsistent solutions were found.

Negative Reflectivity Waves

The BNL 818 analysis [16, 19] found no significant waves with negative reflectivity. This was checked very early in the analysis and re-checked several different times. This analysis also found no significant contributions from negative reflectivity waves. The negative reflectivity waves were generally consistent with 0. The inclusion of negative reflectivity waves did not significantly change the final results for the positive reflectivity waves. This indicates that the production of the $\eta\pi^+\pi^-\pi^-$ events ($f_1(1285)/\eta(1295)\pi^-$and other states) involved mainly natural parity ($f_2(1270)$ or $\rho^0(770)$) exchange, rather than unnatural parity ($b_1(1235)$ or $f_1(1285)$) exchange.

Fit Rank

The need for inclusion of a second rank in the fit was tested several times. While most of the individual second rank wave contributions were small, the total contribution from the second rank waves was about one-quarter of the total signal. The removal of the second rank caused an increase in the -log likelihood of more than 50 points for several of the bins. For the change in parameters from 89 to 46, this indicates the need for the second rank at well over the 99.5% confidence level. The inclusion of the second rank also helps avoid the possibility of false signals being created in the first rank. All of these results led to the conclusion that the second rank is necessary in the fit.

Variation in Event Sample

The sensitivity of the final results to the variation in the event sample was studied. The selection of cuts which are applied to the data can be somewhat arbitrary. An example is the $\Delta\phi$ cut (Section 3.4.2) which was chosen to be $\Delta\phi<20°$. There are a range of cut values which are probably just as valid. A complete partial-wave analysis was performed on a data sample with a tighter $\Delta\phi$ cut ($|\Delta\phi|<12°$). The PWA results were found to be insensitive to the exact $\Delta\phi$ cut. Due to the amount of work necessary to carry a partial-wave analysis to completion most of the cuts were determined by their effect on distributions rather than on the final PWA result.

However, there were two data sets used in this analysis. The primary set has the standard cuts, while the second set has an additional cut on the untagged energy deposited in the CsI (Table 3.3). The purpose of the CsI was vetoing events with non-proton recoils. The cut on the energy deposited in the CsI (untagged energy<.020 GeV) reduces the data sample by half which further decreases the statistics. It was decided to use both data samples and compare the final results to determine if the cut was necessary. The final PWA results were consistent for the two samples. Results for the primary sample are therefore presented in this work because of the greater statistics.

Large and Small Sets of Waves

The number of waves included in the fits varied dramatically. A “super” fit was attempted which included a large subset of the possible waves. This failed because a limitation in the current software restricts the number of waves in the plotting package to 64 or less. Many fits with approximately 60 waves were tried in searching for important waves which may have been missed. Several other fits were done with large sets of waves. They included the 60 (or so) most significant waves. However, the inclusion of many of these waves did not significantly improve the fit. Fits with 60 waves had the major disadvantage of having over 200 parameters.

Attempts were made to do a fit with only a few waves. The included waves were limited to the most significant. This was to test whether the data could be well described with only a few states. The results showed that the included waves had predicted numbers of events with shapes similar to those for fits with the nominal wave set. However, there were significant differences particularly in the magnitude of predicted number of events. The likelihood function definitely indicated the fit was not as good with the small sets. Also, the predicted distributions (Section 4.2) were not in good agreement with the data. It was determined that the fit needed more than a few waves to model the data properly.

Isobar parametrizations

The decay amplitudes contain terms which describe the mass dependence of the intermediate isobars. The various parametrizations which have been used are described in Appendix A.4. Most isobars were described with a Breit-Wigner form (Eq. A.27). Initially the PDG widths [18] were used in the calculation. However some of the widths were later changed to better match the observed widths. For example, the PDG width for the $f_1(1285)$ is .024 GeV/c^2. For Monte Carlo events generated with Γ=.024 GeV/c^2 and processed by the experimental GEANT simulation, the observed width was closer to .048 GeV/c^2. The $\eta\pi^+\pi^-$ peak in the 1.28 GeV/c^2 region for the data (which is presumably both $f_1(1285)$ and $\eta(1295)$) has a width of .056 GeV/c^2. The results of the PWA were not highly sensitive to the choice of Breit-Wigner widths for the intermediate isobars.

For two of the isobars, $a_0(980)$ and σ, there is some controversy about the proper parametrization. The $a_0(980)$ (in the $\eta\pi$ decay mode) can be treated either as a single Breit-Wigner or via a coupled-channel (CC) approach. The coupled-channel parametrization takes into account the $a_0(980)$ proximity to the $K\bar{K}$ threshold [63]. Three parametrizations were tried for the $a_0(980)$: PDG Breit-Wigner (Γ = .057 GeV/c^2), observed Breit-Wigner (Γ = .071 GeV/c^2) and coupled-channel formulation. The PWA results were insensitive to the differences in these $a_0(980)$ parametrizations. Two different parametrizations were used for the $\pi^+\pi^-$ S-wave, σ. These were the Au, Morgan, and Pennington (AMP) [64] and Crystal Barrel (CB) [65] parametrizations. See Appendix A.4 for explanations. Once again, the PWA results did not depend significantly upon the description of the σ. It has been shown that the results of this partial-wave analysis were essentially independent of these parametrizations. For the final fits, the PDG Breit-Wigners were used for all isobars except the σ (AMP), $a_0(980)$ (CC), $f_1(1285)$ (Γ=.048 GeV/c^2), and $\eta(1295)$ (Γ=.080 GeV/c^2).

$f_1(1285)$ Decay

For the majority of this analysis the $f_1(1285)\pi^-$ waves have been included in pairs. For each $J^{PC}m^{\epsilon}\ell$ $f_1(1285)\pi^-$ state a separate wave was given for each of the two $f_1(1285)$ decay modes, $a_0(980)\pi$ and $\sigma\eta$. The Particle Data Group [18] lists two decays modes for $f_1(1285) \to \eta\pi^+\pi^-$. The primary mode is through $a_0(980)\pi$. It also lists a direct three body decay mode. The direct three body decay mode is parametrized as $\sigma\eta$.

There is some uncertainty about the branching ratios for these decays. The PDG fit gives the $f_1(1285) \to a_0(980)\pi$ as 82$\pm$12% of the $\eta\pi^+\pi^-$ decays. The experiments which are used in this determination find values from 60% [40] to 100% [66]. The $f_1(1285) \to \eta\pi^+\pi^-$ decay has been studied in the E852 data sample [44]. However, the analysis of $\eta\pi^+\pi^-$ found the peak in the 1.28 GeV/c^2 region to be primarily $\eta(1295)$. The results for the decay of the $f_1(1285)$ allow for decays to $a_0(980)\pi$ 70-100% of the time.

Because of the uncertainty in the $\eta\pi^+\pi^-$ decay modes of the $f_1(1285)$, no constraint was initially applied to require the pairs of $f_1(1285)$ waves to have a given ratio. The PWA fit was allowed to determine the relative intensities and phases of the two decay modes independently. Fits were attempted with only the $a_0(980)\pi$ decays, but the change in likelihood indicated the fit needed both decay modes. Therefore, these waves were added or subtracted from the fit in pairs. Studies of the phase between waves of a pair indicated a fairly constant phase difference of about 2-3 radians. The relative intensities were also fairly constant with the $\sigma\eta$ decay mode being approximately 20-40% of the $a_0(980)\pi$ decay mode. This indicated the fit was handling the separate waves in a manner not inconsistent with previous studies of $f_1(1285)$ decays. The intensity distributions for the $f_1(1285)\pi^-$ waves are presented with both decay modes added together coherently. The relative phase difference distributions use the wave for the $a_0(980)\pi$ decay mode since it was the dominant mode.

A study was performed to determine whether a method could be found to constrain the two decay modes into a single wave. Physically, a single J^{PC} $f_1(1285)\pi^-$ state is produced which decays two different ways. One manner of parametrizing the $f_1(1285)$ decay is the coherent addition of the two decay modes. A new $f_1(1285)\pi^-$ decay amplitude was calculated

$$\psi_\alpha(\tau) = \psi_{\alpha_1}(\tau) + CN \times \psi_{\alpha_2}(\tau) \tag{4.14}$$

where ψ_{α_1} is the decay amplitude for the $f_1(1285) \rightarrow a_0(980)\pi$ wave, ψ_{α_2} is the decay amplitude for the $f_1(1285) \rightarrow \sigma\eta$ wave and CN is a complex number which gives the phase (ϕ) and relative intensity (r) between the two waves. Numerous PWA fits were done varying r and ϕ. The likelihood functions was evaluated in several mass bins until the best values for r (r=.34) and ϕ (ϕ=2.5 radians) were determined. The intensity and relative phase difference distributions for the PWA fit with these values were consistent with the distributions from the final fit when the waves are included independently. This helps verify the consistency of the two treatments of the $f_1(1285)$ decay. It also indicates that the decay modes of the $f_1(1285)$ may be studied in the $\eta\pi^+\pi^-\pi^-$ data.

Concurrent Analysis

The $\eta\pi^+\pi^-\pi^-p$ system in the 1994 E852 data has been concurrently studied by D. Ryabchikov [67]. A complete partial-wave analysis was performed using the VES PWA system. This helped to check that the results are not highly dependent upon the details of the PWA technique. Also, the concurrent analysis was performed with and without the $f_1(1285)$ cut. It was shown the results for the $f_1(1285)/\eta(1295)\pi^-$ waves were not affected by this cut. However, the results for the non-$f_1(1285)/\eta(1295)\pi^-$ waves were affected. The concurrent analysis greatly strengthened this analysis by suggesting important waves and additional areas of investigation. The basic conclusions of both analyses are in agreement.

CHAPTER 5

RESULTS

The ultimate goal of a partial-wave analysis is the determination of the intermediate states within the reaction. The work described up to this point has been done to determine the final PWA fit. The best set of waves has been found. The need to use rank 2 has been shown. The lack of negative reflectivity waves in the sample was demonstrated. The set of waves used in the final fit is listed in Table 5.1.

Once the final fit is found, the results must be plotted and interpreted. The remaining sections are devoted to presenting and interpreting the final results. The intensity distributions are given first. These determine the relative intensity of the waves. Some of the relative phase differences are then presented. A major advantage of a partial-wave analysis is the determination of the production amplitude phases. This is significantly more information than is available from a traditional mass analysis. The combination may allow the determination of the resonant properties of the states. A mass dependent analysis is presented. Finally, the results are interpreted.

TABLE 5.1
THE SET OF WAVES USED FOR THE FINAL PWA FIT

J	P	C	m	ϵ	Primary Decay Mode	ℓ
1	-	+	1	+	$f_1(1285)\pi^-$	S
1	+	+	0	+	$f_1(1285)\pi^-$	P
2	+	+	1	+	$f_1(1285)\pi^-$	P
1	-	+	1	+	$f_1(1285)\pi^-$	D
2	-	+	0	+	$f_1(1285)\pi^-$	D
2	-	+	1	+	$f_1(1285)\pi^-$	D
3	+	+	0	+	$f_1(1285)\pi^-$	F
1	-	+	1	+	$\eta(1295)\pi^-$	P

J	P	C	m	ϵ	Primary Decay Mode	ℓ
2	-	+	0	+	$a_2^-(1320)\eta$	S
2	-	+	1	+	$a_2^-(1320)\eta$	S
1	+	+	0	+	$a_2^-(1320)\eta$	P
1	-	+	1	+	$a_1(1260)\eta$	S
1	-	+	1	+	$\rho^0(770)a_0^-(980)$	S
1	+	+	0	+	$\rho^0(770)a_0^-(980)$	P
2	+	+	1	+	$\rho^0(770)a_0^-(980)$	P
background						

5.1 *Intensity Distributions*

There are a fairly large number of combinations of wave intensities which may be plotted for the final fit. Figure 5.1 shows the sum of all waves plus background, the background, the sum of all $f_1(1285)/\eta(1295)\pi^-$ waves and the sum of all non-$f_1(1285)/\eta(1295)\pi^-$ waves. The ratio of all waves to background is consistent with the ratio of signal to background for the η (Section 3.3.1). The $f_1(1285)/\eta(1295)\pi^-$ waves are approximately 40% of the data as is expected from the $\eta\pi^+\pi^-$ distribution (Section 4.2).

The intensity distributions for the individual $f_1(1285)/\eta(1295)\pi^-$ waves are shown in figure 5.2. The $1^{++}0^+P$ $f_1(1285)\pi^-$ wave is the dominant wave in the fit. However, the $1^{-+}1^+S$ $f_1(1285)\pi^-$ wave is fairly significant. The $1^{++}0^+$P, $1^{-+}1^+$S, and $2^{-+}0^+$D $f_1(1285)\pi^-$ waves will be examined in more detail below. The $1^{-+}1^+$P $\eta(1295)\pi^-$ wave is not very significant, shows no structure of interest and is unnecessary as determined from the likelihood function. However, it is included for

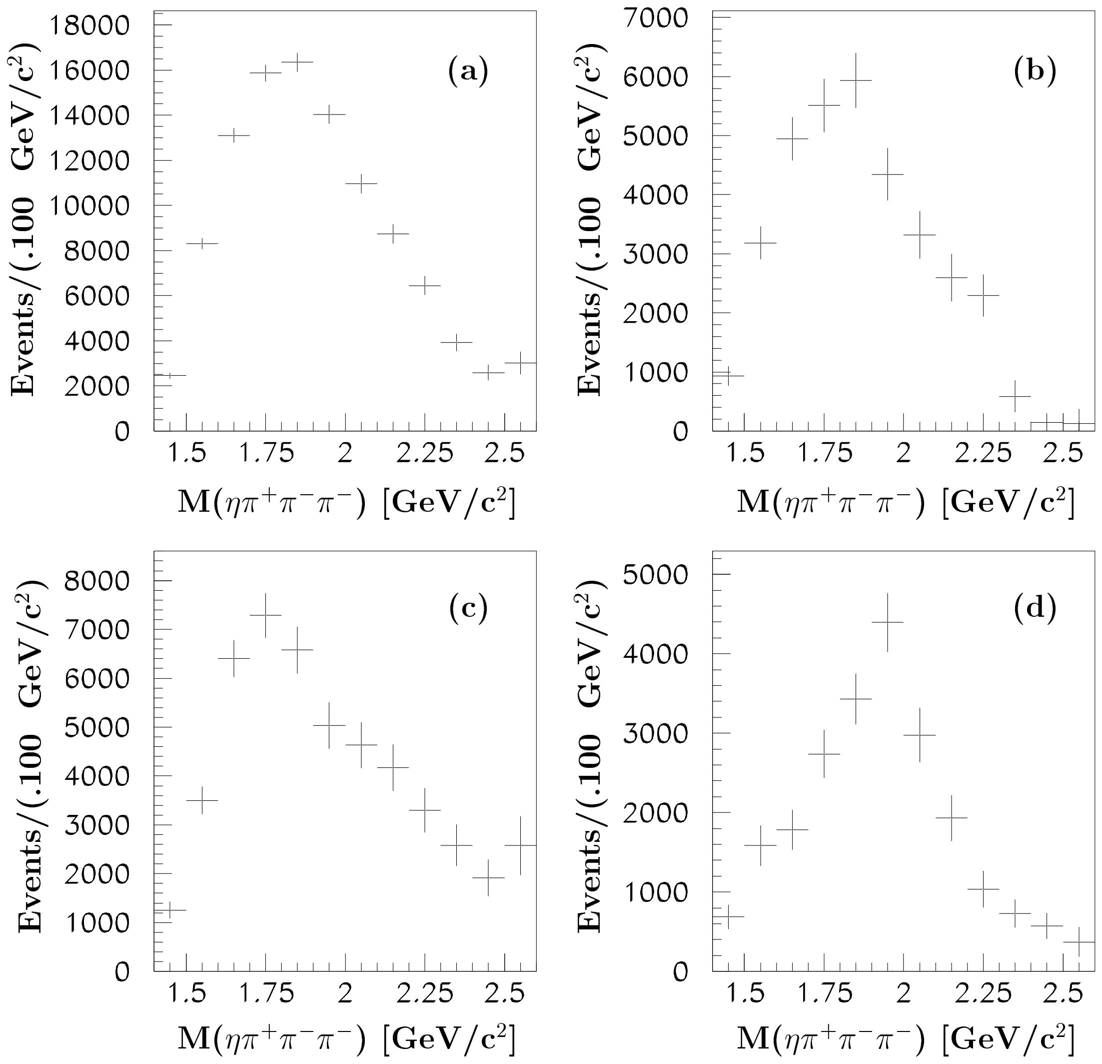

Figure 5.1: Intensity distributions for the final PWA fit. The figures are (a) all waves + background; (b) background; (c) all $f_1(1285)\pi^-$ waves; (d) all non-$f_1(1285)\pi^-$ waves.

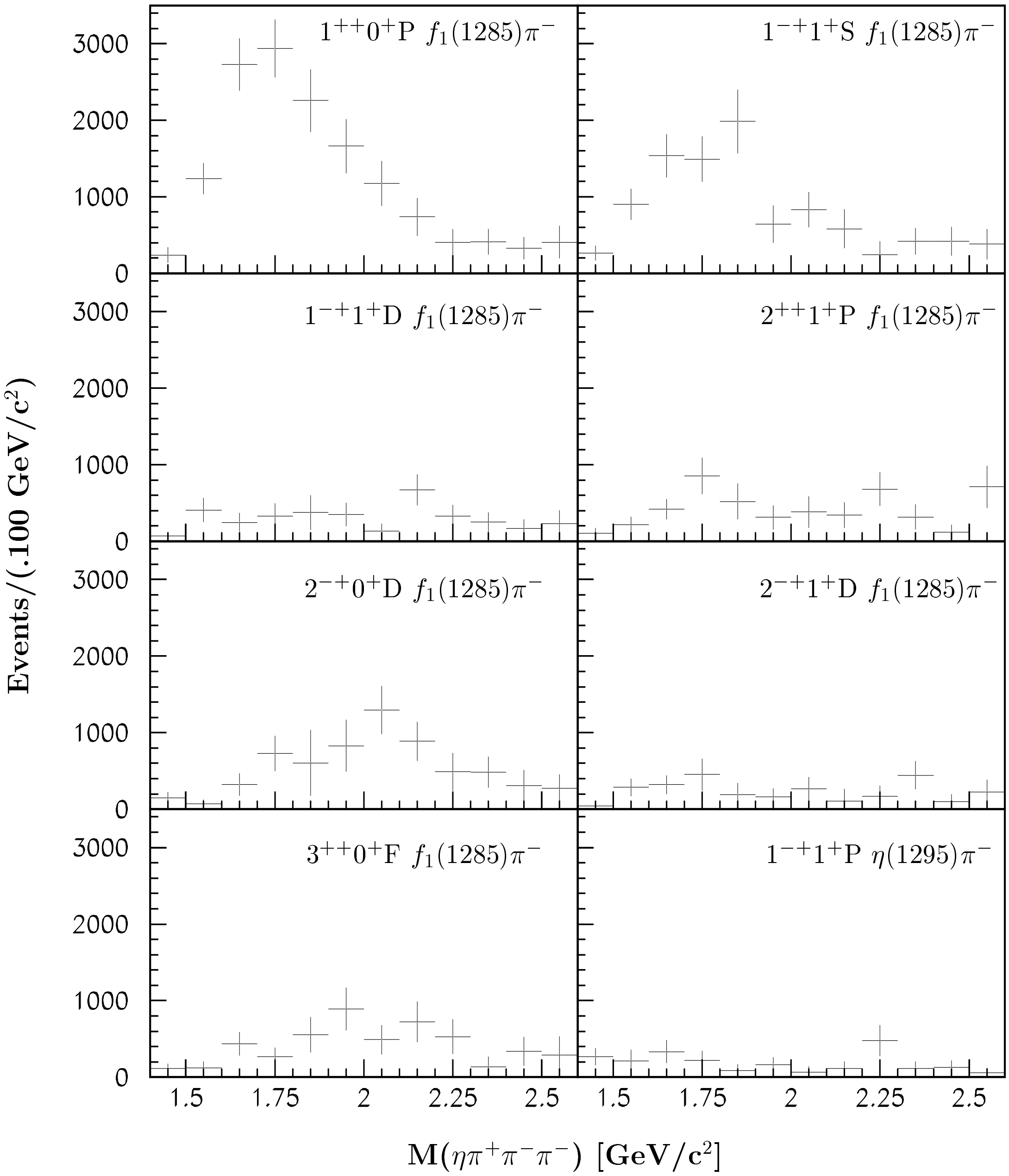

Figure 5.2: $f_1(1285)/\eta(1295)\pi^-$ intensity distributions for the waves in the final fit. The waves are listed on the plots.

comparison with BNL 818 [16, 19] which found evidence for it in their data.

The intensity distributions for the individual non-$f_1(1285)/\eta(1295)\pi^-$ waves are given in figure 5.3. The $f_1(1285)$ cut (1.23<M($\eta\pi^+\pi^-$)<1.33 GeV/c^2) may have distorted these distributions, so conclusions must be limited. There is a fairly strong $1^{-+}1^+$P $\rho^0(770)a_0^-(980)$ wave which is a possible exotic. The $2^{-+}0^+$S $a_2^-(1320)\eta$ wave has some interesting possibilities. The structure may indicate a fairly narrow ($\Gamma\leq$100 MeV) state around 1.9 GeV/c^2. However, the enhancement occures at threshold. The $2^{-+}0^+$S quantum numbers are the same as the $2^{-+}0^+D$ $f_1(1285)\pi^-$ wave. This could mean two decay modes of the same state. These possible states should be considered in future analyses.

Three $f_1(1285)\pi^-$ waves have been found to be of particular interest. These are the $1^{++}0^+$P, $1^{-+}1^+$S, and $2^{-+}0^+$D $f_1(1285)\pi^-$ waves. They are the strongest $f_1(1285)\pi^-$ waves and have interesting properties. The relative phases of these waves will be shown in the next section. These waves are plotted with expanded scales in figure 5.4. The $1^{++}0^+$P and $2^{-+}0^+$D waves have quantum numbers which are allowed for traditional $q\bar{q}$ mesons. These could be new states or new decay modes of previously observed states. The $1^{-+}1^+S$ $f_1(1285)\pi^-$ wave has exotic quantum numbers and may indicate a hybrid meson. The change in likelihood when this wave is removed gives a confidence level of greater than 99.99% that this wave is necessary to the fit. This is strong evidence for the necessity of an exotic wave in the $\eta\pi^+\pi^-\pi^-p$ data sample. All three waves will be the focus of a mass dependent analysis presented below.

5.2 Phase Information

The phase difference between waves can be a valuable tool for determining the resonant properties of the waves. The phase of a Breit-Wigner resonance goes through

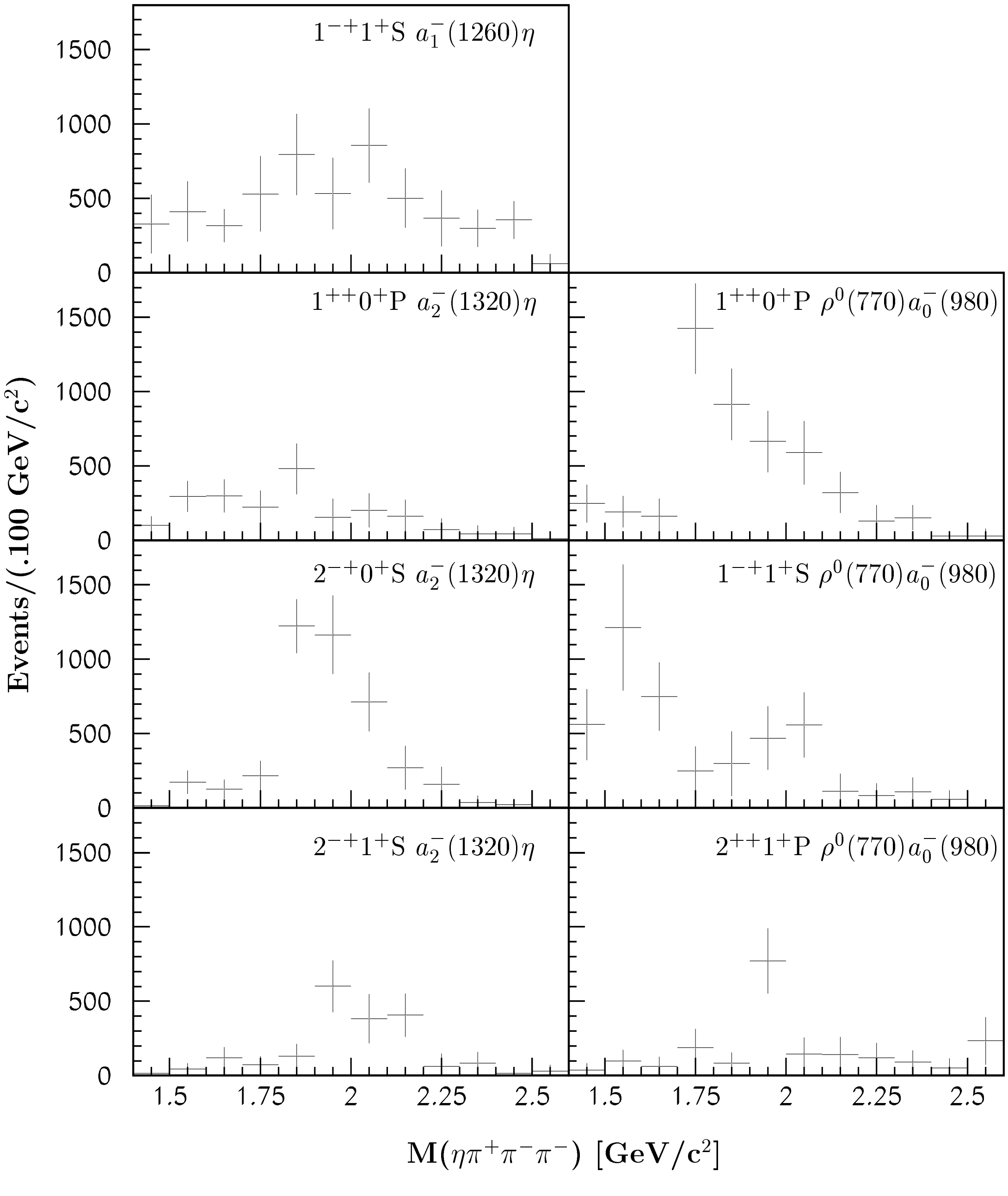

Figure 5.3: Non-$f_1(1285)\pi^-$intensity distributions for the waves in the final fit. The waves are listed on the plots.

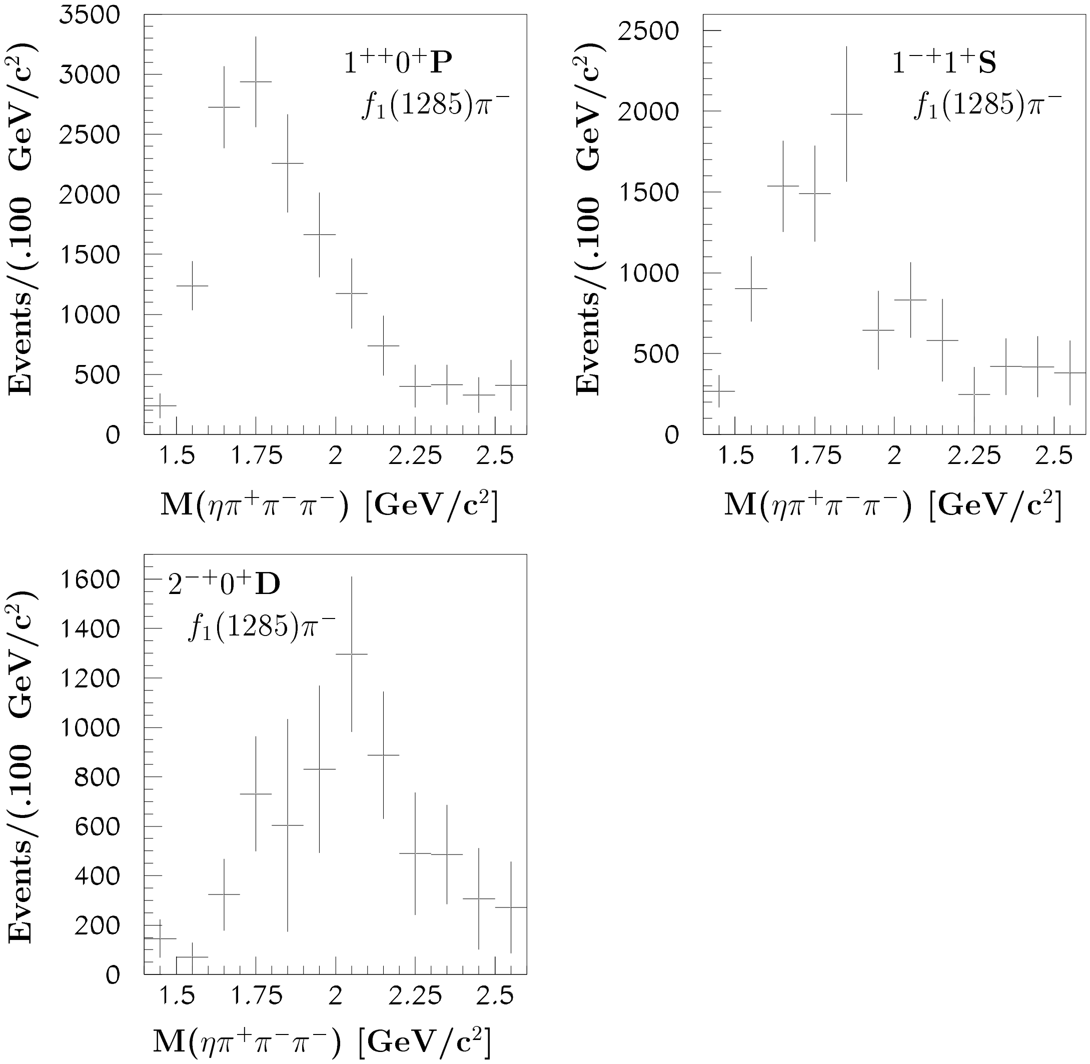

Figure 5.4: Intensity distributions for the three strongest $f_1(1285)\pi^-$ waves in the final fit.

a change of π when measured against a constant or slowly changing phase. The phase differences between the important $f_1(1285)\pi^-$ waves ($1^{++}0^+P$ $f_1(1285)\pi^-$, $1^{-+}1^+S$ $f_1(1285)\pi^-$ and $2^{-+}0^+D$ $f_1(1285)\pi^-$) are shown in figure 5.5. The phase difference between the $1^{++}0^+P$ $f_1(1285)\pi^-$ and the $2^{-+}0^+$S $a_2^-(1320)\eta$ waves is also included. Some of these phase differences have several "good" solutions which allow a sign flip. This is particularly true of the 1.8-1.9 and 2.0-2.1 GeV/c^2 bins. The bins above 2.4 GeV/c^2 have large enough error bars that the different solutions will cover all possible values.

The phase motion between the $f_1(1285)\pi^-$ waves is indicative of possible interesting physics. The small variation between the $1^{++}0^+P$ $f_1(1285)\pi^-$ and $1^{-+}1^+S$ $f_1(1285)\pi^-$ phases in the 1.5-2.2 GeV/c^2 region (figure 5.5(a)) may be caused by two resonances which have slightly different widths. The strongly falling phase of the $2^{-+}0^+D$ $f_1(1285)\pi^-$ phase (below 2.3 GeV/c^2) measured against both the $1^{++}0^+P$ $f_1(1285)\pi^-$ (figure 5.5(b)) and $1^{-+}1^+S$ $f_1(1285)\pi^-$ (figure 5.5(c)) phases could indicate resonances in the $2^{-+}0^+D$ $f_1(1285)\pi^-$ wave or in both the $1^{++}0^+P$ $f_1(1285)\pi^-$ and $1^{-+}1^+S$ $f_1(1285)\pi^-$ waves. It is possible that all three states are resonant or that some of the states are non-resonant. A mass dependent analysis has been performed in an attempt to differentiate among the possibilities.

5.3 Mass Dependent Analysis

A mass dependent analysis (MDA) has been performed on several waves from the final fit. Traditionally, a mass dependent analysis is an attempt to describe an intensity distribution (mass spectra) by a Breit-Wigner form. Here the analysis is a bit more complicated. Several intensity distributions and the relative phase differences between them will be fit together. This is an attempt to determine the resonant or non-resonant qualities of some of the waves in the PWA analysis.

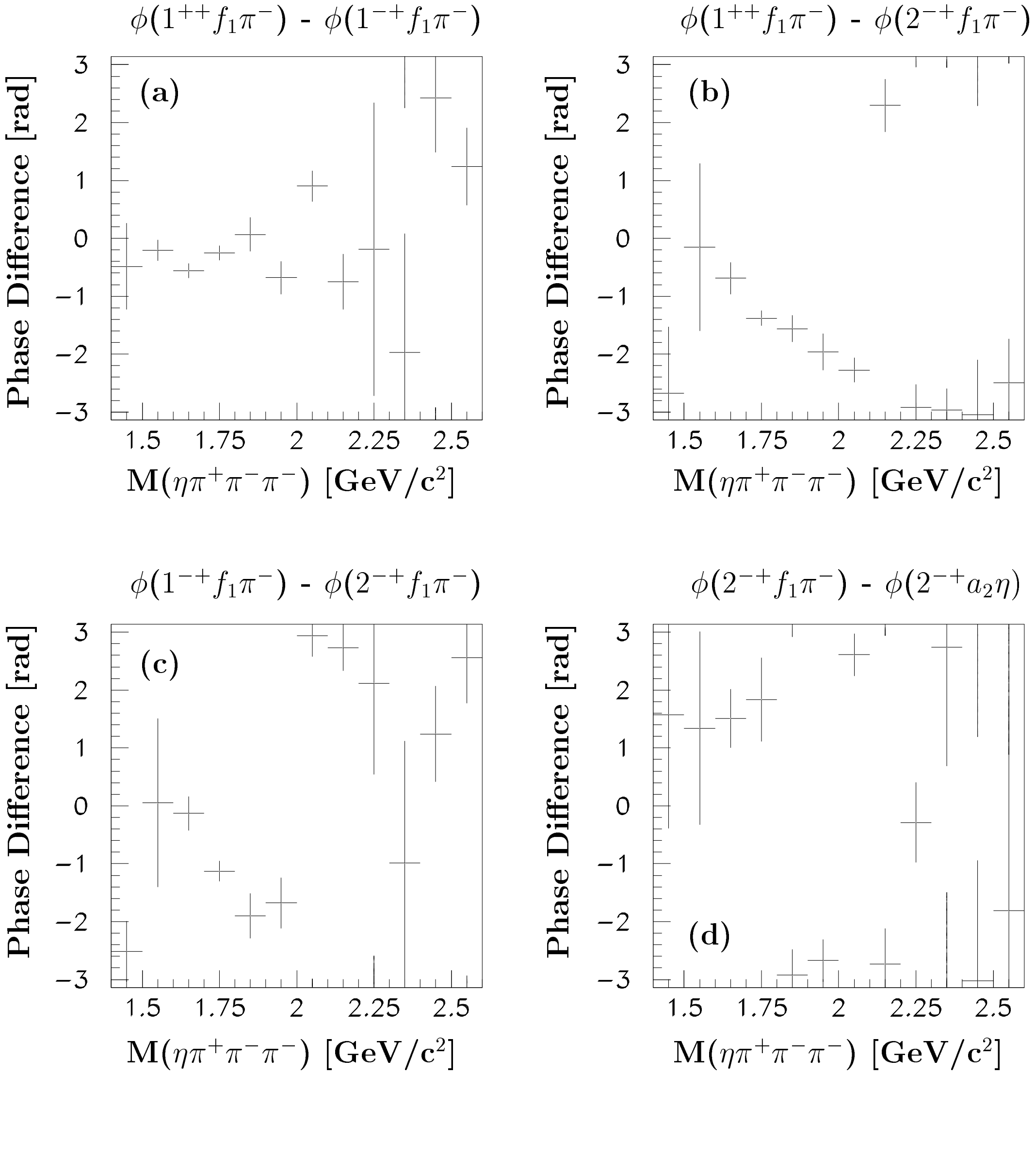

Figure 5.5: Relative phase differences for selected waves from the final fit. The figures are (a) [$\phi(1^{++}0^+P\ f_1(1285)\pi^-)$ - $\phi(1^{-+}1^+S\ f_1(1285)\pi^-)$]; (b) [$\phi(1^{++}0^+P\ f_1(1285)\pi^-)$ - $\phi(2^{-+}0^+D\ f_1(1285)\pi^-)$]; (c) [$\phi(1^{-+}1^+S\ f_1(1285)\pi^-)$ - $\phi(2^{-+}0^+D\ f_1(1285)\pi^-)$]; (d) [$\phi(2^{-+}0^+D\ f_1(1285)\pi^-)$ - $\phi(2^{-+}0^+\mathrm{S}\ a_2^-(1320)\eta)$].

In this analysis, three forms will be used to describe the intensity distributions and phases of the states. These forms are the usual Breit-Wigner, a coupled channel Breit-Wigner [63] and a two-pole K-matrix. The coupled channel describes a state with multiple decay channels with the threshold for one of the channels occurring after the initial state's threshold. The coupled channel approach is described in Appendix A.4. The two-pole K-matrix describes two overlapping resonances in the same wave and guarantees unitarity. The form of the K-matrix is given in Appendix A.5. The intensity distributions are given by

$$I = pqN\frac{F_s^2(q)}{F_s^2(q_0)}|A^2| \tag{5.1}$$

where A is either the Breit-Wigner, coupled channel or K-matrix form and N is an overall normalization factor. $F_s^2(q)$ and $F_s^2(q_0)$ are Blatt-Weisskopf functions (see Appendix A.2) with s equal to the spin of the X^-. q is the breakup momentum of the $X^-\to f_1(1285)\pi^-$ decay and p is the breakup momentum of the X^-p system. The p, q and F_s terms describe the phase space effects. The phase differences are given by

$$\Delta\phi = c_1\phi(A_1) - c_2\phi(A_2) + B \tag{5.2}$$

where A_1 and A_2 are the parametrizations for the two waves, c_1 and c_2 are either 0 or 1 depending on whether the state is hypothesized to be non-resonant or resonant, and B is a function allowing an additional relative phase difference. The B term can be a constant, a linear or a quadratic function of $\eta\pi^+\pi^-\pi^-$ mass. The errors are calculated using the error matrix from the PWA fit. This ensures the correlations between the intensity distributions and phase motions are taken into account.

The three main $f_1(1285)\pi^-$ waves shown in the previous section will be the focus of this analysis. The mass dependent analysis will be limited to the mass bins 1.4-2.4 GeV/c^2. There are many combinations of hypotheses for these three states. The observed shape of the $1^{++}0^{+}P$ $f_1(1285)\pi^-$ intensity distribution has led to restricting its hypothesis to a single Breit-Wigner. There is no evidence for the need for two states to describe that wave. The interesting structure observed in the $1^{-+}1^{+}S$ $f_1(1285)\pi^-$ intensity distribution led to attempts to describe it with both a single Breit-Wigner and a two-pole K-matrix. The shape of the $2^{-+}0^{+}D$ $f_1(1285)\pi^-$ intensity distribution suggests several possibilities. It was hypothesized as a single Breit-Wigner, a coupled channel Breit-Wigner and a two-pole K-matrix. The coupled channel hypothesis was included because the 1.8-2.0 GeV/c^2 bins for the $2^{-+}0^{+}D$ $f_1(1285)\pi^-$ wave has a possible "dip". This occurs at the same mass that the $2^{-+}0^{+}$S $a_2^-(1320)\eta$ is enhanced. The phases of these states have been fitted as either resonant or constant. For the resonant hypothesis the phase is that of the Breit-Wigner or K-matrix forms. The inclusion of the three possible forms of the B term leads to 144 distinct hypotheses for these three waves.

The majority of these hypotheses have been tried with varying success. Tables 5.2 and 5.3 list some of the more interesting hypotheses. Several remarks can be made about the various fits. The phase motion of a resonant state can be approximated by a linear relative production phase (see fits 1 and 2). However, a strongly mass dependent relative production phase is not expected. For this reason, the number of fits which were attempted with a quadratic production phase was limited. Also, fits with a strong linear term were not favored. It was determined that a two-pole K-matrix (which requires interference) made no physical sense as a non-resonant state. Therefore, all two-pole states were required to be resonant. Fits with χ^2/DoF in italics indicate solutions with parameters which are considered unlikely.

Some conclusions can easily be drawn from the MDA fit results. Figure 5.6 shows the PWA intensity distributions used in the MDA and a few of the possible solutions. These solutions have been selected from various fits and are uncorrelated.

TABLE 5.2
SELECTED MDA HYPOTHESES WITH BREIT-WIGNER FORMS

Fit #	1^{++} Type	1^{++} Phase	1^{-+} Type	1^{-+} Phase	2^{-+} Type	2^{-+} Phase	Production Phase	$\frac{\chi^2}{DoF}$
1	BW	Const	BW	Const	BW	Const	Constant	4.397
2	BW	Const	BW	Const	BW	Const	Linear	2.070
3	BW	Res	BW	Const	BW	Const	Constant	*6.200*
4	BW	Const	BW	Res	BW	Const	Constant	*8.658*
5	BW	Const	BW	Const	BW	Res	Constant	2.228
6	BW	Const	BW	Const	BW	Res	Linear	1.945
7	BW	Res	BW	Res	BW	Res	Constant	2.754
8	BW	Res	BW	Res	BW	Res	Linear	3.181

TABLE 5.3
SELECTED MDA HYPOTHESES WITH TWO-POLE K-MATRIX FORMS

Fit #	1^{++} Type	1^{++} Phase	1^{-+} Type	1^{-+} Phase	2^{-+} Type	2^{-+} Phase	Production Phase	$\frac{\chi^2}{DoF}$
9	BW	Const	BW	Const	2 pole	Res	Constant	2.018
10	BW	Const	BW	Const	2 pole	Res	Linear	*1.817*
11	BW	Res	BW	Res	2 pole	Res	Constant	1.914
12	BW	Res	BW	Res	2 pole	Res	Linear	1.775
13	BW	Res	2 pole	Res	2 pole	Res	Constant	*1.761*

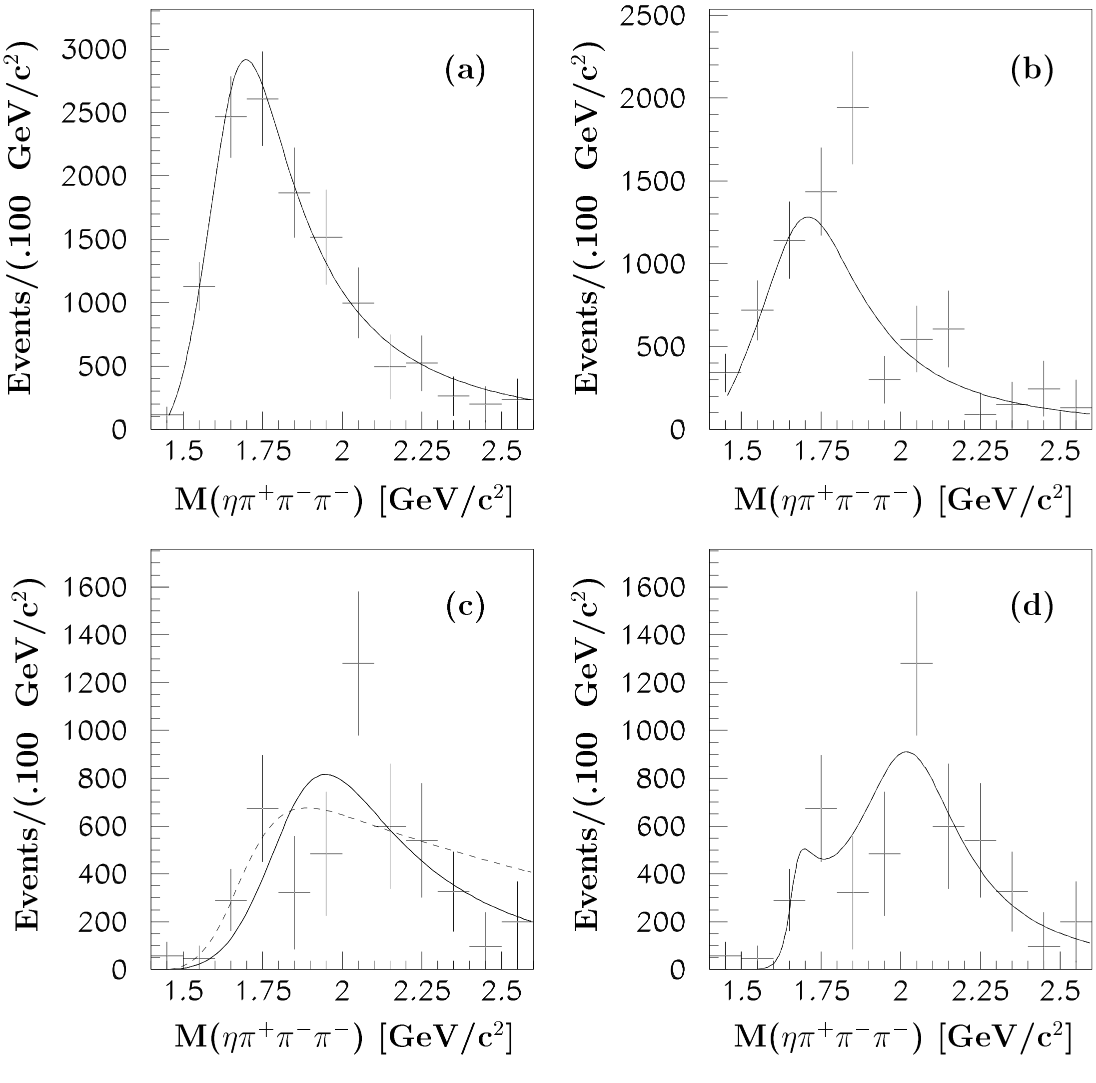

Figure 5.6: Intensity distributions (points) and sample fit results (lines) from the mass dependent analysis. The figures are (a) $1^{++}0^+P$ $f_1(1285)\pi^-$ with single Breit-Wigner solution; (b) $1^{-+}1^+S$ $f_1(1285)\pi^-$ with single Breit-Wigner solution; (c) $2^{-+}0^+D$ $f_1(1285)\pi^-$ with two different single Breit-Wigner solutions; (d) $2^{-+}0^+D$ $f_1(1285)\pi^-$ with two-pole K-matrix solution.

The $1^{++}0^{+}P$ $f_1(1285)\pi^-$ intensity distribution can be well described by a single Breit-Wigner (figure 5.6(a)). The $1^{-+}1^{+}S$ $f_1(1285)\pi^-$ intensity distribution can be partially described by a single Breit-Wigner (figure 5.6(b)). However, the 1.8-1.9 GeV/c^2 bin is not well described in any of the fits. Many fits were attempted with a two-pole K-matrix for the $1^{-+}1^{+}S$ $f_1(1285)\pi^-$ wave. However no acceptable solution was found. The $2^{-+}0^{+}D$ $f_1(1285)\pi^-$ intensity distribution can have either a single Breit-Wigner or a two-pole K-matrix form (figures 5.6(c) and 5.6(d)). Fits with a coupled channel hypothesis favored the coupling going to zero which becomes the single Breit-Wigner form.

The PWA phase difference distributions and selected solutions are shown in figure 5.7. The phase motion between the $1^{++}0^{+}P$ $f_1(1285)\pi^-$ and $1^{-+}1^{+}S$ $f_1(1285)\pi^-$ waves can be described by two resonances with different widths (figure 5.7(a)). However, a constant or linear production phase term can also give an approximate description. The falling phase of the $2^{-+}0^{+}D$ $f_1(1285)\pi^-$ wave against both the $1^{++}0^{+}P$ $f_1(1285)\pi^-$ and $1^{-+}1^{+}S$ $f_1(1285)\pi^-$ waves is best described by a resonant $2^{-+}0^{+}D$ $f_1(1285)\pi^-$ or a linear relative production phase (figures 5.7(b) and 5.7(c)). However, if the $1^{++}0^{+}P$ $f_1(1285)\pi^-$ and $1^{-+}1^{+}S$ $f_1(1285)\pi^-$ waves are resonant the falling phase favors the two-pole K-matrix hypothesis for the $2^{-+}0^{+}D$ $f_1(1285)\pi^-$ wave.

Table 5.4 lists the mass and width parameters for the fits of Table 5.2. Table 5.5 lists the mass and width parameters for the fits of Table 5.3. For solutions with a two-pole K-matrix form, the corresponding T-matrix pole masses and widths are given. All masses and widths are in GeV/c^2. Resonant states are in boldface type.

Based on the χ^2/DoF the majority of the MDA solutions are not good fits. The confidence level for most fits is $\ll .1\%$. These fits have degrees of freedom ranging from 35 to 48. Several of the fits (fits 6, 11, 12) have higher confidence levels, although the best is fit 12 with only a .5% confidence level. Some fits, although

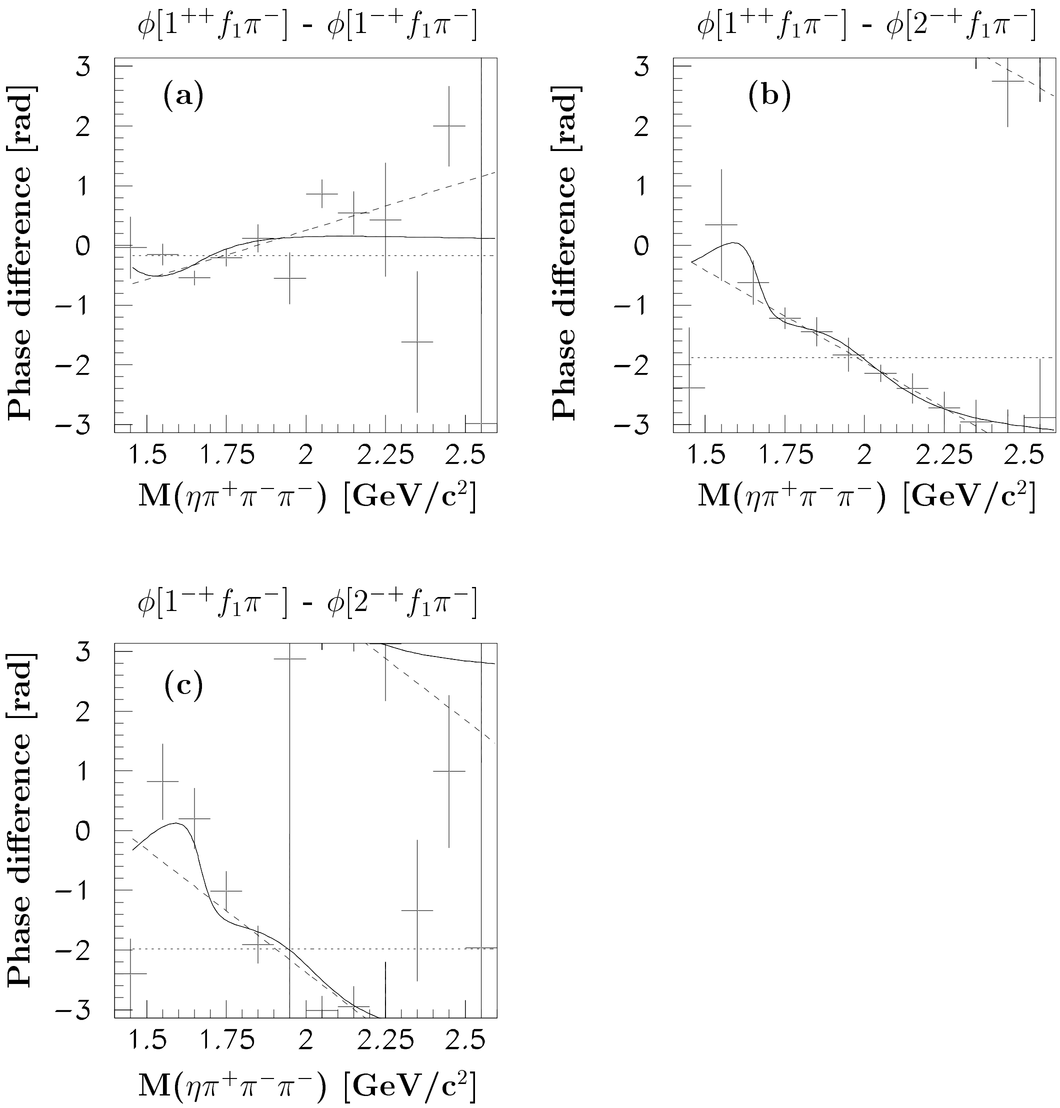

Figure 5.7: ;

(b) $[\phi(1^{++}0^{+}P\ f_1(1285)\pi^-)$ - $\phi(2^{-+}0^{+}D\ f_1(1285)\pi^-)]$; (c) $[\phi(1^{-+}1^{+}S\ f_1(1285)\pi^-)$ - $\phi(2^{-+}0^{+}D\ f_1(1285)\pi^-)]$.]Phase difference (points) and sample fit results (lines) from the mass dependent analysis. The solid lines correspond to resonance phases. The dashed lines correspond to non-resonant phases with linear production phase term. The dotted lines correspond to non-resonant phases with constant production phase term. The figures are (a) $[\phi(1^{++}0^{+}P\ f_1(1285)\pi^-)$ - $\phi(1^{-+}1^{+}S\ f_1(1285)\pi^-)]$; (b) $[\phi(1^{++}0^{+}P\ f_1(1285)\pi^-)$ - $\phi(2^{-+}0^{+}D\ f_1(1285)\pi^-)]$; (c) $[\phi(1^{-+}1^{+}S\ f_1(1285)\pi^-)$ - $\phi(2^{-+}0^{+}D\ f_1(1285)\pi^-)]$.

TABLE 5.4

MASS AND WIDTH PARAMETERS FOR SELECTED MDA HYPOTHESES WITH BREIT-WIGNER FORMS

Fit #	1^{++} Mass	1^{++} Width	1^{-+} Mass	1^{-+} Width	2^{-+} Mass	2^{-+} Width
1	1.74 ±.02	0.399 ±.053	1.73 ±.03	0.406 ±.096	2.17 ±.29	1.729 ±1.531
2	1.74 ±.02	0.411 ±.057	1.73 ±.02	0.365 ±.076	2.11 ±.21	1.444 ±1.154
3	*111. ±14.*	*613.1 ±1.7*	1.73 ±.03	0.406 ±.096	2.00 ±.130	1.245 ±.700
4	1.74 ±.01	0.399 ±.05	1.80 ±.002	$<10^{-5}$	2.17 ±.21	1,728 ±1.09
5	1.73 ±.02	0.395 ±.05	1.73 ±.02	0.373 ±.080	**2.01 ±.05**	**0.612 ±.128**
6	1.73 ±.02	0.399 ±.06	1.73 ±.02	0.366 ±.086	**2.04 ±.07**	**0.792 ±.335**
7	**1.74 ±.01**	**0.414 ±.048**	**1.71 ±.03**	**0.674 ±.158**	**1.93 ±.04**	**0.283 ±.052**
8	**1.75 ±.02**	**0.410 ±.05**	**1.70 ±.03**	**0.426 ±.078**	**1.93 ±.08**	**0.786 ±,352**

TABLE 5.5
MASS AND WIDTH PARAMETERS FOR SELECTED MDA HYPOTHESES WITH TWO-POLE K-MATRIX FORMS

Fit #	1^{++} Mass	1^{++} Width	1st 1^{-+} Mass	1st 1^{-+} Width	2nd 1^{-+} Mass	2nd 1^{-+} Width	1st 2^{-+} Mass	1st 2^{-+} Width	2nd 2^{-+} Mass	2nd 2^{-+} Width
9	1.74 $\pm$.02	0.410 $\pm$.052	1.73 $\pm$.02	0.382 $\pm$.072	–	–	**1.67**	**0.215**	**1.73**	**0.402**
10	1.74 $\pm$.003	0.418 $\pm$.008	1.72 $\pm$.005	0.372 $\pm$.011	–	–	**1.70**	**0.220**	*31.8*	$<10^{-6}$
11	**1.75 $\pm$.01**	**0.321 $\pm$.023**	**1.71 $\pm$.02**	**0.467 $\pm$.052**	–	–	**1.68**	**0.084**	**2.04**	**0.408**
12	**1.75 $\pm$.01**	**0.402 $\pm$.048**	**1.72 $\pm$.02**	**0.411 $\pm$.074**	–	–	**1.51**	**1.002**	**1.70**	**0.185**
13	**1.75 $\pm$.01**	**0.362 $\pm$.029**	<1.4	*1.4*	*2.35*	$<10^{-7}$	**1.68**	**0.087**	**2.04**	**0.424**

their χ^2/DoF may be relatively low, have been discounted because the resulting fit makes little sense. Examples include solutions with masses or widths which are unreasonably large (> 5 GeV/c^2) or unreasonably small ($< .005$ GeV/c^2) (see fits 3, 4, 10 and 13).

The three best MDA fits are presented in figures 5.8, 5.9, and 5.10. These fits show the preferred solutions for the mass dependent analysis. The best fit for the hypothesis of no resonant states is presented in figure 5.11. The mass dependent analysis favors hypotheses with resonant states particularly in the $2^{-+}0^+D$ $f_1(1285)\pi^-$ wave. The $1^{++}0^+P$ $f_1(1285)\pi^-$ and $1^{-+}1^+S$ $f_1(1285)\pi^-$ waves are linked and need to be either both resonant or both non-resonant. If the $1^{++}0^+P$ $f_1(1285)\pi^-$ and $1^{-+}1^+S$ $f_1(1285)\pi^-$ waves are resonant, the two-pole solution for the $2^{-+}0^+D$ $f_1(1285)\pi^-$ wave is favored. However, none of the fits are sufficient to determine the proper solution with high confidence.

The $1^{++}0^+P$ $f_1(1285)\pi^-$ intensity distribution is clearly described by a single Breit-Wigner. Nearly all of the fits find the same parameters for this Breit-Wigner. The mass is found to be approximately 1.74 ± 0.02 GeV/c^2. The width is approximately $.40 \pm .05$ GeV/c^2. The $1^{-+}1^+S$ $f_1(1285)\pi^-$ intensity distribution shows strong evidence for an enhancement at about $1.73 \pm .07$ GeV/c^2. The MDA finds the width of this enhancement to be about $.38 \pm .07$ GeV/c^2. The $2^{-+}0^+D$ $f_1(1285)\pi^-$ intensity distribution and phase motion allows for either a single Breit-Wigner or a two-pole solution. The single Breit-Wigner solution gives a mass near 2.0 GeV/c^2 and a width ranging from .28 to 1.73 GeV/c^2. For the two-pole solution, the lower pole is found to be near $1.69 \pm .02$ GeV/c^2 with a width of approximately $.20 \pm .05$ GeV/c^2. The higher pole is usually found near $2.05 \pm .02$ GeV/c^2, but the width varies from .4 GeV/c^2 to 1.0 GeV/c^2.

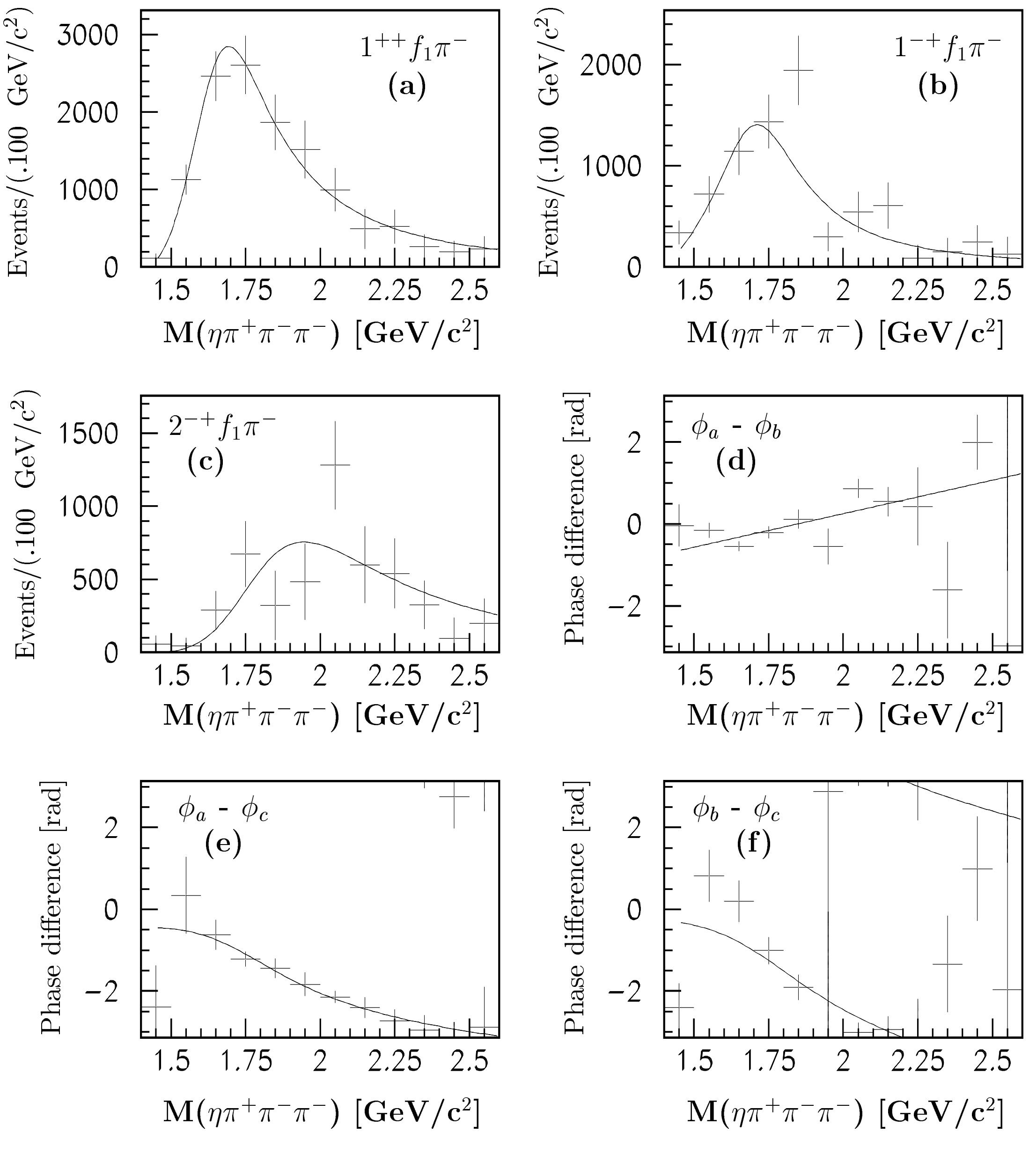

Figure 5.8: Solution of mass dependent analysis for fit 6. The figures are (a) $1^{++}0^+P$ $f_1(1285)\pi^-$ intensity; (b) $1^{-+}1^+S$ $f_1(1285)\pi^-$ intensity; (c) $2^{-+}0^+D$ $f_1(1285)\pi^-$ intensity; (d) $[\phi(1^{++}0^+P\ f_1(1285)\pi^-)$ - $\phi(1^{-+}1^+S\ f_1(1285)\pi^-)]$; (e) $[\phi(1^{++}0^+P$ $f_1(1285)\pi^-)$ - $\phi(2^{-+}0^+D\ f_1(1285)\pi^-)]$; (f) $[\phi(1^{-+}1^+S\ f_1(1285)\pi^-)$ - $\phi(2^{-+}0^+D$ $f_1(1285)\pi^-)]$. Note: $\phi_a = \phi(1^{++}0^+P\ f_1(1285)\pi^-)$, $\phi_b = \phi(1^{-+}1^+S\ f_1(1285)\pi^-)$, and $\phi_c = \phi(2^{-+}0^+D\ f_1(1285)\pi^-)$.

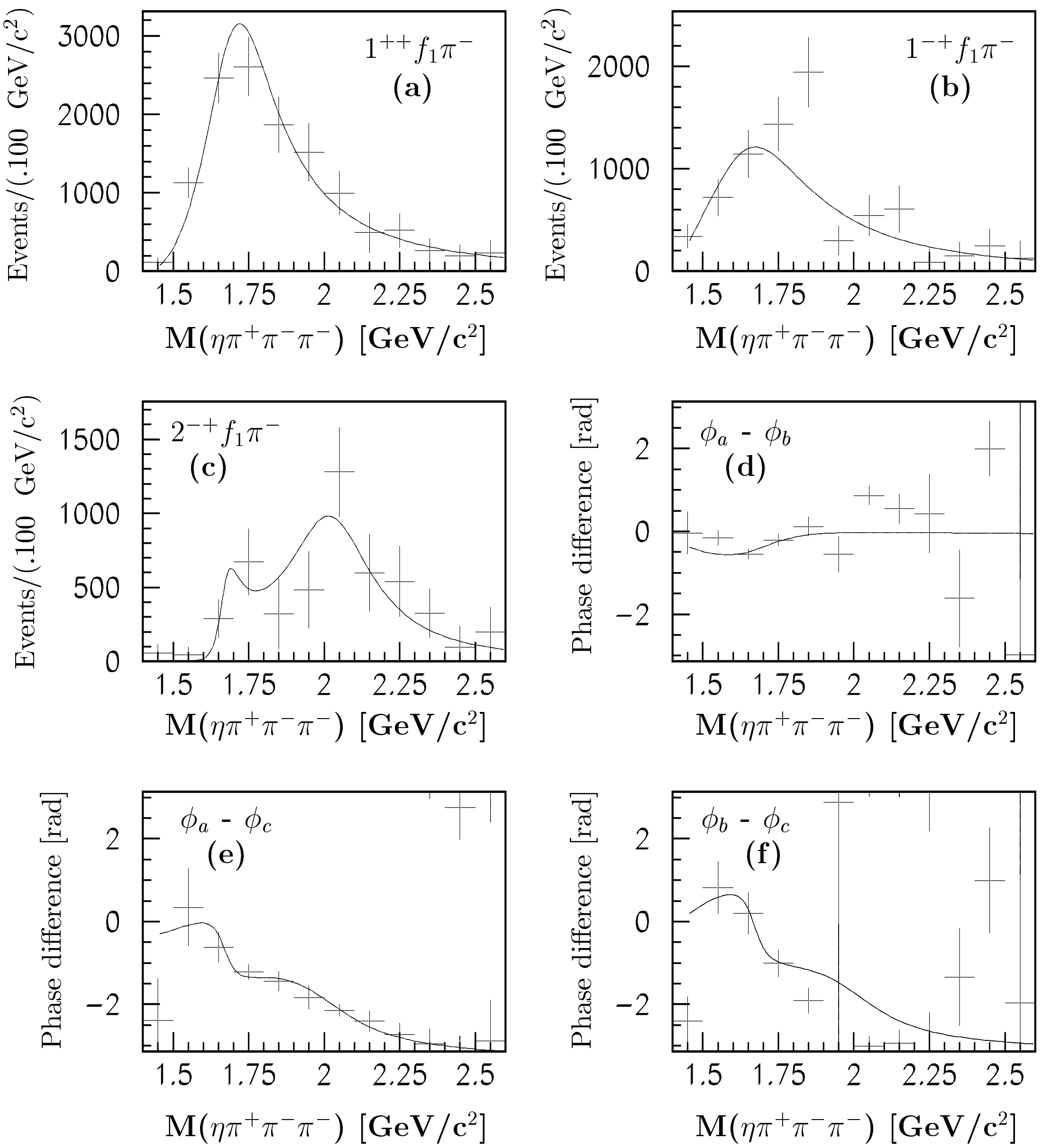

Figure 5.9: Solution of mass dependent analysis for fit 11. The figures are (a) $1^{++}0^+P$ $f_1(1285)\pi^-$ intensity; (b) $1^{-+}1^+S$ $f_1(1285)\pi^-$ intensity; (c) $2^{-+}0^+D$ $f_1(1285)\pi^-$ intensity; (d) $[\phi(1^{++}0^+P\ f_1(1285)\pi^-)$ - $\phi(1^{-+}1^+S\ f_1(1285)\pi^-)]$; (e) $[\phi(1^{++}0^+P\ f_1(1285)\pi^-)$ - $\phi(2^{-+}0^+D\ f_1(1285)\pi^-)]$; (f) $[\phi(1^{-+}1^+S\ f_1(1285)\pi^-)$ - $\phi(2^{-+}0^+D\ f_1(1285)\pi^-)]$. Note: $\phi_a = \phi(1^{++}0^+P\ f_1(1285)\pi^-)$, $\phi_b = \phi(1^{-+}1^+S\ f_1(1285)\pi^-)$, and $\phi_c = \phi(2^{-+}0^+D\ f_1(1285)\pi^-)$.

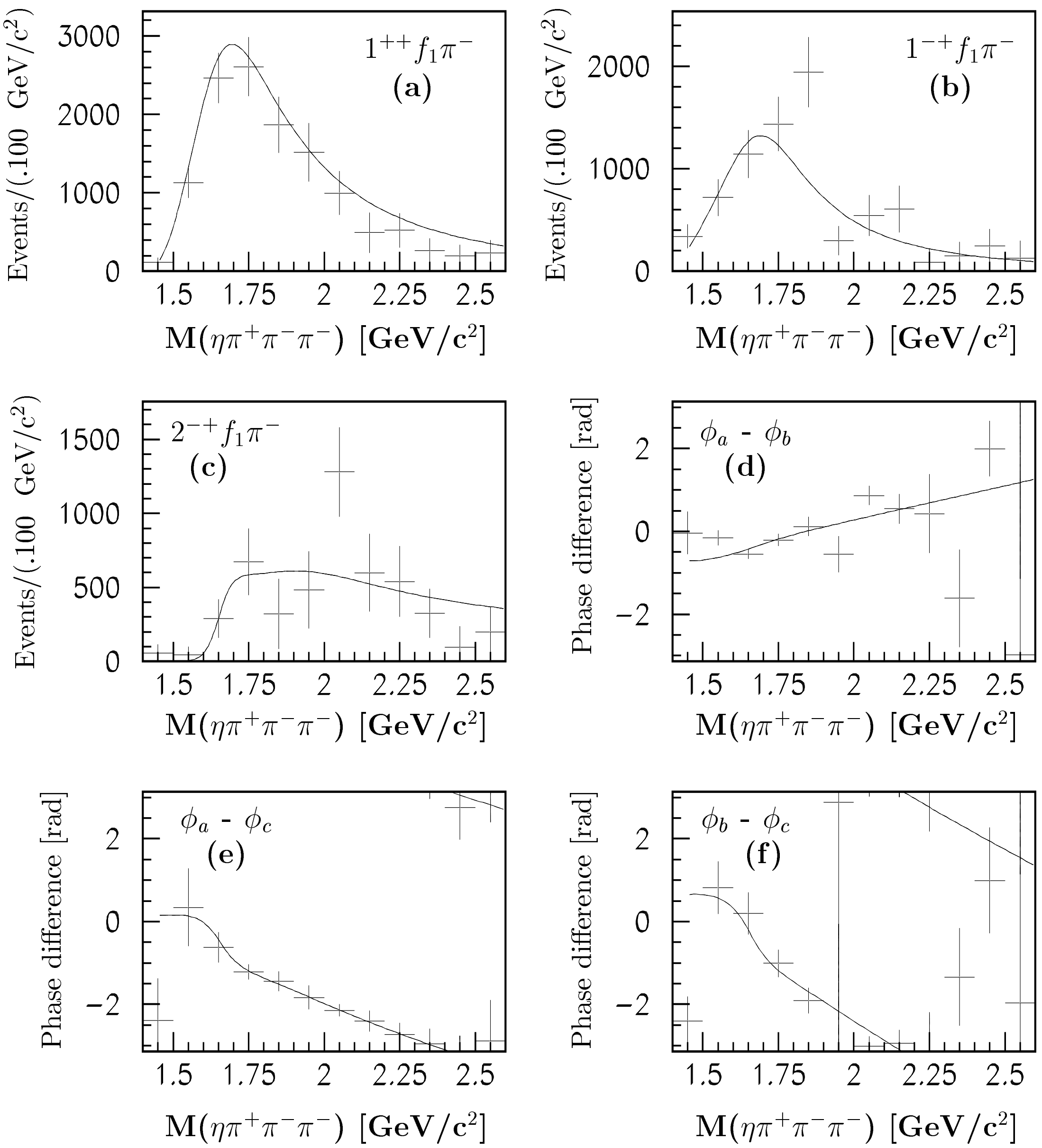

Figure 5.10: Solution of mass dependent analysis for fit 12. The figures are (a) $1^{++}0^+P$ $f_1(1285)\pi^-$ intensity; (b) $1^{-+}1^+S$ $f_1(1285)\pi^-$ intensity; (c) $2^{-+}0^+D$ $f_1(1285)\pi^-$ intensity; (d) $[\phi(1^{++}0^+P\ f_1(1285)\pi^-)$ - $\phi(1^{-+}1^+S\ f_1(1285)\pi^-)]$; (e) $[\phi(1^{++}0^+P\ f_1(1285)\pi^-)$ - $\phi(2^{-+}0^+D\ f_1(1285)\pi^-)]$; (f) $[\phi(1^{-+}1^+S\ f_1(1285)\pi^-)$ - $\phi(2^{-+}0^+D\ f_1(1285)\pi^-)]$. Note: $\phi_a = \phi(1^{++}0^+P\ f_1(1285)\pi^-)$, $\phi_b = \phi(1^{-+}1^+S\ f_1(1285)\pi^-)$, and $\phi_c = \phi(2^{-+}0^+D\ f_1(1285)\pi^-)$.

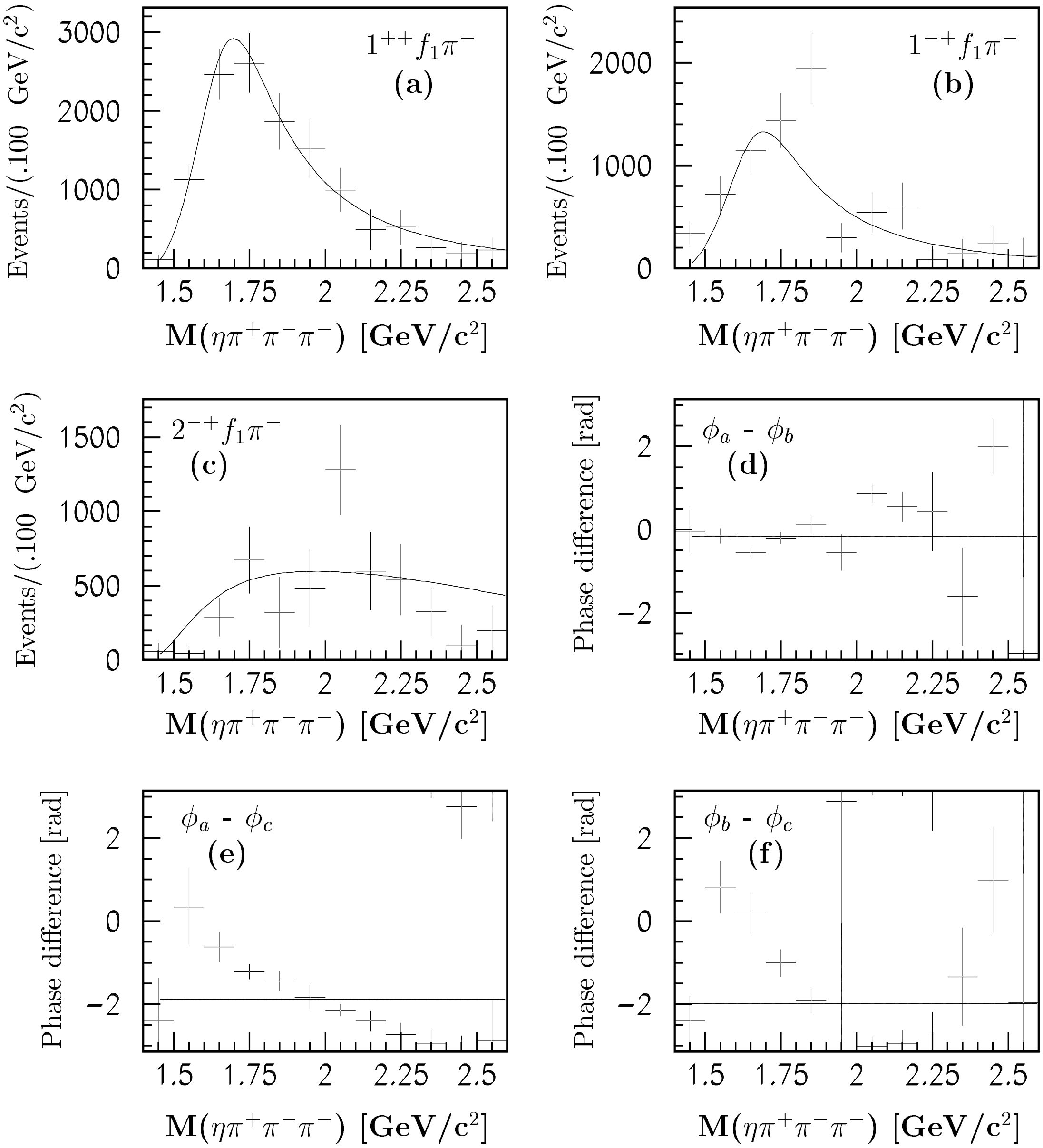

Figure 5.11: Solution of mass dependent analysis for hypothesis with no resonant phase motion and constant relative production phase (fit 1). The figures are (a) $1^{++}0^+P$ $f_1(1285)\pi^-$ intensity; (b) $1^{-+}1^+S$ $f_1(1285)\pi^-$ intensity; (c) $2^{-+}0^+D$ $f_1(1285)\pi^-$ intensity; (d) [$\phi(1^{++}0^+P\ f_1(1285)\pi^-)$ - $\phi(1^{-+}1^+S\ f_1(1285)\pi^-)$]; (e) [$\phi(1^{++}0^+P\ f_1(1285)\pi^-)$ - $\phi(2^{-+}0^+D\ f_1(1285)\pi^-)$]; (f) [$\phi(1^{-+}1^+S\ f_1(1285)\pi^-)$ - $\phi(2^{-+}0^+D\ f_1(1285)\pi^-)$]. Note: $\phi_a = \phi(1^{++}0^+P\ f_1(1285)\pi^-)$, $\phi_b = \phi(1^{-+}1^+S\ f_1(1285)\pi^-)$, and $\phi_c = \phi(2^{-+}0^+D\ f_1(1285)\pi^-)$.

5.4 Interpretation

The interpretation of the results is the most critical part of the analysis. This section compares the final results to previous experiments and theoretical predictions. The important previous experiments were discussed in Chapter 1. They include BNL 818 [16], VES [15] and FNAL 687 [20]. The theoretical predictions were also described in Chapter 1. Additional predictions about possible states are described below. This section also gives the most likely interpretations.

The mass dependent analysis failed to give a definitive answer to the question of what resonant states are produced in the $f_1(1285)/\eta(1295)\pi^-$ system. The hypotheses with one resonance (in the $2^{-+}0^+D$ $f_1(1285)\pi^-$ wave) or four resonances (one each in $1^{++}0^+P$ $f_1(1285)\pi^-$, $1^{-+}1^+S$ $f_1(1285)\pi^-$and $2^{-+}0^+D$ $f_1(1285)\pi^-$ with a second in $2^{-+}0^+D$ $f_1(1285)\pi^-$) appear the most likely. Additional work is necessary to determine the exact answer. This work could include the additional statistics of the 1995 E852 data, analysis of other decay modes or input from other experiments such as VES. However, the analysis presented here can provide some very useful insight into the $f_1(1285)\pi^-$ system.

The $1^{++}0^+P$ $f_1(1285)\pi^-$ intensity distribution is in agreement with the results of both BNL 818 [16, 19] and VES [15]. Both show a large enhancement in the $1^{++}0^+P$ $f_1(1285)\pi^-$ near 1.7 GeV/c^2. Neither experiment has published a mass or width for this enhancement. BNL 818 interprets the phase motion indicating that this state may be resonant. FNAL 687 does not find any $1^{++}0^+P$ $f_1(1285)\pi^-$ produced in photoproduction. The mass dependent analysis for the E852 data does not confirm or deny the resonant status of the $1^{++}0^+P$ $f_1(1285)\pi^-$ wave. However, the intensity distribution and phase motion can be well described by a single resonant Breit-Wigner.

A recent paper by T. Barnes *et al.* [68] lists two possible 1^{++} states in the 1.7

GeV/c^2 region. These possible states are based upon calculations from the flux tube model [13] and the $^3P_0$ model. The two states are the $a_1(1700)$ which is a radial excitation of the $a_1(1260)$ and the $a_{1(H)}(1700)$ which is a hybrid. Both of these states have comparable widths (.25-.3 GeV/c^2). A possible 1^{++} state near 1.7 GeV/c^2 has been seen in analysis of the E852 $\pi^+\pi^-\pi^-$ data [69]. This state may be narrower (approximately .25-.35 GeV/c^2) than the $f_1(1285)\pi^-$ state. If the $1^{++}0^+P$ $f_1(1285)\pi^-$ wave is resonant, the determination of whether this state is $q\bar{q}$ or hybrid may require analysis of the $b_1(1235)\pi$ system to provide branching ratios.

The observation of the $1^{-+}1^+S$ $f_1(1285)\pi^-$ wave is in agreement with the results of BNL 818, VES and FNAL 687. Its production via f_2(1270 or $\rho^0(770)$ exchange (for π^-p reactions) agrees with BNL 818 and VES. VES has published no other claims about the $1^{-+}1^+S$ $f_1(1285)\pi^-$ wave. BNL 818 interprets this wave as having two parts. The low mass region (near 1.7 GeV/c^2) is non-resonant while the higher mass region (near 2.0 GeV/c^2) may be resonant. That interpretation is not supported by this analysis. The intensity distribution is significantly different in the 1.8-2.1 GeV/c^2 region. There is little evidence for a resonant state at 2.0 GeV/c^2. There is the possibility of a resonant (or non-resonant) state in the E852 data near 1.7 GeV/c^2. This analysis does not observe the significant 1^{-+} $\eta(1295)\pi^-$ in the low mass region which is seen by BNL 818. While the interpretation is not supported there is fair agreement between the intensity distribution and phase differences of the two experiment. A $1^{-+}1^+S$ $f_1(1285)\pi^-$ state at 1.73 GeV/c^2 is in agreement with the FNAL 687 peak at 1.776 $\pm$ .013 GeV/c^2. However, the FNAL 687 width is significantly narrower (.155 $\pm$ .04 GeV/c^2).

A J^{PC}= 1^{-+} resonant state must be an exotic meson, probably a hybrid. This analysis is unable to provide conclusive evidence for a resonant $1^{-+}1^+S$ $f_1(1285)\pi^-$ state, but gives significant support for one. The flux tube model [11, 12, 13] predicts the lowest lying hybrids to be near 1.8 GeV/c^2. The experimental evidence for a

$1^{-+}1^{+}S$ $f_1(1285)\pi^-$ state is mounting. Once again, the confirmation of a hybrid 1^{-+} state may depend upon analysis of the $b_1(1235)\pi$ final state. A possible $J^{PC}= 1^{-+}$ state near 1.6 GeV/c^2 has also been observed in the analysis of the E852 $\pi^+\pi^-\pi^-$ data [69]. The mass dependent analysis of the $\pi^+\pi^-\pi^-$ PWA result gives a mass and width of $1.593 \pm .008$ and $.168 \pm .02$, respectively.

Very little is known of the $2^{-+}0^{+}D$ $f_1(1285)\pi^-$ wave from previous experimental work. BNL 818 claims the $2^{-+}0^{+}D$ $f_1(1285)\pi^-$ wave is insignificant and it is left out of their final fit. No plots of this wave have been published. VES has not published any distributions for the $2^{-+}0^{+}D$ $f_1(1285)\pi^-$ wave and makes no claims about it or its existence. This analysis suggests a significant contribution from the $2^{-+}0^{+}D$ $f_1(1285)\pi^-$ wave. The mass dependent analysis favors the presence of one or two possible states. The phase motion indicates the states may be resonant.

Although no proper solution could be found in this analysis, the coupled channel parametrization for the $2^{-+}0^{+}D$ $f_1(1285)\pi^-$ may hold promise. The fact that a dip occurs in the $2^{-+}0^{+}D$ $f_1(1285)\pi^-$ intensity distribution in the same mass bin as the beginning of the $2^{-+}0^{+}$S $a_2^-(1320)\eta$ wave is evidence for a single state with two decay modes. An improved parametrization which includes the slow threshold turn-on of the $a_2^-(1320)\eta$ wave (due to the width of the $a_2^-(1320)$) might help. The full $\eta\pi^+\pi^-\pi^-$ analysis should show whether the $2^{-+}0^{+}D$ $f_1(1285)\pi^-$ and $2^{-+}0^{+}$S $a_2^-(1320)\eta$ waves represent different decay modes of the same state. It could also determine a fixed value for the ratio of the coupling constants (r).

The theoretical possibilities for any $2^{-+}0^{+}D$ $f_1(1285)\pi^-$ states are not clear. If there are two states, the lower state ($m = 1.68$ GeV/c^2, $\Gamma = .09$ GeV/c^2) may correspond to the $\pi_2(1670)$. T. Barnes *et al.* [68] gives a small partial width (.001 GeV/c^2) for the $\pi_2(1670)$ decaying to $f_1(1285)\pi$. Previous experimental evidence [18] indicates a wider width ($.258 \pm .018$) than seen in this analysis. No theoretical prediction has been found for the nature of a higher mass $2^{-+}0^{+}D$ $f_1(1285)\pi^-$ state.

Although the other $f_1(1285)\pi^-$ waves (figure 5.2) were not included in the mass dependent analysis some statements can be made about them. The magnitude of the $1^{-+}1^+$D $f_1(1285)\pi^-$ wave shows that any $1^{-+}1^+$ $f_1(1285)\pi^-$ states have a small D/S ratio. The magnitude of the $2^{-+}1^+$D $f_1(1285)\pi^-$ wave is also much smaller than its m=0 partner. The $3^{++}1^+$F $f_1(1285)\pi^-$ wave is not insignificant, but further analysis requires higher statistics. The $1^{-+}1^+$ $\eta(1295)\pi^-$ intensity (in the 1.7 GeV/c^2 region) found by BNL 818 is not observed in this analysis.

Interpretations of the non-$f_1(1285)/\eta(1295)\pi^-$ waves are extremely tentative. An interesting structure is seen in the intensity distribution for the $2^{-+}0^+$S $a_2^-(1320)\eta$ wave. The mass and width of this structure (as seen by this analysis) are not consistent with the $\pi_2(1670)$. The possibility remains that this wave is coupled to the $2^{-+}0^+D$ $f_1(1285)\pi^-$ wave. The enhancement seen in the intensity distribution for the $1^{++}0^+$P $\rho^0(770)a_0^-(980)$ wave is in the same region as the enhancement of the $1^{++}0^+P$ $f_1(1285)\pi^-$ wave. This could be either the $a_1(1700)$ or $a_{1(H)}(1700)$. T. Barnes *et al.* provides no partial width for $a_1(1700) \rightarrow \rho^0(770)a_0^-(980)$. The $1^{-+}1^+$S $\rho^0(770)a_0^-(980)$ wave is exotic which makes it extremely interesting. All conclusions about the non-$f_1(1285)/\eta(1295)\pi^-$ waves are premature without the full $\eta\pi^+\pi^-\pi^-p$ analysis without the $f_1(1285)$ cut applied.

CHAPTER 6

CONCLUSIONS

This work has provided a significant study of the $f_1(1285)\pi^-$ system in the $\eta\pi^+\pi^-\pi^-p$ data sample from the E852 experiment. The data were found to be of high quality. A partial-wave analysis of 12,000 selected $\eta\pi^+\pi^-\pi^-p$ events has been performed. It was shown that all waves in this analysis were produced through natural parity exchange. The most significant waves in this analysis were the $1^{++}0^+P\ f_1(1285)\pi^-$, $1^{-+}1^+S\ f_1(1285)\pi^-$and $2^{-+}0^+D\ f_1(1285)\pi^-$ waves. The $1^{-+}1^+S\ f_1(1285)\pi^-$ wave is found to be needed by the partial-wave analysis at greater than 99.99% confidence level. This wave (if resonant) has expressly exotic quantum numbers and may represent a hybrid meson. The partial-wave analysis also demonstrates there is no significant contribution from $\eta(1295)\pi^-$ waves.

The three strongest $f_1(1285)\pi^-$ waves ($1^{++}0^+P\ f_1(1285)\pi^-$, $1^{-+}1^+S\ f_1(1285)\pi^-$, and $2^{-+}0^+D\ f_1(1285)\pi^-$) have been studied in a mass dependent analysis which attempted to simultaneously describe the intensity distributions and the relative phase differences between the waves. No simple hypothesis was found which completely describes the results of the partial-wave analysis. The $1^{++}0^+P\ f_1(1285)\pi^-$ intensity distribution and phase motion can be well described by a single Breit-Wigner with a mass and width of 1.74 ± 0.02 GeV/c^2 and $.40 \pm .05$ GeV/c^2, respectively. The $1^{-+}1^+S\ f_1(1285)\pi^-$ intensity distribution and phase motion can be described over most of the mass range by a single Breit-Wigner with a mass and width of $1.73 \pm .07$ GeV/c^2 and $.38 \pm .07$ GeV/c^2, respectively. The $2^{-+}0^+D$ $f_1(1285)\pi^-$ intensity distribution and phase motion can be described by a single Breit-Wigner with a mass near 2.0 GeV/c^2 and a width between .28 and 1.73 GeV/c^2. The $2^{-+}0^+D$ $f_1(1285)\pi^-$ intensity distribution and phase motion can also be described by two overlapping resonances. These resonances have masses of $1.69 \pm .02$ GeV/c^2 and $2.05 \pm .02$ GeV/c^2. The lower resonance has a width of $.20 \pm .05$ GeV/c^2. The higher resonance has a width between .4 and 1.0 GeV/c^2.

The mass dependent analysis was unable to conclusively identify a unique hypothesis. However, some important observations can be made:

- The $1^{++}0^+P$ $f_1(1285)\pi^-$ and $1^{-+}1^+S$ $f_1(1285)\pi^-$ waves are linked together by their phase motion. If one is resonant then both are resonant.

- The no resonant hypothesis can not describe the phase motion without some production process which has a mass dependent phase.

- If resonances are not present, some other explanation is necessary for the intensity distributions.

- There are theoretical explanations for resonances in the $1^{++}0^+P$ $f_1(1285)\pi^-$, $1^{-+}1^+S$ $f_1(1285)\pi^-$ and $2^{-+}0^+D$ $f_1(1285)\pi^-$ waves.

For these reasons, the distributions, analysis and interpretation favor the four resonance hypothesis (one $1^{++}0^+P$ $f_1(1285)\pi^-$ resonance, one $1^{-+}1^+S$ $f_1(1285)\pi^-$ resonance and two $2^{-+}0^+D$ $f_1(1285)\pi^-$ resonances). This gives the $1^{++}0^+P$ $f_1(1285)\pi^-$ as a candidate for either the $a_1(1700)$ or the $a_{1(H)}(1700)$. The $1^{-+}1^+S$ $f_1(1285)\pi^-$ is a hybrid candidate. The lower $2^{-+}0^+D$ $f_1(1285)\pi^-$ pole may be the $\pi_2(1670)$. The higher $2^{-+}0^+D$ $f_1(1285)\pi^-$ pole is an unknown. The intensity distributions and relative phase differences support this interpretation.

Several other waves of interest are seen in the partial-wave analysis. These include the $2^{++}1^{+}$P $f_1(1285)\pi^-$, $3^{++}0^{+}$F $f_1(1285)\pi^-$, $1^{++}0^{+}$P $\rho^0(770)a_0^-(980)$ and the 2^{-+}S $a_2^-(1320)\eta$ waves. The $1^{++}0^{+}$P $\rho^0(770)a_0^-(980)$ wave could be a decay mode of either the $a_1(1700)$ or the $a_{1(H)}(1700)$. The 2^{-+}S $a_2^-(1320)\eta$ wave could be the related to the $2^{-+}0^{+}D$ $f_1(1285)\pi^-$ wave.

There is still plenty of opportunity for this analysis to be extended. The data from the 1995 run of E852 should add an additional factor of two in statistics. This will allow the higher mass regions to be studied more effectively. Other decay modes of the $f_1(1285)\pi^-$ system are available in the E852 data. These can be studied independently or possibly combined with the set used in this analysis. The 1997 data run will include identification of charged kaons in the final state which allows for even more decay modes of the $f_1(1285)\pi^-$ system. Analysis of the $f_1(1285)\pi^0$ system could confirm or contradict the conclusions of this analysis. Also, analysis of the $b_1(1235)\pi$ can help confirm the hybrid identification of any states. This analysis has shown there are possible non-$f_1(1285)/\eta(1295)\pi^-$ states in the $\eta\pi^+\pi^-\pi^-p$ data which may be of interest. The higher mass region (>2.0 GeV/c^2) has quite a bit of data which is rejected by the $f_1(1285)$ cut. Any future studies could shed light upon these waves by performing a full $\eta\pi^+\pi^-\pi^-p$ analysis which does not include the $f_1(1285)$ cut.

Appendix A

PARTIAL WAVE ANALYSIS

The details of the partial-wave analysis (PWA) as it applies to the $\eta\pi^+\pi^-\pi^-$ state are described in this section. The partial-wave analysis was done with the Brookhaven National Laboratory PWA system modified to handle the $\eta\pi^+\pi^-\pi^-$ state. It is based upon the isobar method [70, 50] expanded for four-body states. The BNL PWA system was originally used for BNL 771, modified for BNL 818 and expanded for the current work.

A.1 Additional Isobar Decay Chains

Tables A.1 and A.2 give an extended list of decay chains which result in an $\eta\pi^+\pi^-\pi^-$ final state. The diagrams for the two types of decay chains are shown in figure 4.1. The marked states (*) were used in this analysis. The other states were not used for various reasons. One reason is that the decay mode had a small branching ratio (i.e. $BR(\omega \to \pi^+\pi^-) = (2.21 \pm .03)\%$) or was unconfirmed (i.e. $f_1(1420) \to \eta\pi^+\pi^-$ possibly seen). Another reason is the lack of evidence for the state in the mass spectra (no $\rho(1700) \to \eta\pi^+\pi^-$ seen in the $\eta\pi^+\pi^-$ mass spectrum). There are even less likely states which are not listed here.

TABLE A.1
POSSIBLE PRIMARY DECAY MODES FOR THE $\eta\pi^+\pi^-\pi^-$ STATE

Primary Decay	Secondary Decay	Tertiary Decay
* $X^- \to f_1(1285)\pi^-$	$f_1(1285) \to a_0(980)\pi$ $f_1(1285) \to (\pi^+\pi^-)_s\eta$	$a_0(980) \to \eta\pi$ $(\pi^+\pi^-)_s \to \pi^+\pi^-$
* $X^- \to \eta(1295)\pi^-$	$\eta(1295) \to a_0(980)\pi$ $\eta(1295) \to (\pi^+\pi^-)_s\eta$	$a_0(980) \to \eta\pi$ $(\pi^+\pi^-)_s \to \pi^+\pi^-$
* $X^- \to a_2^-(1320)\eta$	$a_2^-(1320) \to \rho^0(770)\pi^-$	$\rho^0(770) \to \pi^+\pi^-$
* $X^- \to a_1^-(1260)\eta$	$a_1^-(1260) \to \rho^0(770)\pi^-$	$\rho^0(770) \to \pi^+\pi^-$
$X^- \to \eta'\pi^-$	$\eta' \to \eta\pi^+\pi^-$	
$X^- \to f_1(1420)\pi^-$	$f_1(1420) \to \eta\pi^+\pi^-$	
$X^- \to \eta(1440)\pi^-$	$\eta(1440) \to a_0(980)\pi$	$a_0(980) \to \eta\pi$
$X^- \to \rho(1700)\pi^-$	$\rho(1700) \to \rho^0(770)\eta$	$\rho^0(770) \to \pi^+\pi^-$
$X^- \to h_1^-(1170)\eta$	$h_1^-(1170) \to \rho^0(770)\pi^-$	$\rho^0(770) \to \pi^+\pi^-$
$X^- \to \pi^-(1300)\eta$	$\pi^-(1300) \to \rho^0(770)\pi^-$	$\rho^0(770) \to \pi^+\pi^-$

TABLE A.2
POSSIBLE DOUBLE ISOBAR DECAY MODES FOR THE $\eta\pi^+\pi^-\pi^-$ STATE

Primary Decay	Secondary Decay A	Secondary Decay B
* $X^- \to \rho^0(770)a_0^-(980)$	$\rho^0(770) \to \pi^+\pi^-$	$a_0^-(980) \to \eta\pi^-$
* $X^- \to \sigma a_0^-(980)$	$\sigma \to \pi^+\pi^-$	$a_0^-(980) \to \eta\pi^-$
$X^- \to \rho^0(770)a_2^-(1320)$	$\rho^0(770) \to \pi^+\pi^-$	$a_2^-(1320) \to \eta\pi^-$
$X^- \to \sigma a_2^-(1320)$	$\sigma \to \pi^+\pi^-$	$a_2^-(1320) \to \eta\pi^-$
$X^- \to \omega^0(782)a_0^-(980)$	$\omega^0(782) \to \pi^+\pi^-$	$a_0^-(980) \to \eta\pi$
$X^- \to \omega^0(782)a_2^-(1320)$	$\omega^0(782) \to \pi^+\pi^-$	$a_2^-(1320) \to \eta\pi$
$X^- \to f_2(1270)a_0^-(980)$	$f_2(1270) \to \pi^+\pi^-$	$a_0^-(980) \to \eta\pi$
$X^- \to f_2(1270)a_2^-(1320)$	$f_2(1270) \to \pi^+\pi^-$	$a_2^-(1320) \to \eta\pi$

A.2 Decay Amplitudes for Primary Decays

For primary decays (see figure 4.1(a)), the unsymmetrized decay amplitudes, ${}^{\epsilon}A_b(\tau)$, described in Chapter 4, can be factored into several parts, one depending only on angular information $(\Omega, \Omega_h, \Omega_{h'})$ and the others containing all known dependence on the isobar masses (w, w') and momenta. Explicitly, this can be written as

$$ {}^{\epsilon}A_b(\tau) = {}^{\epsilon}E_m^{J\ell s\ell'\sigma *}(\Omega, \Omega_h, \Omega_{h'}) Q_{\ell s}^{v}(w) Q_{\ell'\sigma}^{v'}(w') \tag{A.1} $$

where ${}^{\epsilon}E_m^{J\ell s\ell'\sigma *}(\Omega, \Omega_h, \Omega_{h'})$ contains the angular dependence and $Q_{\ell s}^{v}(w)$ and $Q_{\ell'\sigma}^{v'}(w')$ contain the mass and momentum dependence.

The mass/momentum terms are given by

$$ Q_{\ell s}^{v}(w) = F_\ell(p)\Delta_v(w) \tag{A.2} $$

$$ Q_{\ell'\sigma}^{v'}(w') = F_{\ell'}(q)F_\sigma(q')\Delta_{v'}(w') \tag{A.3} $$

where F denotes the angular momentum barrier functions defined below.

$F_\ell(p)$, $F_{\ell'}(q)$ and $F_\sigma(q')$ are the Blatt-Weisskopf centrifugal-barrier factors as given by von Hippel and Quigg [71]. The form of the F functions, up to $\ell, \ell', \sigma = 3$ are shown below

$$ F_0(p) = 1 \tag{A.4} $$

$$ F_1(p) = \sqrt{\frac{2z}{z+1}} \tag{A.5} $$

$$ F_2(p) = \sqrt{\frac{13z^2}{(z+1)^2 + 9z}} \tag{A.6} $$

$$ F_3(p) = \sqrt{\frac{277z^3}{z(z-15)^2 + 9(2z-5)^2}} \tag{A.7} $$

where $z = (p/p_r)^2$ and $p_r = 0.1973$ GeV/c corresponding to one fermi.

$\Delta_v(w)$ and $\Delta_{v'}(w')$ are the standard Breit-Wigner forms for the isobars, v and v',

$$\Delta_v(w) = \frac{w_0\Gamma_0}{w_0^2 - w^2 - iw_0\Gamma_v(w)} \tag{A.8}$$

$$\Delta_{v'}(w') = \frac{w_0'\Gamma_0'}{w_0'^2 - w'^2 - iw_0'\Gamma_{v'}'(w')} \tag{A.9}$$

with

$$\Gamma_v(w) = \Gamma_0 \frac{w_0}{w}\frac{q}{q_0}\frac{F_s^2(q)}{F_s^2(q_0)} \qquad \Gamma_{v'}'(w') = \Gamma_0' \frac{w_0'}{w'}\frac{q'}{q_0'}\frac{F_s^2(q')}{F_s^2(q_0')} \tag{A.10}$$

where w_0 and Γ_0 are the mass and width of the primary isobar and w_0' and Γ_0' are the mass and width of the secondary isobar. When the mass w is equal to w_0, q is equal to q_0, and $\Gamma(w_0) = \Gamma_0$.

The E functions, in the reflectivity basis, are written as

$$\begin{aligned} {}^{\epsilon}E_m^{J\ell s\ell'\sigma *}(\Omega, \Omega_h, \Omega_{h'}) &= \sum_{\lambda\nu} {}^{\epsilon}D_{m\lambda}^{JP*}(\Phi,\Theta,0) D_{\lambda\nu}^{s}{}^*(\phi,\theta,0) D_{\nu 0}^{\sigma}{}^*(\phi',\theta',0) \\ &\times \ \tilde{\ell}\tilde{\ell}'\tilde{\sigma} \times \langle \ell 0 s\lambda | J\lambda\rangle \langle \ell' 0 \sigma\nu | s\nu\rangle \end{aligned} \tag{A.11}$$

where

$$\tilde{\ell} = \sqrt{(2\ell+1)}, \quad \tilde{\ell}' = \sqrt{(2\ell'+1)}, \quad \tilde{\sigma} = \sqrt{(2\sigma+1)} \tag{A.12}$$

λ is the helicity of the primary isobar which is summed from $-s$ to s. ν is the helicity of the secondary isobar which is summed from $-\sigma$ to σ. $\langle \ell 0 s\lambda | J\lambda\rangle$ and $\langle \ell' 0\sigma\nu | s\nu)\rangle$ are Clebsch-Gordan coefficients. ${}^{\epsilon}D_{m\lambda}^{JP*}(\Phi,\Theta,0)$ is defined by

$${}^{\epsilon}D_{m\lambda}^{JP*}(\Phi,\Theta,0) = \theta(m)[D_{m\lambda}^{J}{}^*(\Phi,\Theta,0) - \epsilon P(-1)^{J-m} D_{-m\lambda}^{J}(\Phi,\Theta,0)] \tag{A.13}$$

where P is the parity of the wave and $\theta(m)$ is a three valued function such that

$$\theta(m) = \frac{1}{\sqrt{2}}, \;\; m > 0 \tag{A.14}$$

$$\theta(m) = \frac{1}{2}, \;\; m = 0 \tag{A.15}$$

$$\theta(m) = 0, \;\; m < 0 \tag{A.16}$$

The D functions are the known rotation functions

$$D^{\ell}_{m'm}(\alpha, \beta, 0) = e^{-im'\alpha} d^{\ell}_{m'm}(\beta) \tag{A.17}$$

with $d^{\ell}_{m'm}(\beta)$ being a function of sines and cosines [18, 72].

The final state ($\eta\pi^+\pi^-\pi^- p$) contains two π^-'s. The interchange of the π^-'s gives two decay amplitudes for each wave and event. These amplitudes are then combined to give a single symmetrized decay amplitude

$$^{\epsilon}\psi_b(\tau) = \frac{1}{\sqrt{2}}(\,^{\epsilon}A_b(\tau) + \,^{\epsilon}A_b(\bar{\tau})) \tag{A.18}$$

where $\bar{\tau}$ is the event with interchange of the π^-'s.

There is an additional symmetrization for some of the waves. The $f_1(1285)$ decays to both $a_0^+(980)\pi^-$ and $a_0^-(980)\pi^+$. These two decay modes are identical except for an interchange of the π^+ with one of the π^-'s. Therefore, the symmetrized amplitude for the $f_1(1285)\pi^-$ states is given as

$$^{\epsilon}\psi_b(\tau) = \frac{1}{2}(\,^{\epsilon}A_b(\tau) + \,^{\epsilon}A_b(\bar{\tau}) + \,^{\epsilon}A_b(\tau') + \,^{\epsilon}A_b(\bar{\tau}')) \tag{A.19}$$

where τ' is the same event as τ with the π^+ interchanged with one of the π^-'s and $\bar{\tau}'$ is the same as $\bar{\tau}$ with the same interchange. The $f_1(1285)\pi^-$ and $\eta(1295)\pi^-$ waves are the only ones with this additional interchange. These formulas give the symmetrized amplitudes for the primary decay mode.

A.3 Double Isobar Decays

The decay amplitudes for double isobar decays are more complicated than those of the primary decays (Appendix A.2). The decay amplitudes for the primary decay mode are simplified by the fact that one of the decay products in each step has spin 0. This is not always true for a double isobar decay (i.e. $\rho^0(770)a_2^-(1320)$). The isobars and decay angles must be redefined for the double isobar decays. The differences are detailed here along with how this analysis handles the decays. However, once the decay amplitudes are calculated, the partial-wave analysis treats the double isobar waves the same as the primary decay waves.

A.3.1 Isobars and Reference Frames

There are still eight variables which define an event for a double isobar: ω, ω', Φ, Θ, ϕ, θ, ϕ', θ'. The variable names remain the same; however the meanings have changed. ω and ω' refer to the isobars of the primary decay (eg. $\rho^0(770)$ and $a_0^-(980)$). The first two angles, $\Omega = (\Phi, \Theta)$, still refer to the Gottfried-Jackson and Triemann-Yang angles of the primary decay. The second two angles, $\Omega_v = (\phi, \theta)$, are the angles of the decay of one of the isobars (v) (i.e. $\rho^0(770) \to \pi^+\pi^-$) in that isobar's rest frame. The last two angles, $\Omega_{v'} = (\phi', \theta')$, are the angles of the decay of the other isobar (i.e. $a_0^-(980) \to \eta\pi$) in its rest frame. The axes in the isobar rest frames are defined the same way as those of the first helicity frame of the primary decay mode. The $\hat{z}_i$ axis is along the isobar momentum ($\vec{p_i}$) in the X^- rest frame. The $\hat{y}_i$ axis is along $\hat{y}_i \propto \hat{z} \times \hat{p}_i$ where $\hat{z}$ is the z axis in the G-J frame. These variables are then used in the calculation of the decay amplitude. The quantum numbers needed to define the state are the same.

A.3.2 Decay Amplitudes for Double Isobar Decays

For double isobar decays (see figure 4.1(b)), the general form of the decay amplitudes, ${}^{\epsilon}A_b(\tau)$, remains the same as before

$$
{}^{\epsilon}A_b(\tau) = {}^{\epsilon}E_m^{J\ell s\ell'\sigma *}(\Omega, \Omega_v, \Omega_{v'}) Q^v_{\ell s}(w) Q^{v'}_{\ell'\sigma}(w') \tag{A.20}
$$

where ${}^{\epsilon}E_m^{J\ell s\ell'\sigma *}(\Omega, \Omega_v, \Omega_{v'})$ contains the angular dependence and $Q^v_{\ell s}(w)$ and $Q^{v'}_{\ell'\sigma}(w')$ contain the mass and momentum dependence. The mass/momentum terms are the same as Equations A.2 and A.3.

The E functions have a different form

$$
\begin{aligned}
{}^{\epsilon}E_m^{J\ell s\ell'\sigma *}(\Omega, \Omega_v, \Omega_{v'}) &= \sum_{\lambda_1\lambda_2} {}^{\epsilon}D^{JP}_{m\lambda_1-\lambda_2}{}^{*}(\Phi,\Theta,0) D^{s}_{\lambda_1 0}{}^{*}(\phi,\theta,0) D^{\sigma}_{\lambda_2 0}{}^{*}(\phi',\theta',0) \\
&\times\ \tilde{\ell}\tilde{\ell}'\tilde{\sigma} \times \langle \ell 0 s\lambda_1 | J\lambda_1\rangle \langle \ell' 0 \sigma\lambda_2 | s\lambda_2\rangle
\end{aligned} \tag{A.21}
$$

where

$$
\tilde{\ell} = \sqrt{(2\ell+1)}, \quad \tilde{\ell}' = \sqrt{(2\ell'+1)}, \quad \tilde{\sigma} = \sqrt{(2\sigma+1)} \tag{A.22}
$$

λ_1 is the helicity of one of the isobars (v) which is summed from $-s$ to s. λ_2 is the helicity of the other isobar (v') which is summed from $-\sigma$ to σ. $\langle \ell 0 s\lambda_1 | J\lambda_1\rangle$ and $\langle \ell' 0 \sigma\lambda_2 | s\lambda_2\rangle$ are Clebsch-Gordan coefficients. ${}^{\epsilon}D^{JP}_{m\lambda_1-\lambda_2}{}^{*}(\Phi,\Theta,0)$ is defined by

$$
{}^{\epsilon}D^{JP}_{m\lambda_1-\lambda_2}{}^{*}(\Phi,\Theta,0) = \theta(m)[D^{J}_{m\lambda_1-\lambda_2}{}^{*}(\Phi,\Theta,0) - \epsilon P(-1)^{J-m} D^{J}_{-m\lambda_1-\lambda_2}(\Phi,\Theta,0)] \tag{A.23}
$$

where P is the parity of the wave and $\theta(m)$ is the three valued function given in Equations A.14-A.16. The D functions are the same rotation functions given in Equation A.17.

A.3.3 Implementation

The current BNL PWA software was not set up to calculate decay amplitudes for decays of states to two isobars. A new version which can do this has been under development for some time. However, it is not currently available. This has caused the double isobar decays to be handled differently in this analysis. The $f_1(1285)$ cut effectively removes the $\rho^0(770)a_2^-(1320)$ events from the sample. This leaves only the $\rho^0(770)a_0^-(980)$ and $\sigma a_0^-(980)$ states of this type.

The $\rho^0(770)a_0^-(980)$ decay amplitudes were calculated as though they were a $\rho^0(770)\pi^-$ state. The $\sigma a_0^-(980)$ decay amplitudes were calculated as though they were a $\sigma\pi^-$ state. These amplitudes were multiplied by a term to give the $a_0^-(980)$ mass dependence. This approach is valid because the $a_0^-(980) \to \eta\pi$ decay has no angular dependence. Also, λ_2=0. The new decay amplitude is given by

$$^{\epsilon}A_b(\tau) = {}^{\epsilon}E_m^{J\ell s*}(\Omega, \Omega_v) Q_{\ell s}^{v}(w) Q_{00}^{v'}(w') \tag{A.24}$$

where $^{\epsilon}E_m^{J\ell s*}(\Omega, \Omega_v)$ contains the angular dependence, $Q_{\ell s}^{v}(w)$ contains the mass and momentum dependence of the $\rho^0(770) \to \pi^+\pi^-$ decay and $Q_{00}^{v'}(w')$ contains the mass and momentum dependence of the $a_0^-(980) \to \eta\pi$ decay. The mass/momentum terms are the same as Equations A.2 and A.3.

The E functions have a different form

$$^{\epsilon}E_m^{J\ell s*}(\Omega, \Omega_v) = \tilde{\ell} \sum_{\lambda} {}^{\epsilon}D_{m\lambda}^{JP*}(\Phi, \Theta, 0) D_{\lambda 0}^{s}{}^{*}(\phi, \theta, 0) \langle \ell 0 s \lambda | J \lambda \rangle \tag{A.25}$$

where $\tilde{\ell} = \sqrt{(2\ell + 1)}$. λ is the helicity of the $\rho^0(770)$ which is summed from -1 to 1. $\langle \ell 0 s \lambda | J \lambda \rangle$ is a Clebsch-Gordan coefficient. $^{\epsilon}D_{m\lambda}^{JP*}(\Phi, \Theta, 0)$ is defined by

$$^{\epsilon}D_{m\lambda}^{JP*}(\Phi, \Theta, 0) = \theta(m)[D_{m\lambda}^{J}{}^{*}(\Phi, \Theta, 0) - \epsilon P (-1)^{J-m} D_{-m\lambda}^{J}(\Phi, \Theta, 0)] \tag{A.26}$$

where P is the parity of the wave and $\theta(m)$ is the three valued function given in Equations A.14-A.16. The D functions are the same rotation functions given in Equation A.17.

A.4 Parameterization of the Isobars

For two of the isobars used in this experiment there is some uncertainty about the best parameterization. These are the $a_0(980)$ and the σ. Most resonances are parameterized by a Breit-Wigner form

$$\Delta_v(w) = \frac{w_0\Gamma_0}{w_0^2 - w^2 - iw_0\Gamma_v(w)} \tag{A.27}$$

where w_0 is the mass of the resonance, Γ_0 is the width and $\Gamma_v(w)$ is given by Equation A.10. However, the Breit-Wigner form may not be adequate to describe the $\eta\pi$ and $\pi^+\pi^-$ spectra.

The decay of the $a_0(980)$ is complicated by the proximity of the $a_0(980)$ to $K\bar{K}$ threshold. The $a_0(980)$ has a decay mode to $K\bar{K}$. However, the $a_0(980)$, as seen in the $\eta\pi$ decay mode, is wide enough that it extends below $K\bar{K}$ threshold. Therefore, another parameterization is needed to describe the $a_0(980)$ in the $K\bar{K}$ spectra. The coupled channel (CC) approach was developed by Flatté [63] while studying the reactions $K^-p \to \Sigma^+(1385)\eta\pi^-$ and $K^-p \to \Sigma^+(1385)K^0K^-$ at 4.2 GeV/c [73].

The new form of the coupled channel Breit-Wigner is given as

$$\Delta_\delta(w) = \frac{|D_\delta(w_t)|}{D_\delta(w)} \tag{A.28}$$

where w_t is the $K\bar{K}$ mass threshold which gives a normalization Δ_δ=1 at $K\bar{K}$ mass threshold. D_δ is given by

$$D_\delta = w_\delta^2 - w^2 - iw_\delta\Gamma_w \tag{A.29}$$

where w_δ is given below and

$$\Gamma_w = \frac{w_t}{w}(g_1^2 q_{\eta\pi} - g_2^2 q_{KK}) \tag{A.30}$$

where g_1 and g_2 are dimensionless coupling constants, while $q_{\eta\pi}$ and q_{KK} are the breakup momenta for the $\eta\pi$ and $K\bar{K}$ channels at isobar mass w.

The term w_δ is given by

$$w_\delta^2 = w_0^2 - r\frac{q_{0KK}}{q_{0\eta\pi}} w_0 \Gamma_0 \tag{A.31}$$

with $q_{0\eta\pi}$ and q_{0KK} being the breakup momenta for the $\eta\pi$ and $K\bar{K}$ channels at the resonant mass w_0.

A new variable, $r = \frac{g_2^2}{g_1^2}$, is defined and g_1 is written as

$$g_1^2 = \frac{w_0^2 \Gamma_0}{w_t w_\delta q_{0\eta\pi}} \tag{A.32}$$

Now, Γ_w can be written as

$$\Gamma_w = \frac{w_0^2 \Gamma_0}{w w_\delta q_{0\eta\pi}}(q_{\eta\pi} + r q_{KK}) \tag{A.33}$$

The parameters used in this analysis are the same as those used in BNL 818 [19, 57], $w_0 = .978$ GeV/c^2, $\Gamma_0 = .068$ GeV/c^{2}and $r = .5$.

While the results of the partial-wave analysis were insensitive to the $a_0(980)$ parameterization, the coupled channel approach was used for the majority of (and final) fits.

The σ state refers to a $\pi\pi$ S-wave state. This state is also fairly complicated. It has been studied by several experiments. The Particle Data Group [18] acknowledges several spin 0 states which decay to $\pi\pi$, including $f_0(980)$, $f_0(1370)$, and $f_0(1500)$.

The last two states are very wide (Γ = 300-500 MeV/c^2 and Γ = 120 MeV/c^2, respectively). This causes interference between the states such that the $f_0(980)$ is sometimes seen as a hole in the $\pi\pi$ spectrum.

The overlap of these resonances means that the normal Breit-Wigner form can not be used to describe the $\pi\pi$ S-wave. One of the ways the $\pi\pi$ S-wave can be describe is given by Au, Morgan and Pennington (AMP) [64]. This was a coupled channel analysis of the $\pi\pi$ and KK S-waves. The K-matrix formalism was used to guarantee unitarity. In this analysis, it is implemented with a single pole at .9828 GeV/c^2 with contributions from both the $\pi\pi$ and KK channels. It should be noted that K-matrix poles can be significantly different than T-matrix poles. The T-matrix poles correspond to the state's mass and width.

Another way to describe the $\pi\pi$ S-wave has been developed by the Crystal Barrel collaboration (CB) [65]. This approach uses several K-matrix poles and 2 channels ($\pi\pi$ and KK). This analysis used 2 poles located at .855 and 1.268 GeV/c^2. The P-vector approach was used for both AMP and CB. The PWA results were not highly sensitive to the parameterization of the $\pi\pi$ S-wave. The AMP parameterization was used in the final fit because its implementation and interpretation are simpler.

A.5 Two-Pole K-Matrix Formalism

The overlap of two Breit-Wigner equations can violate unitarity. In the case where there is significant overlap of two possible states it is necessary to use K-matrix formalism [74]. This will guarantee unitarity. The sum of two overlapping resonances at masses w_a and w_b can be written in the P-vector approach as

$$A = \frac{P_a + P_b}{1 - iK} \tag{A.34}$$

where

$$P_a = \beta_a \frac{w_a \Gamma_a^0}{w_a^2 - w^2} \left(\frac{F_s(q)}{F_s(q_a)} \right) \qquad P_b = \beta_b \frac{w_b \Gamma_b^0}{w_b^2 - w^2} \left(\frac{F_s(q)}{F_s(q_b)} \right) \tag{A.35}$$

Here, β_a and β_b are unitless complex numbers specifying the strengths of the two states. In this analysis, β_a is chosen to be purely real. The K-matrix is given by

$$K = K_a + K_b = \frac{w_a \Gamma_a(w)}{w_a^2 - w^2} + \frac{w_b \Gamma_b(w)}{w_b^2 - w^2} \tag{A.36}$$

with the mass-dependent widths the same as Equation A.10.

The parameters which describe each pole in the K-matrix are β_0, w_0 and Γ_0. However, the w_0 and Γ_0 do not correspond to the mass and width of the state. These are the values of the poles in the K-matrix. They can be converted to the T-matrix through the relationship

$$T = K(I - iK)^{-1} \tag{A.37}$$

The T-matrix poles then correspond to the mass and width of the resonance.

A.6 Allowed Waves

The allowed waves for this PWA and the additional restrictions imposed upon the waves were discussed in Chapter 4. The following tables (Tables A.3, A.4, A.5, A.6, A.7, A.8) list all the waves which were tried in this analysis.

TABLE A.3
$f_1(1285)\pi^-$ WAVES FOR PWA

J	P	C	m	ϵ	Primary Decay Mode	ℓ
1	-	+	0	-	$f_1(1285)\pi^-$	S
1	-	+	1	+/-	$f_1(1285)\pi^-$	S
0	+	+	0	-	$f_1(1285)\pi^-$	P
1	+	+	0	+	$f_1(1285)\pi^-$	P
1	+	+	1	+/-	$f_1(1285)\pi^-$	P
2	+	+	0	-	$f_1(1285)\pi^-$	P
2	+	+	1	+/-	$f_1(1285)\pi^-$	P
1	-	+	0	-	$f_1(1285)\pi^-$	D
1	-	+	1	+/-	$f_1(1285)\pi^-$	D
2	-	+	0	+	$f_1(1285)\pi^-$	D
2	-	+	1	+/-	$f_1(1285)\pi^-$	D
3	-	+	0	-	$f_1(1285)\pi^-$	D
3	-	+	1	+/-	$f_1(1285)\pi^-$	D
2	+	+	0	-	$f_1(1285)\pi^-$	F
2	+	+	1	+/-	$f_1(1285)\pi^-$	F
3	+	+	0	+	$f_1(1285)\pi^-$	F
3	+	+	1	+/-	$f_1(1285)\pi^-$	F
3	-	+	0	-	$f_1(1285)\pi^-$	G
3	-	+	1	+/-	$f_1(1285)\pi^-$	G

TABLE A.4
$\eta(1295)\pi^-$ WAVES FOR PWA

J	P	C	m	ϵ	Primary Decay Mode	ℓ
0	+	+	0	-	$\eta(1295)\pi^-$	S
1	-	+	0	-	$\eta(1295)\pi^-$	P
1	-	+	1	+/-	$\eta(1295)\pi^-$	P
2	+	+	0	-	$\eta(1295)\pi^-$	D
2	+	+	1	+/-	$\eta(1295)\pi^-$	D
3	-	+	0	-	$\eta(1295)\pi^-$	F
3	-	+	1	+/-	$\eta(1295)\pi^-$	F

TABLE A.5
$a_2^-(1320)\eta$ WAVES FOR PWA

J	P	C	m	ϵ	Primary Decay Mode	ℓ	J	P	C	m	ϵ	Primary Decay Mode	ℓ
2	-	+	0	+	$a_2^-(1320)\eta$	S	3	-	+	1	+/-	$a_2^-(1320)\eta$	D
2	-	+	1	+/-	$a_2^-(1320)\eta$	S	1	+	+	0	-	$a_2^-(1320)\eta$	F
1	+	+	0	+	$a_2^-(1320)\eta$	P	1	+	+	1	+/-	$a_2^-(1320)\eta$	F
1	+	+	1	+/-	$a_2^-(1320)\eta$	P	2	+	+	0	+	$a_2^-(1320)\eta$	F
2	+	+	0	-	$a_2^-(1320)\eta$	P	2	+	+	1	+/-	$a_2^-(1320)\eta$	F
2	+	+	1	+/-	$a_2^-(1320)\eta$	P	3	+	+	0	-	$a_2^-(1320)\eta$	F
3	+	+	0	+	$a_2^-(1320)\eta$	P	3	+	+	1	+/-	$a_2^-(1320)\eta$	F
3	+	+	1	+/-	$a_2^-(1320)\eta$	P	2	-	+	0	-	$a_2^-(1320)\eta$	G
0	-	+	0	+	$a_2^-(1320)\eta$	D	2	-	+	1	+/-	$a_2^-(1320)\eta$	G
1	-	+	0	-	$a_2^-(1320)\eta$	D	3	-	+	0	+	$a_2^-(1320)\eta$	G
1	-	+	1	+/-	$a_2^-(1320)\eta$	D	3	-	+	1	+/-	$a_2^-(1320)\eta$	G
2	-	+	0	+	$a_2^-(1320)\eta$	D	3	+	+	0	+	$a_2^-(1320)\eta$	H
2	-	+	1	+/-	$a_2^-(1320)\eta$	D	3	+	+	1	+/-	$a_2^-(1320)\eta$	H
3	-	+	0	-	$a_2^-(1320)\eta$	D							

TABLE A.6
$a_1^-(1260)\eta$ WAVES FOR PWA

J	P	C	m	ϵ	Primary Decay Mode	ℓ
1	-	+	0	-	$a_1^-(1260)\eta$	S
1	-	+	1	+/-	$a_1^-(1260)\eta$	S
0	+	+	0	-	$a_1^-(1260)\eta$	P
1	+	+	0	+	$a_1^-(1260)\eta$	P
1	+	+	1	+/-	$a_1^-(1260)\eta$	P
2	+	+	0	-	$a_1^-(1260)\eta$	P
2	+	+	1	+/-	$a_1^-(1260)\eta$	P
1	-	+	0	-	$a_1^-(1260)\eta$	D
1	-	+	1	+/-	$a_1^-(1260)\eta$	D
2	-	+	0	+	$a_1^-(1260)\eta$	D
2	-	+	1	+/-	$a_1^-(1260)\eta$	D
3	-	+	0	-	$a_1^-(1260)\eta$	D
3	-	+	1	+/-	$a_1^-(1260)\eta$	D
2	+	+	0	-	$a_1^-(1260)\eta$	F
2	+	+	1	+/-	$a_1^-(1260)\eta$	F
3	+	+	0	+	$a_1^-(1260)\eta$	F
3	+	+	1	+/-	$a_1^-(1260)\eta$	F
3	-	+	0	-	$a_1^-(1260)\eta$	G
3	-	+	1	+/-	$a_1^-(1260)\eta$	G

TABLE A.7

$\rho^0(770)a_0^-(980)$ WAVES FOR PWA

J	P	C	m	ϵ	Primary Decay Mode	ℓ	J	P	C	m	ϵ	Primary Decay Mode	ℓ
1	-	+	0	-	$\rho^0 a_0^-(980)$	S	2	-	+	1	+/-	$\rho^0 a_0^-(980)$	D
1	-	+	1	+/-	$\rho^0 a_0^-(980)$	S	3	-	+	0	-	$\rho^0 a_0^-(980)$	D
0	+	+	0	-	$\rho^0 a_0^-(980)$	P	3	-	+	1	+/-	$\rho^0 a_0^-(980)$	D
1	+	+	0	+	$\rho^0 a_0^-(980)$	P	2	+	+	0	-	$\rho^0 a_0^-(980)$	F
1	+	+	1	+/-	$\rho^0 a_0^-(980)$	P	2	+	+	1	+/-	$\rho^0 a_0^-(980)$	F
2	+	+	0	-	$\rho^0 a_0^-(980)$	P	3	+	+	0	+	$\rho^0 a_0^-(980)$	F
2	+	+	1	+/-	$\rho^0 a_0^-(980)$	P	3	+	+	1	+/-	$\rho^0 a_0^-(980)$	F
1	-	+	0	-	$\rho^0 a_0^-(980)$	D	3	-	+	0	-	$\rho^0 a_0^-(980)$	G
1	-	+	1	+/-	$\rho^0 a_0^-(980)$	D	3	-	+	1	+/-	$\rho^0 a_0^-(980)$	G
2	-	+	0	+	$\rho^0 a_0^-(980)$	D							

TABLE A.8

$\sigma a_0^-(980)$ WAVES FOR PWA

J	P	C	m	ϵ	Primary Decay Mode	ℓ	J	P	C	m	ϵ	Primary Decay Mode	ℓ
0	+	+	0	-	$\sigma a_0^-(980)$	S	2	+	+	1	+/-	$\sigma a_0^-(980)$	D
1	-	+	0	-	$\sigma a_0^-(980)$	P	3	-	+	0	-	$\sigma a_0^-(980)$	F
1	-	+	1	+/-	$\sigma a_0^-(980)$	P	3	-	+	1	+/-	$\sigma a_0^-(980)$	F
2	+	+	0	-	$\sigma a_0^-(980)$	D							

BIBLIOGRAPHY

[1] A. Einstein. *The World As I See It.* Covici Friede Publishers, New York, 1934. pages 137-139.

[2] M. Gell-Mann and Y. Ne'eman. *The Eightfold Way.* W.A. Benjamin, Inc., New York, 1964.

[3] N. Isgur. Concluding remarks: Light quarks and glue (theory). In F. Binon, J.-M. Frère and J.-P. Peigneux, editor, *Proceedings of Hadron '89, Ajaccio, Corsica, France*, pages 709–737, B.P. 33, 91192 Gif-sur-Yvette Cedex-France, 1990. Editions Frontières.

[4] L. Montanet. Concluding remarks: Light quark mesons and exotics (experimental). In F. Binon, J.-M. Frère and J.-P. Peigneux, editor, *Proceedings of Hadron '89, Ajaccio, Corsica, France*, pages 669–683, B.P. 33, 91192 Gif-sur-Yvette Cedex-France, 1990. Editions Frontières.

[5] M. Poulet. Exotic mesons (an experimental review). In *Invited Talk to the First Biennal Conferencoe on Low Antiproton Physics, Stockholm, Sweden, July 2-6, 1990*, September 1990. LAPP-EXP/90-10.

[6] S. Godfrey. An overview of hybrid meson phenomenology. In S.U. Chung, editor, *Proceedings of the BNL Workshop on Glueballs, Hybrids, and Exotic Hadrons (Glue '88)*, pages 373–388, New York, 1989. American Institute of Physics Conference Proceedings No. 185.

[7] E852 Collaboration. P852 proposal. October 2, 1989 (unpublished).

[8] F. de Viron and J. Weyers. New meson configuration in the bag model (I). first order energy spectrum of $q\bar{q}g$ states. *Nuclear Physics*, B185:391–402, 1981.

[9] T. Barnes *et al.* $q\bar{q}g$ hybrid mesons in the MIT bag model. *Nuclear Physics*, B224:241–264, 1983.

[10] M. Chanowitz and S. Sharpe. Hybrids: Mixed states of quarks and gluons. *Nuclear Physics*, B222:211–244, 1983.

[11] N. Isgur and J. Paton. Flux-tube model for hadrons in QCD. *Physical Review D*, 31(11):2910–2929, June 1985.

[12] R. Kokoski and N. Isgur. Meson decays by flux-tube breaking. *Physical Review D*, 35(3):907–933, February 1987.

[13] F. E. Close and P. R. Page. The production and decay of hybrid mesons by flux-tube breaking. *Nuclear Physics*, B443:233–254, 1995.

[14] D. Alde *et al.* Evidence for a 1^{-+} exotic meson. *Physics Letters B*, 205:397, 1988.

[15] Y.P. Gouz *et al.* Study of the wave with $J^{PC} = 1^{-+}$ in the partial wave analysis of $\eta'\pi^-$, $\eta\pi^-$, $f_1(1295)\pi^-$, and $\rho^0\pi^-$ systems produced in $\pi^- N$ interactions at $p_{\pi^-} = 37$ GeV/c. In J.R. Sanford, editor, *Proceedings of the XXVIth Int. Conf. on High Energy Physics, 1992, Dallas, Texas*, pages 572–576, New York, 1993. American Institute of Physics Conference Proceedings.

[16] J. H. Lee *et al.* Spin-parity analysis of the $f_1(1285)\pi^-$ system in the reaction $\pi^- p \rightarrow f_1(1285)\pi^- p$ at 18 GeV/c. *Physics Letters B*, 323:227–233, 1994.

[17] H. Aoyagi *et al.* New results on spectroscopy from BENKEI. *Nuovo Cimento*, 107 A(10):1925–1939, October 1994.

[18] Particle Data Group. Review of particle physics. *Physical Review D*, 54(1), July 1996.

[19] J. H. Lee. *Study of the $f_1(1285)\pi^-$ System Produced in the Reaction $\pi^- p \rightarrow f_1(1285)\pi^- p$ at 18 GeV/c.* PhD thesis, Kyungpook National University, 1993.

[20] K. Danyo Blackett. *The Photoproduction of Possible Hybrid Mesons at $< E_\gamma > = 110$ GeV.* PhD thesis, The University of Tennessee, Knoxville, Knoxville, Tennessee, 1995.

[21] A. Etkin. HEUB PWC system. MPS note 47, 1978 (unpublished).

[22] A. Etkin. Momentum measurement in A1 (HEUB). MPS note 49, 1979 (unpublished).

[23] R.M. Edelstein. Note on beam cerenkov counters for MESB/MPS. MPS note 16, 1973 (unpublished).

[24] E. Halik. Multiparticle spectrometer magnet (MPS). MPS note 17, 1972 (unpublished).

[25] Z. Bar-Yam *et al.* A cylindrical drift chamber with azimuthal and axial position readout. *Nuclear Instruments & Methods*, A386:235–248, 1997.

[26] Z. Bar-Yam *et al.* A cylindrical drift chamber of novel design. *Nuclear Instruments & Methods*, A342:398–410, 1994.

[27] T. Adams *et al.* Design and performance of a cesium iodide detector. *Nuclear Instruments & Methods*, A368:617–627, 1996.

[28] S. Eisman *et al.* The MPS II drift chamber system. *Nuclear Instruments & Methods*, 217:140–148, 1983.

[29] S. Ozaki. Description of the MPS II detector system. MPS note 51, 1979 (unpublished).

[30] B.B. Brabson *et al.* A study of two prototype lead glass electromagnetic calorimeters. *Nuclear Instruments & Methods*, A332:419–443, 1993.

[31] R.R. Crittenden *et al.* A 3000 element lead glass electromagnetic calorimeter. *Nuclear Instruments & Methods*, A387:377–394, March 1997.

[32] J.E. Moyal. Theory of ionization fluctuations. *Philosophical Magazine*, 46(374):263–280, March 1955.

[33] W. R. Leo. *Techniques for Nuclear and Particle Physics Experiments*. Springer-Verlag, New York, 1994. p. 17-68.

[34] L. Landau. On the energy loss of fast particles by ionisation. *Journal of Physics U.S.S.R.*, 8:201–204, 1944.

[35] Y. Teramoto. MPS II drift chamber local pattern recognition. MPS note 71, 1982 (unpublished).

[36] Y. Teramoto. MPS II pattern recognition program I. MPS note 72, 1982 (unpublished).

[37] Y. Teramoto. MPS II pattern recognition program II. MPS note 73, 1983 (unpublished).

[38] O.I. Dahl *et al.* SQUAW kinematic fitting program. Univ. of Calif, Berkeley, Group A programming note P-126, 1968 (unpublished).

[39] D. L. Stienike. *An Analysis of the $\pi^-\eta'$ System Produced in the Reaction $\pi^- p \to \pi^-\eta' p$ at 18 GeV/c.* PhD thesis, University of Notre Dame, Notre Dame, Indiana, 1997. (in progress).

[40] A. Gurtu *et al.* Production and decay properties of the D(1285) meson in $K^- p$ interactions at 4.2 GeV/c. *Nuclear Physics*, B151:181–192, 1979.

[41] S. Fukui *et al.* Study of the $\eta\pi^+\pi^-$ system in the $\pi^- p$ charge exchange reaction at 8.95 GeV/c. *Physics Letters B*, 267:293–298, 1991.

[42] A. Ando *et al.* Evidence of Two Pseudoscalar Resonances of the $\eta\pi^+\pi^-$ System in the $D(1285)$ and E/ι Regions. *Physical Review Letters*, 57(11):1296, September 1986.

[43] A. Birman *et al.* Partial-Wave Analysis of the $K^+\bar{K}^0\pi^-$ System. *Physical Review Letters*, 61(14):1557–1560, October 1988.

[44] J.M. Manak. *A Study of the $\eta\pi^+\pi^-$ System Produced in the Reaction $\pi^- p \to \eta\pi^+\pi^- n$ at 18 GeV/c.* PhD thesis, University of Notre Dame, Notre Dame, Indiana, 1997.

[45] S. Teige *et al.* Properties of the $a_0(980)$ meson. (to be submitted).

[46] S. Blessing. *Study of the $K^+\bar{K}^0\pi^-$ System Produced in the Reaction $\pi^- p \to K^+\bar{K}^0\pi^- n$ at 8 GeV/c.* PhD thesis, Indiana University, Bloomington, Indiana, 1988.

[47] E. King. *Study of the $K^+\bar{K}^0\pi^-$ System Produced in the Reaction $K^- p \to K^+\bar{K}^0\pi^-(\Lambda/\Sigma^0)$ at 8 GeV/c.* PhD thesis, University of Massachusetts at Amherst, Amherst, Massachusetts, 1991.

[48] S.U. Chung. Formulas for partial-wave analysis version II. note BNL-QGS-93-05, BNL, March 1995 (unpublished).

[49] S.U. Chung. Spin formalisms. CERN Yellow Report 71-8, CERN, March 1971.

[50] J.D. Hansen *et al.* Formalism and assumptions involved in partial-wave analysis of three-meson system. *Nuclear Physics*, B81:403, 1974.

[51] M. Jacob and G. C. Wick. On the general theory of collisions of particles with spin. *Annals of Physics*, 7:404–428, 1959.

[52] J. D. Richman. *A Study of the Iota in Radiative J/Psi Decays.* PhD thesis, California Institute of Technology, Pasadena, California, December 1984. Appendix B: An Experimenter's Guide to Helicity Formalism.

[53] D. J. Herndon *et al.* Generalized isobar model formalism. *Physical Review D*, 11(11):3165–3182, June 1975.

[54] S. U. Chung and T. L. Trueman. Positivity conditions on the spin density matrix: A simple parameterization. *Physical Review D*, 11(3):633–646, February 1975.

[55] Application Support Group. GEANT program. Computing and Network Support Division, Geneva, Switzerland, March 1994.

[56] L. Lyons. *Statistics for nuclear and particle physicists.* Cambridge University Press, New York, 1986. p. 85-102.

[57] J. P. Cummings. *A Study of the $K^+\bar{K}^0\pi^-$ System Produced in the Reaction $\pi^- p \rightarrow K^+\bar{K}^0\pi^- n$ at 18 GeV/c.* PhD thesis, Rice University, Houston, Texas, May 1995.

[58] F. James. MINUIT - function minimization and error analysis. CERN Program Library Long Writeup D506, 1994 (unpublished).

[59] F. James. Determining the statistical significance of experimental results. In C. Verkerk, editor, *Proceedings of the 1980 CERN School of Computing*, pages 182–219, Geneva, Switzerland, September 1980.

[60] D. Thompson *et al.* Exotic meson production in the reaction $\pi^- p \to \eta\pi^- p$ at 18 GeV/c. *Physical Review Letters*. (to be submitted).

[61] D. Thompson. PhD thesis, University of Notre Dame, Notre Dame, Indiana, 1997. (in progress).

[62] S.A. Taegar. *A Study of the $\eta\eta$ System Produced in the Reaction $\pi^- p \to \eta\eta n$ at 18 GeV/c.* PhD thesis, University of Notre Dame, Notre Dame, Indiana, 1997.

[63] S.M. Flatté. Coupled-channel analysis of the $\pi\eta$ and $K\bar{K}$ systems near $K\bar{K}$ threshold. *Physics Letters*, 63B:224–227, July 1976.

[64] K.L. Au, D. Morgan and M.R. Pennington. Meson dynamics beyond the quark model: Study of final-state interactions. *Physical Review D*, 35(5):1633–1664, March 1987.

[65] C. Amsler *et al.* High-statistics study of $f_0(1500)$ decay into $\pi^0\pi^0$. *Physics Letters B*, 342:433–439, 1995.

[66] H. Grassler *et al.* Production and decay of the $\delta(980)$ and D(1285) mesons in $\pi^\pm p$ interactions at 16 GeV/c. *Nuclear Physics*, B121:189–209, 1977.

[67] D. Ryabchikov. Private communication.

[68] T. Barnes *et al.* Higher quarkonia. *Physical Review D*, 55:4157–4188, 1997.

[69] A. Ostrovidov. Private communication (to be published).

[70] G. Ascoli *et al.* Partial wave analysis of the Deck amplitude for $\pi N \rightarrow \pi\pi\pi N$. *Physical Review D*, 8(11):3894–3919, 1973.

[71] Frank von Hippel and C. Quigg. Centifugal-barrier effects in resonance partial decay widths, shapes, and production amplitudes. *Physical Review D*, 5(3):624–638, February 1972.

[72] M. E. Rose. *Elementary Theory of Angular Momentum.* John Wiley & Sons, New York, 1957.

[73] J.B. Gay *et al.* Production and decay properties of the $\delta(970)$ meson. *Physics Letters*, 63B:220–223, July 1976.

[74] S. U. Chung *et al.* Partial wave analysis in K-matrix formalism. *Annalen der Physik*, 4:404–430, 1995.